



Strojniški vestnik

Journal of Mechanical Engineering

no. **12**
year **2018**
volume **64**



Strojniški vestnik – Journal of Mechanical Engineering (SV-JME)

Aim and Scope

The international journal publishes original and (mini)review articles covering the concepts of materials science, mechanics, kinematics, thermodynamics, energy and environment, mechatronics and robotics, fluid mechanics, tribology, cybernetics, industrial engineering and structural analysis.

The journal follows new trends and progress proven practice in the mechanical engineering and also in the closely related sciences as are electrical, civil and process engineering, medicine, microbiology, ecology, agriculture, transport systems, aviation, and others, thus creating a unique forum for interdisciplinary or multidisciplinary dialogue.

The international conferences selected papers are welcome for publishing as a special issue of SV-JME with invited co-editor(s).

Editor in Chief

Vincenc Butala

University of Ljubljana, Faculty of Mechanical Engineering, Slovenia

Technical Editor

Pika Škraba

University of Ljubljana, Faculty of Mechanical Engineering, Slovenia

Founding Editor

Bojan Kraut

University of Ljubljana, Faculty of Mechanical Engineering, Slovenia

Editorial Office

University of Ljubljana, Faculty of Mechanical Engineering

SV-JME, Aškerčeva 6, SI-1000 Ljubljana, Slovenia

Phone: 386 (0)1 4771 137

Fax: 386 (0)1 2518 567

info@sv-jme.eu, <http://www.sv-jme.eu>

Print: Abografika, printed in 300 copies

Founders and Publishers

University of Ljubljana, Faculty of Mechanical Engineering,
Slovenia

University of Maribor, Faculty of Mechanical Engineering,
Slovenia

Association of Mechanical Engineers of Slovenia

Chamber of Commerce and Industry of Slovenia,

Metal Processing Industry Association

President of Publishing Council

Mitjan Kalin

University of Ljubljana, Faculty of Mechanical Engineering, Slovenia

Vice-President of Publishing Council

Jože Balič

University of Maribor, Faculty of Mechanical Engineering, Slovenia

International Editorial Board

Kamil Arslan, Karabuk University, Turkey

Hafiz Muhammad Ali, University of Engineering and Technology, Pakistan

Josep M. Bergada, Polytechnical University of Catalonia, Spain

Anton Bergant, Litostroj Power, Slovenia

Miha Boltežar, UL, Faculty of Mechanical Engineering, Slovenia

Franci Čuš, UM, Faculty of Mechanical Engineering, Slovenia

Janez Diaci, UL, Faculty of Mechanical Engineering, Slovenia

Anselmo Eduardo Diniz, State University of Campinas, Brazil

Igor Emri, UL, Faculty of Mechanical Engineering, Slovenia

Imre Felde, Obuda University, Faculty of Informatics, Hungary

Janez Grum, UL, Faculty of Mechanical Engineering, Slovenia

Imre Horvath, Delft University of Technology, The Netherlands

Aleš Hribenik, UM, Faculty of Mechanical Engineering, Slovenia

Soichi Ibaraki, Kyoto University, Department of Micro Eng., Japan

Julius Kaplunov, Brunel University, West London, UK

Iyas Khader, Fraunhofer Institute for Mechanics of Materials, Germany

Jernej Klemenc, UL, Faculty of Mechanical Engineering, Slovenia

Milan Kljajin, J.J. Strossmayer University of Osijek, Croatia

Peter Krajnik, Chalmers University of Technology, Sweden

Janez Kušar, UL, Faculty of Mechanical Engineering, Slovenia

Gorazd Lojen, UM, Faculty of Mechanical Engineering, Slovenia

Thomas Lübken, University of Bremen, Germany

George K. Nikas, KADMOS Engineering, UK

José L. Ocaña, Technical University of Madrid, Spain

Vladimir Popović, University of Belgrade, Faculty of Mech. Eng., Serbia

Franci Pušavec, UL, Faculty of Mechanical Engineering, Slovenia

Bernd Sauer, University of Kaiserslautern, Germany

Rudolph J. Scavuzzo, University of Akron, USA

Branko Vasić, University of Belgrade, Faculty of Mechanical Eng., Serbia

Arkady Voloshin, Lehigh University, Bethlehem, USA

General information

Strojniški vestnik – Journal of Mechanical Engineering is published in 11 issues per year (July and August is a double issue).

Institutional prices include print & online access: institutional subscription price and foreign subscription €100,00 (the price of a single issue is €10,00); general public subscription and student subscription €50,00 (the price of a single issue is €5,00). Prices are exclusive of tax. Delivery is included in the price. The recipient is responsible for paying any import duties or taxes. Legal title passes to the customer on dispatch by our distributor.

Single issues from current and recent volumes are available at the current single-issue price. To order the journal, please complete the form on our website. For submissions, subscriptions and all other information please visit: <http://www.sv-jme.eu>.

You can advertise on the inner and outer side of the back cover of the journal. The authors of the published papers are invited to send photos or pictures with short explanation for cover content.

We would like to thank the reviewers who have taken part in the peer-review process.

The journal is subsidized by Slovenian Research Agency.

Strojniški vestnik - Journal of Mechanical Engineering is available on <http://www.sv-jme.eu>, where you access also to papers' supplements, such as simulations, etc.



Cover:

Active flow control with plasma actuator around an airfoil. Implementation of the plasma actuator geometries to optimize shifting of stall angle, increasing lift and decreasing drag forces. The implementation of this technique proves that aerodynamic performance of an aeroplane can be improved while achieving higher energy efficiency.

Image Courtesy:

Çukurova University, Adana, TURKEY, Scientific Research Projects (BAP, FBA-2017-7111)

ISSN 0039-2480, ISSN 2536-2948 (online)

© 2018 Strojniški vestnik - Journal of Mechanical Engineering. All rights reserved. SV-JME is indexed / abstracted in: SCI-Expanded, Compindex, Inspec, ProQuest-CSA, SCOPUS, TEMA. The list of the remaining bases, in which SV-JME is indexed, is available on the website.

Contents

Strojniški vestnik - Journal of Mechanical Engineering
volume 64, (2018), number 12
Ljubljana, December 2018
ISSN 0039-2480

Published monthly

Papers

Hürrem Akbıyık, Hakan Yavuz, Yahya Erkan Akansu: A Study on the Plasma Actuator Electrode Geometry Configurations for Improvement of the Aerodynamic Performance of an Airfoil	719
Jinguo Chen, Minli Zheng, Yushuang Sun, Wei Zhang, Pengfei Li: Research on the Microscopic Mechanism of the Bond Breakage of Cemented Carbide Tools	726
Igor Šauperl, Andreas Wimmer, Dimitar Dimitrov, Jan Zelenka, Gerhard Pirker, Eduard Schneßl, Hubert Winter: LDM COMPACT – A Methodology for Development of Gas Engines for Use with Low Environmental Impact Non-Natural Gas	743
Jovan Trajkovski, Miha Ambrož, Robert Kunc: The Importance of Friction Coefficient between Vehicle Tyres and Concrete Safety Barrier to Vehicle Rollover - FE Analysis Study	753
Jasna Prester, Borut Buchmeister, Iztok Palčič: Effects of Advanced Manufacturing Technologies on Manufacturing Company Performance	763
Ma'en S. Sari, Wael G. Al-Kouz, Anas Atieh: Buckling Analysis of Axially Functionally Graded Tapered Nanobeams Resting on Elastic Foundations, Based on Nonlocal Elasticity Theory	772

A Study on the Plasma Actuator Electrode Geometry Configurations for Improvement of the Aerodynamic Performance of an Airfoil

Hürrem Akbıyık¹ – Hakan Yavuz^{1,*} – Yahya Erkan Akansu²

¹ Çukurova University, Faculty of Engineering and Architecture, Turkey

² Niğde Ömer Halisdemir University, Faculty of Engineering, Turkey

In this study, the induced flow effects of plasma generated by various types of electrode geometry configurations are presented. The model chosen for the study is a NACA0015 airfoil. The experiments are conducted in a wind tunnel at Reynolds number of 4.8×10^4 . The plasma actuators mounted on the leading edge of the airfoil at chord position of 0.1 (x/C). The plasma actuators consist of an embedded and exposed electrode between which a dielectric material is placed. The applied voltage is set to 7 kV_{pp}. The excitation frequency is also set to 3.5 kHz. Three different electrode geometry configurations, namely as linear, saw-tooth and square, are considered for the study. As a part of the experimental study, the two dimensional and three dimensional flow structures generated by the plasma actuators and related analysis results are presented. In addition, necessary measurements are also made to determine the drag and lift forces.

Keywords: NACA0015 airfoil, lift and drag coefficients, square plasma actuator, sawtooth plasma actuator, linear plasma actuator

Highlights

- The 2D and 3D flow structure generated by the plasma actuators.
- The plasma actuator geometry is determined according to the necessary conditions of the aircraft.
- The stall angle is shifted by 2 degrees.

0 INTRODUCTION

In recent years, plasma actuators have become an important tool in flow control applications. The plasma actuators basically maintain a surface discharge that starts with delaying flow separation on airplane wings. In flow control application, the performance of the plasma actuators appears to be far more effective than that of the base airfoil model. It is well-known that the generated plasma contributes to the flow around the bodies. In terms of flow control effectiveness, parameters such as thickness of the dielectric material, dielectric constant of the dielectric material, the distance between electrodes, the electrode lengths, applied voltage level, applied voltage signal properties, electrode geometry and the number of electrodes appear to play an important role in the process.

Erfani et al. [1] conducted a study in which the plasma structures formed by placing a plasma actuator having a multiple encapsulated electrode structure with an electrode in contact with air on a flat plate. The induced flow velocity is increased and more momentum is provided by using multiple-encapsulated electrodes. Also, the most effective electrode structure is identified in their study. Hale et al. [2] reported that the multiple encapsulate electrode structure affects the induced jet structure. Their results

revealed that the generated induced jet positions have an influence on the jet length. Also, the jet velocity appears to increase linearly along the embedded electrodes. In their experiments, all multiple-encapsulated electrode geometries provide higher velocity values than the classical models. Akansu et al. [3] placed plasma actuators at different positions ($x/C = 0.1, 0.3, 0.5, 0.9$) in order to control flow around a NACA0015 airfoil. The plasma actuators led to reattach flow over the airfoil and also the lift coefficients were increased. In their numerical study, Zhang et al. [4] reported that the lift effect is increased when the plasma actuators are placed on the Gurney flaps. Wang et al. [5] placed four electrode geometries on a flat plate and produced three dimensional (3D) vortex structures in their numerical study. 3D effects such as compression and expansion were observed by using square and serpentine plasma actuators in the flow over the electrode. Numerical results have shown that the linear actuator is less effective in creating the vortex structure in the flow direction than the other designed models. Roy and Wang [6] used serpentine and horseshoe shaped plasma actuators in order to change boundary layer's thickness. They observed that the serpentine and horseshoe shaped plasma actuators lead to 3D flow structures. Not only these actuators help to reattach the flow on model surfaces but also with momentum transfer they

*Corr. Author's Address: Çukurova University, Faculty of Engineering and Architecture, Adana, Turkey, hyavuz@cu.edu.tr

convert the flow type from two dimensional (2D) flow structure to a 3D volume flow. Akbiyik et al. [7] reported that intermittent plasma actuators give rise to reduction in drag coefficient of a bluff body and lead to changes in wake width of the bluff body. 2D flow structure around the bluff bodies is converted into a 3D flow structure by intermittent plasma actuators [7]. Bhattacharya and Gregory [8] and [9] reported 3D instabilities in the wake of a circular cylinder by using spanwise segmented plasma actuators. For flow control, 3D flow structure produced by segmented plasma actuators is more effective than 2D actuation. Lu et al. [10] reported results of an experimental work based on saw-tooth plasma actuators mounted on the NACA0015 airfoil at $Re = 7.7 \times 10^4$. In their study, they reported that they achieved 5° delay in the attack angle of the airfoil and also 9 % increases in lift force. Compared to standard type linear plasma actuators with saw-tooth plasma actuators at the same input power, the attack angle shift is about 3° and increase in lift force is about 3 %. Belan and Messanelli [11] studied corona and dielectric barrier discharge (DBD) plasma actuators with triangular actuator shapes. They compared these two sets of plasma actuators in terms of far field ionic wind, mass flow and efficiency. Their results showed that the tips of triangular plasma actuators improve the efficiency of these actuators. The plasma actuators with multiple tips have better performances in generation of longitudinal ionic wind. Also, the tips improve the stability of coronas. Berendt et al. [12] compared the saw-tooth floating with the traditional DBD floating electrode structure. They varied the positions of the floating electrodes in order to obtain the maximum airflow velocity. They reported that the velocities of the airflow generated by the DBD saw-tooth floating electrode are higher than that of the traditional DBD floating electrodes. The 3D flow structure is also obtained with sinewave (also called serpentine) shaped plasma actuators as well

as the saw-tooth shaped plasma actuators. Liu et al. [13] compared standard actuator configurations with sinewave and saw-tooth actuator configuration on boundary layer flows. They reported that the sinewave and saw-tooth type actuators are more effective for changing the boundary layer flow than conventional actuator configurations. Liu et al. [14] also reported that the produced 3D flow structure by saw-tooth shaped plasma actuators have certain application area such as flow separation suppression.

The aim of this study is to present the results for flow separation control and increase in lift force for different plasma actuator electrode structures. The experiments are performed on the NACA0015 aircraft wing. The study focuses on the electrode geometries that are most widely used in aerodynamic applications.

1 EXPERIMENTAL SETUP

The experiments were conducted on a wind tunnel with a test section of $570 \text{ mm} \times 570 \text{ mm} \times 1000 \text{ mm}$. In Fig. 1 the test model and experimental setup of plasma actuator are illustrated. The NACA0015 airfoil is used as a test model in the experiments at $Re_C = 48000$. The chord length and spanwise length of the airfoil are 150 mm and 540 mm, respectively.

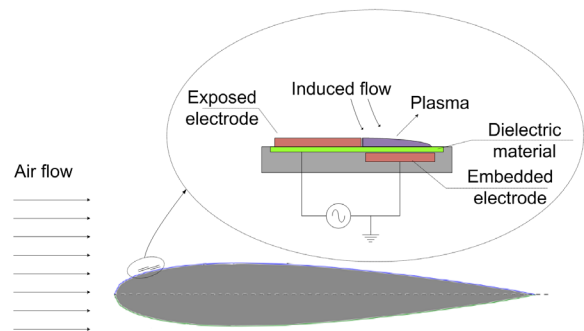


Fig. 1. The test model and experimental setup of plasma actuator

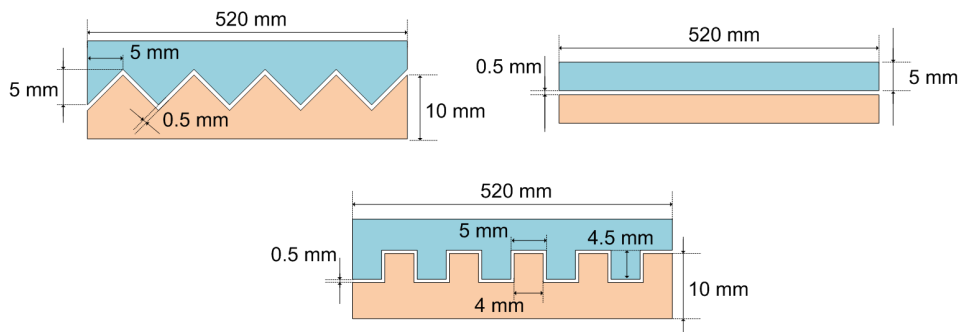


Fig. 2. The electrode geometry configurations, saw-tooth, linear and square

As it is seen in Fig. 2 three different electrode geometry configurations namely as linear, saw-tooth and square types are illustrated. The plasma actuators were mounted horizontally on the NACA0015 airfoil at $x/C = 0.1$ where " x/C " denotes dimensionless distance. Each plasma actuator consists of embedded and exposed electrodes. The dielectric material, Kapton, is a dielectric tape with thicknesses of 0.07 mm and it is placed between plasma electrodes.

The force measurement system devices and plasma production system devices are illustrated in Fig. 3. A custom-made power amplifier is used to produce the voltage required for plasma generation. The applied plasma voltage and the frequency are set to 7 kV_{pp} and 3.5 kHz, respectively.

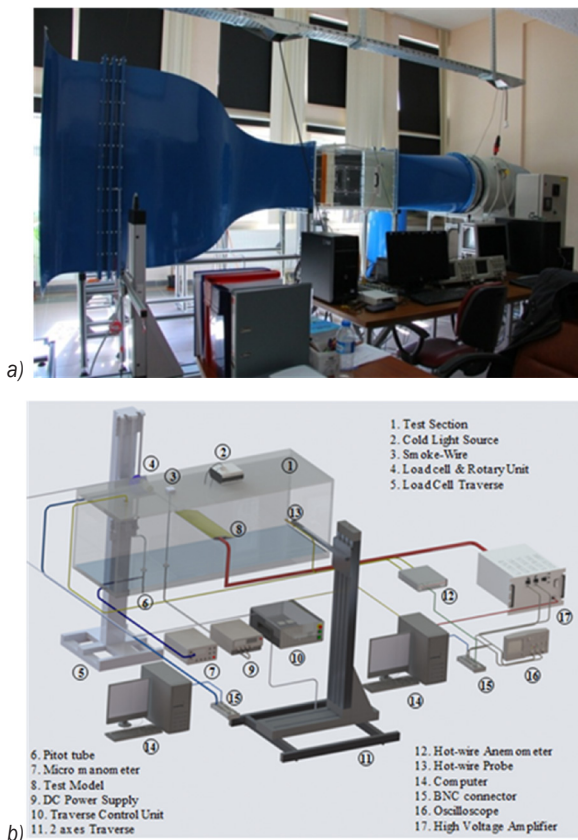


Fig. 3. a) General and b) schematic view of the test setup

The sinusoidal signal waveform is measured by using Tektronix TDS2012B model oscilloscope. The applied voltage is monitored by Tektronix P6015A model voltage probe connected to the oscilloscope.

An ATI Gamma model six axes load cell is used to measure the drag and the lift forces. Test model mounted on a rotary unit to adjust the attack angle of the model. Measurements were taken at 1000 Hz sampling frequency during 10 second period.

Therefore, 10000 sampled values were taken for each measurement and it was repeated twice for each experimental testing session. In order to calculate the net drag forces acting on the airfoil, drag of endplates, holder rod, connector between model and holder rod were exiled from total drag forces.

2 RESULTS AND DISCUSSION

The effects of the plasma actuators shapes placed along the span length of the NACA0015 airfoil are investigated. Three different electrode geometry configurations, linear, saw-tooth and square, are used for the experiments. The plasma actuators were activated at 3.5 kHz excitation frequency and 7 kV_{pp} applied voltage. As it is seen from Fig. 4, the stall angle is shifted from 8° to 10° by using linear and saw-tooth plasma actuators compared with the no plasma condition on the airfoil at $Re = 4.8 \times 10^4$. The square shaped plasma actuator is not effective for delaying stall angle for the same experimental parameters. On the one hand, for the attack angle of 8°, the lift coefficient value is observed to be increasing from 0.70 to 0.80 (approximately 15 % increase) when a saw-tooth shaped plasma actuators is used. The use of a linear plasma actuator appears to increase the lift coefficient approximately by 8 % at the same attack angle. On the other hand, the use of square shaped plasma actuator leads to reduction in lift coefficient of the airfoil. For the attack angle of 10°, the lift coefficient is increased from the value of 0.49 to 0.94 (approximately 91 %) by saw-tooth shaped plasma actuators. The performance enhancement achieved in lift coefficient using the saw-tooth shaped plasma actuator appears to be the same as that of the linear plasma actuators.

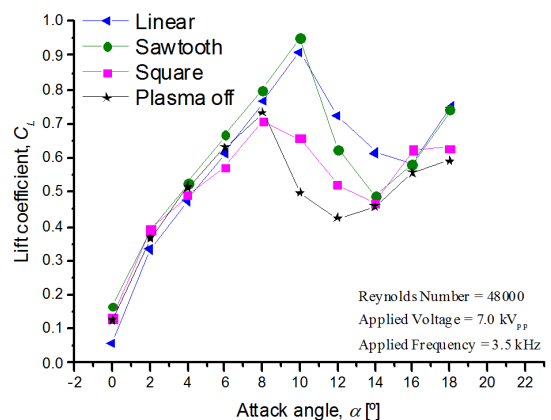


Fig. 4. Effect of the electrode geometry on lift coefficient of the NACA0015 airfoil

As seen from Fig. 5 the use of square shaped and linear plasma actuators leads to reduction in drag. However, there does not appear to be a significant effect in reduction of the drag coefficient for the sawtooth shaped plasma actuators.

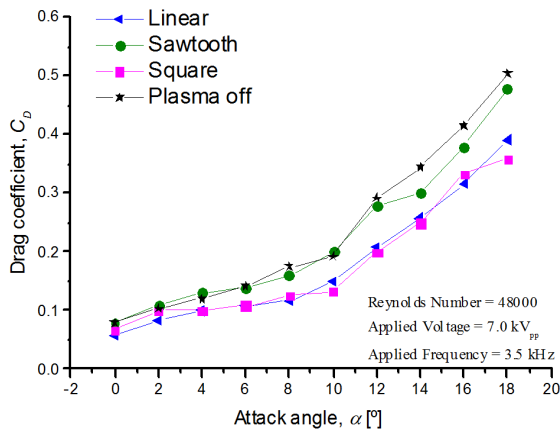


Fig. 5. Effect of the electrode geometry on drag coefficient of the NACA0015 airfoil

The maximum reduction in drag of (about 31 %) is observed at the attack angle of 10° for the square shaped plasma actuators. For the same plasma actuator, the drag coefficient is decreased about 34 % at the attack angle of 12°.

In Figs. 6, 7 and 8, flow visualization of the NACA0015 aircraft wing is performed by the smoke-wire method. For the attack angle of the airfoil at 0, 5, 10 and 15 degrees, flow structure around the airfoil and wake region of the airfoil are observed with the help of the flow visualization method. In Fig. 6, the flow visualization results are presented where the cases of the plasma-off and plasma-on are seen clearly. The induced flow is generated by activating the plasma actuator. This induced flow adds momentum to the separated flow. The separated flow is reattached to the surface of the airfoil with the help of the induced flow.

The plasma actuator appears to be completely controlling the flow around the airfoil at the attack angle of 5°. In addition, the separated flow seems to be reattached to the surface of the airfoil. It is observed that the separated flow is reattached to the surface of the airfoil by the activated plasma actuator at attack angle of 10°. However, with increasing attack angle of the airfoil, the effectiveness of the plasma actuator is decreased. At the attack of 15°, the separated flow is not efficiently reattached to the flow to the airfoil surface. This is mainly due to the fact that the plasma actuator placed in the $x/C = 0.1$ position is not close enough to the separated flow to reattach it to

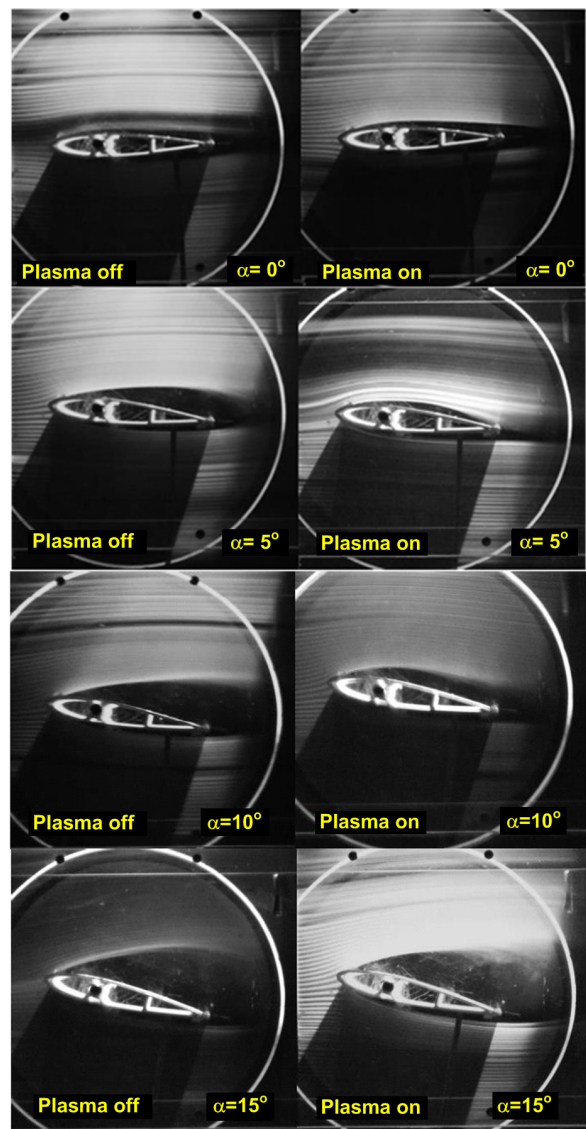


Fig. 6. Visualized flow around the NACA0015 airfoil for $V = 7$ kV_{pp} and $f = 3.5$ kHz at $Re = 25000$ (linear electrodes)

the surface. Hence, for the saw-tooth and the square plasma actuator models, it was unnecessary to obtain flow visualization by the smoke-wire method at the attack angle of 15°. Fig. 7 shows the flow visualization results for square shaped plasma actuator where cases of plasma-on and plasma-off are presented. The flow visualization is performed at $Re = 2.5 \times 10^4$ when the applied plasma voltage and the excitation frequency are set to 7 kV and 3.5 kHz, respectively.

The separated flow is reattached to the surface of the airfoil at the attack angle of 5°. The reattachment of the separated flow is achieved due to the induced flow and the 3D flow structure effects. The square

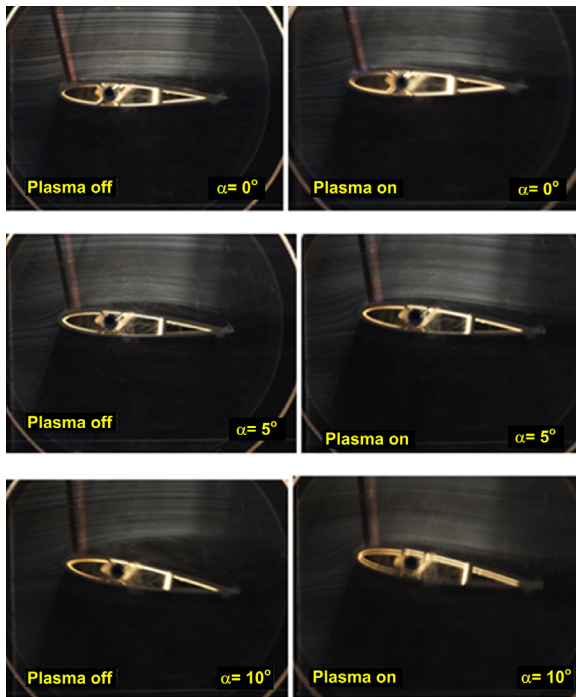


Fig. 7. Visualized flow around the NACA0015 airfoil for $V = 7 \text{ kV}_{pp}$ and $f = 3.5 \text{ kHz}$ at $Re = 25000$ (square electrodes)

shaped plasma actuator is less effective in reattaching the flow to the surface of the airfoil than that of the linear plasma actuator. In square-shaped plasma actuators, the air passing sliding over the surface of the electrodes is held on the electrode surfaces due to induced flow effect of the plasma. However, the air that passes through the gap between the electrodes flows freely. The air that passes through the gap between the electrodes interact with the air flow sliding over the electrode surface that leads to 3D flow structure. At the attack angle of 10° , it is observed that the airfoil reaches to its stall angle. Due to the plasma actuators casing the separated flow become closer to the surface of the airfoil, thus, the stall angle is shifted further.

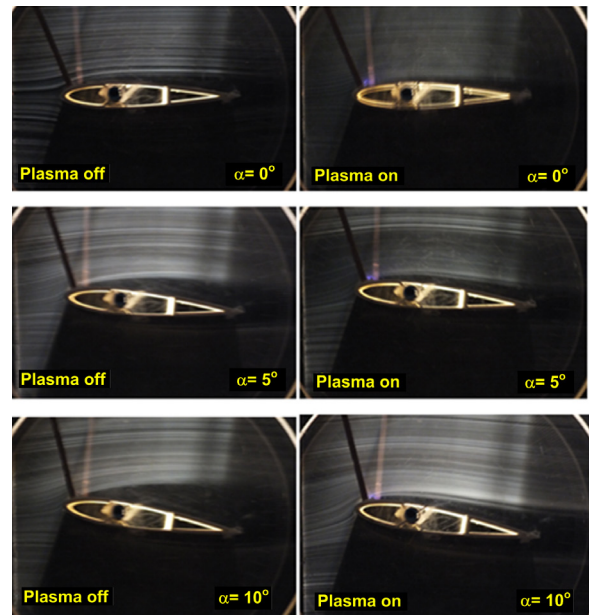
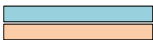




Fig. 8. Visualized flow around the NACA0015 airfoil for $V = 7 \text{ kV}_{pp}$ and $f = 3.5 \text{ kHz}$ at $Re = 25000$ (saw-tooth electrodes)

Fig. 8 illustrates the flow visualization results for the cases of the plasma-off and plasma-on for the saw-tooth shaped plasma actuator. It has been observed that the square and saw-tooth shaped plasma actuator models appear to show similar results in the way they affect the flow. They both force the flow to reattach onto the model surface. The plasma generated by these models also appears to form a 3D flow structure around the airfoil. Comparing the flow visualization results of these two plasma actuators, it is observed that the saw-tooth shaped plasma actuators are far more effective on reattachment of the separated flow onto the model surface. For attack angle of 5° and 10° , this result can be clearly seen from the flow visualization results of the comparison of the relevant plasma actuators.

In Table 1, all the experimental results shown in Figs. 4 and 5 are summarized where the results for comparison of plasma actuators are presented. As seen

Table 1. Plasma actuators and their effect on flow properties

Actuators	Plasma off	Linear	Square	Saw-tooth
Aerodynamic properties	-			
Stall angle	8°	10°	8°	10°
C_L	0.5	0.9	0.65	0.95
C_D	0.22	0.15	0.12	0.20

from Table 1, linear and saw-tooth plasma actuators appears to shift the stall angle about 2° and also increases in lift relative to the other two cases. The linear and square plasma actuators appear to decrease in drag relative to the other two cases. The studied plasma actuators seem to force the separated boundary layer come closer to the airfoil surface due to the effect of induced flow generated and this seems to increase the lift coefficient considerably. The results indicate that, the plasma actuators of square, linear and saw-tooth models increase the lift coefficient by 30 %, 80 % and 90 % relative to plasma-off case, respectively.

The saw-tooth plasma actuators appear to be more suitable for obtaining more lift force on take-off and reducing fuel consumption. However, it seems to be more convenient to use a square-shaped plasma actuator to reduce the drag force acting on the airfoil when there is no need for extra lifting force. This experimental study contributed to the determination of the plasma actuator geometry to be used according to the necessary conditions of the aircraft. In addition, the use of other models in comparison to conventional (linear) plasma actuators appears to reduce fuel consumption due to enhancement in aerodynamic efficiency.

3 CONCLUSIONS

In this study, the effects of the plasma actuator shapes placed along the span length of the NACA0015 airfoil are investigated at $Re = 4.8 \times 10^4$. Three different electrode geometry configurations as linear, saw-tooth and square are used for the experiments. The plasma actuators are activated at 3.5 kHz excitation frequency and 7 kV_{pp} applied voltage. The lift and drag coefficient of the airfoil are examined by varying the attack angle. The following list of conclusions achieved:

- For the attack angle of 10° , the lift coefficient is increased approximately 91 % by saw-tooth shaped plasma actuators. Also, the linear plasma actuator enhanced the lift coefficient significantly.
- The stall angle is shifted from 8° to 10° by using linear and saw-tooth plasma actuators.
- The linear and square shaped plasma actuators also lead to more reduction in the drag than no plasma and saw-tooth shaped plasma actuators cases.
- The maximum reduction in drag is 31 % at the attack angle of 10° for the square shaped plasma actuators. For the same plasma actuator, the drag

coefficient is decreased 34 % at the attack angle of 12° .

4 ACKNOWLEDGEMENTS

The authors would like to acknowledge the financial support of this work by the Scientific Research Projects (BAP) of the Çukurova University under the Contact Number of FBA-2017-7111.

5 NOMENCLATURES

C_D	drag coefficient, [-]
C_L	lift coefficient, [-]
C	chord length, [mm]
x	actuator position, [mm]
Re, Re_C	Reynolds number, [-]
α	attack angle, [$^\circ$]
x/C	dimensionless distance, [-]
kV_{pp}	peak to peak applied voltage, [kV]

6 REFERENCES

- [1] Erfani, R., Erfani, T., Utyuznikov, S.V., Kontis, K. (2013). Optimisation of multiple encapsulated electrode plasma actuator. *Aerospace Science and Technology*, vol. 26, no. 1, p. 120-127, DOI:10.1016/j.ast.2012.02.020.
- [2] Hale, C., Erfani, R., Kontis, K. (2010). Plasma actuators with multiple encapsulated electrodes to influence the induced velocity. *48th AIAA Aerospace Sciences Meeting Including the New Horizons Forum and Aerospace Exposition*, DOI:10.2514/6.2010-1223.
- [3] Akansu, Y.E., Karakaya, F., Şanlısoy, A. (2013). Active control of flow around NACA0015 airfoil by using DBD plasma actuator. *EPJ Web of Conferences*, vol. 45, no. 01008, DOI:10.1051/epjconf/20134501008.
- [4] Zhang, P.F., Liu, A.B., Wang, J.J. (2009). Aerodynamic modification of a NACA 0012 airfoil by trailing-edge plasma Gurney flap. *AIAA Journal*, vol. 47, no. 10, p. 2467-2474 DOI:10.2514/1.43379.
- [5] Wang, C.C., Durscher, R., Roy, S. (2011). Three-dimensional effects of curved plasma actuators in quiescent air. *Journal of Applied Physics*, vol. 109, no. 8, p. 083305, DOI:10.1063/1.3580332.
- [6] Roy, S., Wang, C.C. (2009). Bulk flow modification with horseshoe and serpentine plasma actuators. *Journal of Physics D: Applied Physics*, vol. 42, no. 3, p. 032004, DOI:10.1088/0022-3727/42/3/032004.
- [7] Akbiyik, H., Akansu Y.E., Yavuz, H. (2017). Active control of flow around a circular cylinder by using intermittent DBD plasma actuators. *Flow Measurement and Instrumentation*, vol. 53, part B, p. 215-220, DOI:10.1016/j.flowmeasinst.2016.12.008.
- [8] Bhattacharya, S., Gregory, J.W. (2015). Effect of three-dimensional plasma actuation on the wake of a circular cylinder. *AIAA Journal*, vol. 43, no. 4, p. 958-967, DOI:10.2514/1.J053316.

- [9] Bhattacharya, S., Gregory, J. (2013). The optimum wavelength of spanwise segmented plasma actuator forcing of a circular cylinder wake. *51st AIAA Aerospace Sciences Meeting including the New Horizons Forum and Aerospace Exposition*, no. AIAA 2013-1011, DOI:10.2514/6.2013-1011.
- [10] Lu, Z., Wong, C.W., Wang, L., Alam, M.M., Zhou, Y. (2016). Separation control on a NACA0015 airfoil with plasma-actuator-generated disturbance. *8th AIAA Flow Control Conference*, DOI:10.2514/6.2016-3625.
- [11] Belan, M., Messanelli, F. (2015). Compared ionic wind measurements on multi-tip corona and DBD plasma actuators. *Journal of Electrostatics*, vol. 76, p. 278-287, DOI:10.1016/j.elstat.2015.06.008.
- [12] Berendt, A., Podliński, J., Mizeraczyk, J. (2011). Comparison of airflow patterns produced by DBD actuators with smooth or saw-like discharge electrode. *Journal of Physics: Conference Series*, vol. 301, no. 1, p. 012018, DOI:10.1088/1742-6596/301/1/012018.
- [13] Liu, Z.F., Wang, L.Z., Fu, S. (2011). Study of flow induced by sine wave and saw tooth plasma actuators. *Science China Physics, Mechanics and Astronomy*, vol. 54, no. 11, p. 2033-2039, DOI:10.1007/s11433-011-4511-x.
- [14] Liu, Z.F., Zhang, M.M., Wang, L.Z. (2016). Investigation on 3D flow field induced by a plasma actuator with serrated electrode. *Science Bulletin*, vol. 61, no. 6, p. 481-487, DOI:10.1007/s11434-016-1030-1.

Research on the Microscopic Mechanism of the Bond Breakage of Cemented Carbide Tools

Jinguo Chen^{1,2} – Minli Zheng^{1,*} – Yushuang Sun¹ – Wei Zhang¹ – Pengfei Li¹

¹ Harbin University of Science and Technology, College of Mechanical and Power Engineering, China

² Putian University, School of Electrical and Mechanical Engineering, China

The bond breakage on the rake face of cemented carbide tools has a significant impact on the life of the tool. Using the finite element method, a three-dimensional microstructure model is established for the bond breakage of cemented carbide tools and, based on the analysis of the force conditions in the bond zone, the crack propagation path is investigated at the microscopic scale by varying the cohesive strength of the cemented carbide and the angle between the crack and the rake face to determine the bond breakage process of the cemented carbide tool rake face. The results show that in the absence of the initial cracks, the cracks tend to propagate along the vertical load direction and are deflected due to the increase in the local bonding strength. The angle and location of the cracks and the rake face have a significant influence on the crack propagation path. The stronger the combined force of the cemented carbide, the greater the tensile strength of the material is when there are no cracks in the cemented carbide. In contrast, when initial cracks are present, the crack propagation and crack pinning increase the tensile strength of the material to some extent; however, the increase in the intergranular cracks reduces the overall tensile strength of the material. It is observed from the experiment that intergranular fractures are mainly responsible for the bond breakage of the cemented carbide tools and this result is consistent with the simulation results.

Keywords: bond breakage, crack propagation, cemented carbide tool, tensile strength, cohesive zone model, finite element analyses

Highlights

- A three-dimensional microstructural model of crack propagation in cemented carbide was established.
- The crack propagation path was investigated at the microscopic scale, which illustrated the process of bond breakage.
- The mechanical conditions of the cemented carbide tool in the bond area, the cohesiveness of the cemented carbide, and the crack angle on the rake face were investigated.
- The simulation results illustrated the process of bond breakage.

0 INTRODUCTION

Many researchers have investigated the behaviour of tool-chip adhesion because the bond breakage of cemented carbide tools is a common occurrence during the process of cutting shell material. Sun et al. [1] studied the bond breakage behaviour of several cemented carbide tools during the cutting of 2.25Cr-1Mo steel. It was found that the causes of the tool-chip adhesion were the strong affinity between the tool and the workpiece and the inter-diffusion of the tool and chips under the conditions of high temperature and pressure, which resulted in the formation of a secure joint. Cheng et al. [2] investigated tool bond breakage under extreme overload conditions and the theoretical criterion of tool-chip adhesion was established using experiments and simulations, and a criterion for preventing bond breakage was proposed. Tan et al. [3] researched the distribution of the thermal force of a milling tool with a complex 3D groove and laid a theoretical foundation for analysing the influence of different grooves on the bond breakage mechanisms of milling tools.

The bond breakage process of cemented carbide tools is analysed. During the initial adhesion stage, the surface asperities of the tool and the workpiece in the contact area cause friction. Co in the tool matrix and Fe in the workpiece belong to the same group of elements, and they have a strong affinity for mutual diffusion. The hardness of the chips is lower than that of the tools, and the asperities of the chips and tool result in bonding in the contact area under high temperature and high pressure, as shown in Fig. 1.

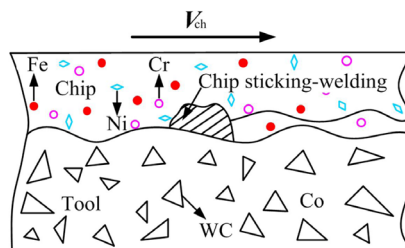


Fig. 1. The initial state of tool-chip adhesion

During the early stages of the cutting process, the type of contact between the tool and chips generally consist of a point contact because of the small contact area; the combined force is relatively small, which

means that the bonding zone is not stable due to the external force. This results in the exposure of areas with larger hardness on the rake face; therefore, a stable bonding zone cannot be formed at this time. Subsequently, more asperities begin to bond in the adhesion area, and this increase causes the tool-chip contact area to extend from the bonding point to the surface, and the combined force also increases accordingly. When the shear resistance of the diffusion joint in the contact area of the two materials exceeds the shear force produced by the chips passing through the rake face of the tool, the newly formed bonding point is not peeled off, as shown in Fig. 2. As the accumulation continues, a stable tool-chip adhesion phenomenon occurs; this is shown in Fig. 3.

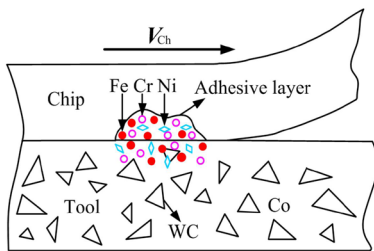


Fig. 2. Stability stage of tool-chip adhesion

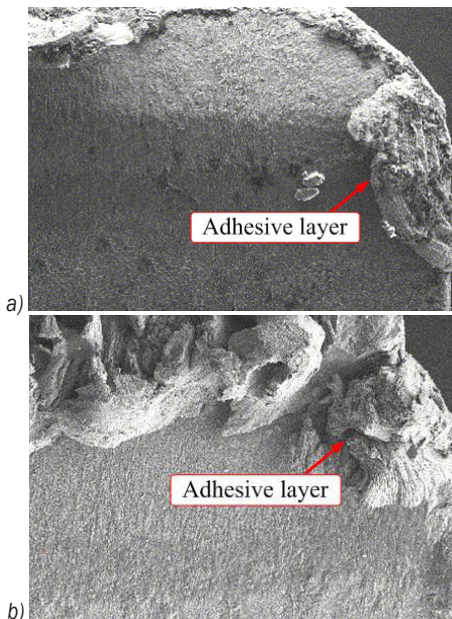


Fig. 3. Microstructural diagram of the tool-chip adhesion on the rake face; a) slight adhesion, and b) severe adhesion

As the cutting continues, due to the continuous element diffusion at the contact area between the tool and chip, extraneous elements such as Fe, Cr, and other elements enter the tool; in addition, the removed chips contain W, Co, and other elements. This changes

the composition and content of the rake face, and the generation of microcracks under high temperature and high pressure will result in the change in the material strength of the rake face. When the combined force of the chip and the bond area is greater than the internal force of the tool, the material of the rake face will be removed in the form of chips and bond breakage occurs, as shown in Fig. 4.

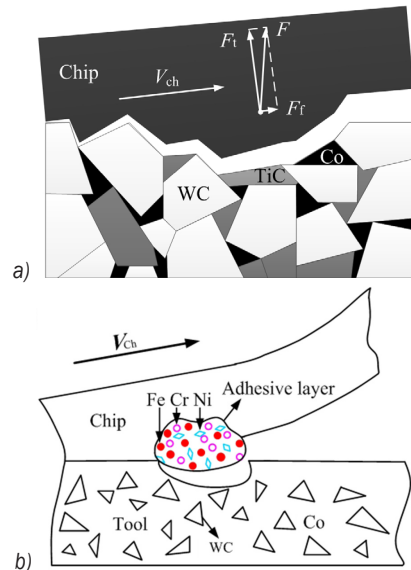


Fig. 4. The adhesion layer is removed in the form of chips; a) forces of the cutting tool in the cutting process, and b) schematic diagram of the formation of tool-chip adhesion

The surface topography of the pits on the cemented carbide tool after bond breakage is observed using a super-depth field emission scanning electron microscope (SEM), as shown in Fig. 5. It is found that the bond breakage has the following characteristics: (1) the area of the bond breakage on the rake face is relatively small. (2) Cracks have formed on the rake face. (3) The surface of the WC particles is intact after the adhesion layer is stripped. These characteristics of the bond breakage and the production of micro defects (such as holes, hot cracks, etc.) on the rake face of the cemented carbide tool occurring during cutting observed at the microscale provide information on the crack propagation path on the rake face of the cemented carbide tool and link the microstructure and macroscopic properties. This information is of great significance to determine the reason for the bond breakage and to improve the service life of the tool.

Many researchers have carried out experimental research on the crack propagation path of cemented carbide tools. Gurland [4] conducted a statistical analysis of the number of WC particles, the WC-WC

boundary, and the WC-Co boundary in the fracture paths of cemented carbide tools; the results showed that the fractures occurred mostly in the WC particles and at the WC-WC boundary. The Mitsubishi Metals Company in Japan observed the crack propagation paths in a cemented carbide tool during a tensile experiment using a SEM; the researchers found that the cracks all occurred at the boundary of the WC-Co and WC-WC and no transgranular fractures occurred. Therefore, the intergranular fracture theory of cemented carbide crack propagation was put forward. The Toshiba Corporation in Japan studied WC-Co fracture morphology, and the fracture behaviour was categorized into three cases: (1) When the grain size of WC was larger than 5 μm , and the Co content was less than 15 %, shearing of the WC grains occurred. (2) When the grain size of WC was less than 2 μm , and the Co content was less than 7 %, the cracks passed through the WC or WC-Co interface. (3) When the size of the WC particles in the cemented carbide was smaller than 4 μm and the Co content was larger than 20 %, the crack passed through the Co phase [5]. Sigl and Exner [6] partitioned the crack propagation paths of WC-Co cemented carbide into four categories, including crack propagation through the Co binder phase, along the WC-Co interface, along the WC-WC interface, and through WC particles. It was also determined that the path along the WC-Co interface did not occur exactly on the WC-Co interface but in the Co binder phase, which was very close to the WC-Co interface and parallel to the interface area; the expansion path along the WC-Co interface had smaller dimples than the path through the Co binder phase.

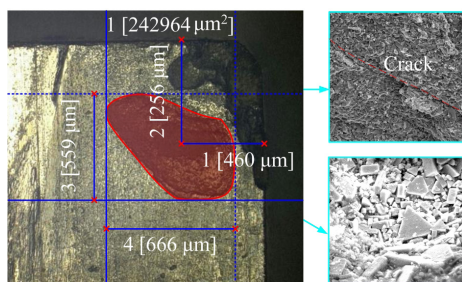


Fig. 5. Bond breakage of the tool

In terms of the research on the cemented carbide simulation: Ljungberg et al. [7] conducted simulations of crack propagation in cemented carbide tools and observed the microstructure using a SEM. The authors established a finite element model and an analysis of the relationship between the maximum plastic zone size of the cemented carbide tip and the mean free path

of the cohesive phase and proved that the carbide grain boundaries did not cause changes in the size of the plastic zone. Fischmeister et al. [8] conducted a study on the plastic deformation of the cohesive phase at the crack tip of the cemented carbide tool and analysed the crack propagation behaviour of the cemented carbide by using the finite element simulation method. The results showed that the void nucleation and growth in the area where the WC phase changed into the Co phase destroyed the reinforcement effect of the plastic zone; the formation and penetration of the void led to crack growth, which resulted in the tear of the perforated plates. Hönle [9] studied the energy consumption and driving force of the crack propagation of cemented carbide using different amounts of Co content and Co inclusions; the results showed that the crack growth occurred at the position of high Co content and Co inclusions with an acute angle. In addition, the influence of the Co inclusion on the energy consumption of the crack propagation was low. Connolly and Mchugh [10] simulated the crack propagation of cemented carbide by using the Gurson model; the results showed that the number of Co layers in the crack propagation path had a large influence on the fracture toughness. Mchugh and Connolly [11] used a numerical simulation to study the ductile failure of the Co binder phase in WC-Co cemented carbide and analysed the crack propagation of cemented carbide under an I-type load. Kim [12] conducted two-dimensional parameterized modelling of cemented carbide; the parameters included the particle size, Co volume fraction, and adjacency. A two-dimensional finite element simulation model of the stress-strain field of the material was developed for predicting the brittle fracture strength of the cemented carbide. Kim et al. [13] used a two-dimensional finite element model to predict the stress-strain distribution and fracture strength of WC-Co composites with a carbide size ranging from 1.4 μm to 5.3 μm and a carbide volume fraction of 0.7 to 0.9. Park [14] used a Boolean algorithm to measure the micro parameters of cemented carbide particles in microscopic images, established a microstructure model of carbide-coated tools by using the obtained structural parameters and analysed the cutting life of the coated cemented carbide tools. Sadowski and Nowicki [15] analysed the elastic-plastic response of cemented carbide and studied the effects of particle size and particle number on the material anisotropy using the finite element method; a microstructure simulation of the cemented carbide based on the microstructure observed in the SEM images was conducted. The results showed that the cemented carbide exhibited less anisotropic

elasticity. Carlsson [16] generated three-dimensional WC grains using the Voronoi method and inserted the Co binder phase between the WC-WC particles to establish a three-dimensional model suitable for modelling the microstructure of the WC-Co cemented carbide; this was used to simulate the yield stress of the material. Park et al. [17] conducted an orthogonal cutting simulation based on the microstructure model of WC-Co cemented carbide to obtain the equivalent stress, strain, and strain energy. A comparison of the predicted and experimental tool failure based on a mixed fracture criterion indicated that the predicted results were in agreement with the experimental results and that the model was suitable for determining the effects of the micro parameters and feed rate on the tool failure. Park et al. [18] established a microstructure prediction model of WC-Co tool failure, validated the results using a turning test, and studied the influence of the microstructure parameters and feed rate on the tool failure using a finite element analysis.

In conclusion, current research on the failure of cemented carbide tools is mainly based on experiments, supplemented by computer simulations. Because of the rigorous experimental conditions, the limitations of the existing experimental equipment, and the high complexity of the research objects, it is difficult to advance the findings. In contrast, the development of computer simulation technology has provided the possibility to explore details at the microscopic level; thus, the breakage caused by the macro-mechanical properties of the tool can be observed at the microscale. This lays the foundation for determining the nature of the bond breakage of the tool. In this study, a three-dimensional microstructure model of the cemented carbide is developed, and the bond breakage of the cemented carbide is simulated in conjunction with the changes in the rake face during the bonding process. The results provide theoretical support for determining the mechanisms of bond breakage.

1 THREE-DIMENSIONAL MICROSTRUCTURAL MODELING OF CRACK PROPAGATION

In this study, we establish a microstructure model of the cemented carbide based on the YT5 tool; the main components of the tool are shown in Table 1. Microstructure observations of the YT5 tool during adhesion are conducted using a SEM, and the measurements of the microstructure parameters are obtained. The theory of stereology is used to establish a microstructure model of the cemented carbide.

Stereology is based on the concept that the area ratio of a component in a two-dimensional image is related to the volume ratio of the component in three-dimensional space.

Table 1. Main components of the carbide tool YT5

components	TiC	WC	Co
content [wt%]	5	85	10

1.1 Determination of Microstructure Parameters

To establish a three-dimensional microstructure model of the cemented carbide, the TiC particles are considered to have the same material properties as WC particles. Therefore, a corresponding simplification is made here, that is, the TiC particles are considered as WC particles to study the model crack propagation. Then Image J software is used to analyse the SEM images of the rake face of the carbide (Fig. 6). The microstructure parameters are calculated to obtain the mean grain size, the volume fraction of each component, and the grain adjacency of the carbide tool rake face.

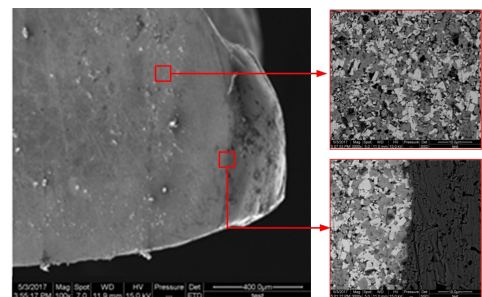


Fig. 6. The tool during adhesion

The analysis steps are as follows:

- (1) Calculation of the volume fraction of each phase
Because the cemented carbide is opaque, one cannot directly observe the composition and the three-dimensional spatial distribution of the phases, and they can only be estimated by observing the two-dimensional microstructure images of the cemented carbide. The two-dimensional microstructure is shown in Fig. 7.

The basic equation of volumetric stereology is shown in Eq. (1):

$$V_V = A_A, \quad (1)$$

where V_V is the volume ratio of the measured tissue in the three-dimensional space and A_A is the area ratio of the measured tissue in the two-dimensional image.

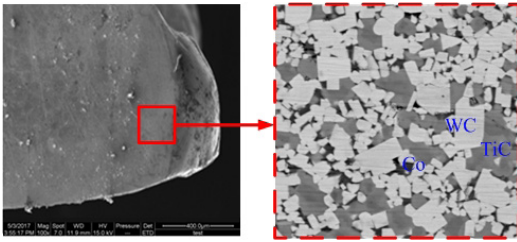


Fig. 7. The two-dimensional microstructure image of the YT5 tool

According to the stereology theory, the volume fraction of each phase in the cemented carbide can be determined by the area of the phase in the cross-section, the percentage of the cross-sections, or the number of observation points. To obtain a relatively accurate area ratio of each phase in the two-dimensional image, the volume fraction of each phase in the cemented carbide was measured using the Image J software and the area method. The image of the microstructure of the YT5 tool is binarized and denoised. In the binary image, the grayscale values range from 0 to 255, where 0 represents black, and 255 represents white. The measurements of the Co and WC phase volume fraction using the grayscale image is shown in Fig. 8. The measurements do not include the volume fraction of the impurities and pores in the cemented carbide, and it is assumed that the cemented carbide contains only WC, TiC, and Co phases. The volume fraction of the WC, Co and TiC phases in the cemented carbide tool can be obtained from the measured average grayscale values.

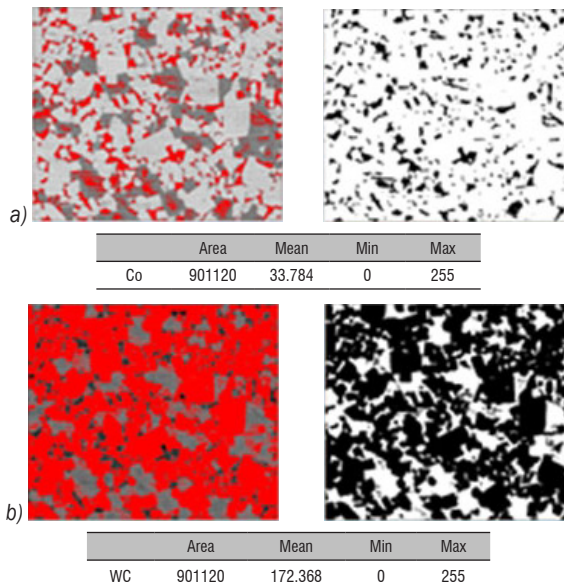


Fig. 8. Co and WC phase volume fractions measurements of the YT5 tool; a) Co, and b) WC

(2) Calculation of the average grain size of WC and TiC

The microstructure image of the YT5 tool is also used to measure the average grain size, as shown in Fig. 9. Because the difference between the WC and TiC grain size is not easy to determine, the average grain size of the two phases is obtained and used as the overall grain size assuming that the grain size is the same for WC and TiC. The grains of the two phases are separated and calibrated using the Image J software, and the area and perimeter of the average grain size of WC and TiC are determined, ignoring the small-size grains. The circular diameter and the shape factor of the grains are calculated based on the area and the circumference. The calculations are shown in Eqs. (2) and (3):

Equivalent circle diameter:

$$d = 2 \times \sqrt{\frac{A}{\pi}}, \quad (2)$$

grain shape factor:

$$S = \frac{4\pi A}{L^2}, \quad (3)$$

where A is the area occupied by the grains and L is the grain perimeter.

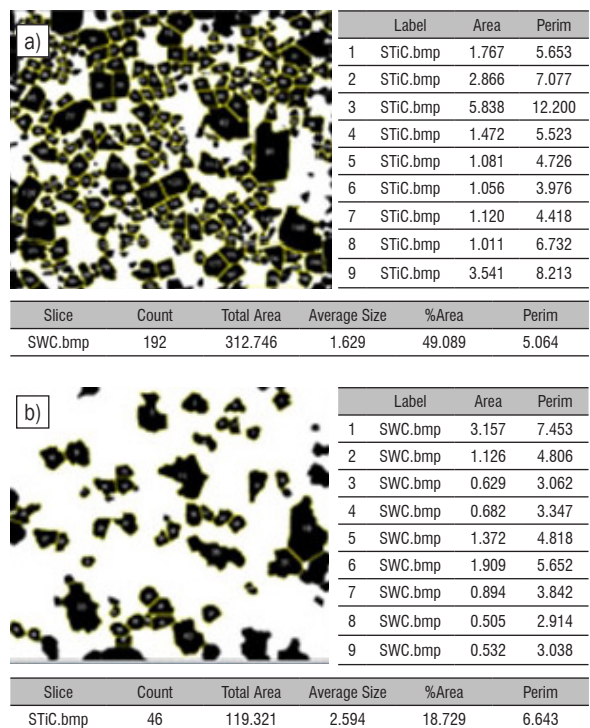


Fig. 9. WC and TiC phase area and circumference measurements of the YT5 tool; a) WC, and b) TiC

(3) Calculation of grain adjacency

It is assumed that the grains of WC and TiC have the same average size and shape. The adjacency of the grains is calculated, and it is assumed that there are only two phases in the tool material; the first is the a phase and includes WC and TiC and the second is the b phase, and it includes only Co. The adjacency is calculated using Eq. (4) [20]:

$$c = \frac{2 \sum_i L_{aa}^i}{2 \sum_i L_{aa}^i + 2 \sum_j L_{ab}^j}, \quad (4)$$

where L_{aa} is the phase boundary length between the grains of phase a and phase a in the two-dimensional image; L_{ab} is the phase boundary length of phase a and b in the two-dimensional image.

The Co phase was binarized using Image J software for the perimeter measurements, as shown in Fig. 10; the small areas are ignored, and the sum of the perimeters $\sum_j L_{ab}^j$ is calculated. Similarly, the sum of the grain perimeters of WC and TiC $2 \sum_i L_{aa}^i + 2 \sum_j L_{ab}^j$ is calculated. Then, the adjacency is calculated using Eq.(4).

	Label	Area	Perim
	1 Co.bmp	0.322	3.245
	2 Co.bmp	0.178	2.229
	3 Co.bmp	0.677	5.579
	4 Co.bmp	0.119	2.164
	5 Co.bmp	0.616	6.157
	6 Co.bmp	0.387	3.154
	7 Co.bmp	0.290	3.276
	8 Co.bmp	0.662	7.183
	9 Co.bmp	0.152	1.888

Slice	Count	Total Area	Average Size	%Area	Perim
Co.bmp	93	34.462	0.371	5.409	3.610

Fig. 10. Co-phase area and circumference measurements of the YT5 tool

The YT5 tool material parameters that were obtained using these equations are shown in Table 2.

Table 2. Main components of the YT5 cemented carbide tool

Components	TiC	WC	Co
Volume fraction	19.15	67.60	13.25
Content [wt%]	7.43	83.41	9.16
Average grain size [μm]	1.41		
Adjacency	0.74		

According to the material parameters of tool YT5 in Table2, the three-dimensional microstructure model of cemented carbide is established in ABAQUS. The modelling process is shown in the following Fig. 11.

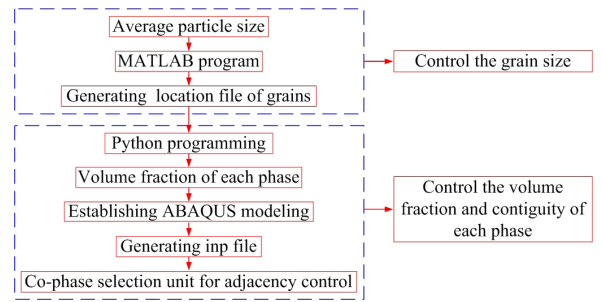


Fig. 11. Flow-chart for establishing the three dimensional micro model of the cemented carbide

In the simulation, a model size of $3 \mu\text{m} \times 3 \mu\text{m} \times 3 \mu\text{m}$ was used. To simulate the crack formation, a layer of cohesive elements was placed between the contact surfaces of the two consecutive (bulk) parts. Each phase unit consists of C3D4 elements, and the cohesive unit consists of COH3D6 elements, as shown in Fig. 12. The model of the crack propagation on the cemented carbide is established by inserting the cohesive unit, as shown in Fig. 13.

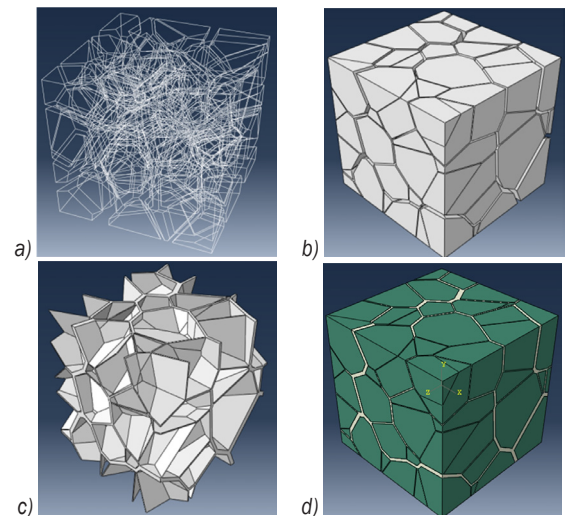


Fig. 12. ABAQUS modelling process; a) create a particle frame, b) build particle surface and body, c) insert the Co phase, and d) micro model of cemented carbide tool rake face

1.2 Constitutive Model of Cohesive Unit

The cohesive unit in ABAQUS uses the traction-separation law as the constitutive model [21], including the damage initiation criteria and damage evolution settings. The maximum stress (T_{max}) and fracture energy (G_{TC}) are chosen here as the fracture criteria because the material is a brittle material, as shown in Fig. 14. Before damage occurs to the cohesive unit, the unit is in the elastic stage, and the

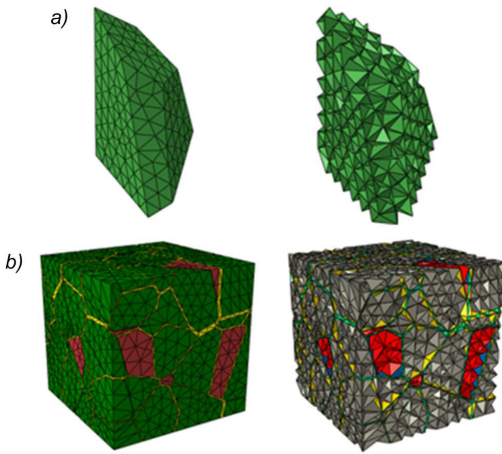


Fig. 13. Particles and integral models embedded in cohesive units; a) particles and its cohesive units, and b) integral models and their cohesive units

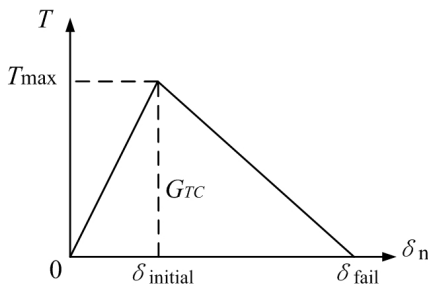


Fig. 14. Typical traction-separation response

elastic modulus at this stage is called the penalty stiffness (K_n). When the unit is subjected to tension, the two separate surfaces of the unit exhibit relative displacement, leading to the continuous increase in the internal stress. When the set maximum stress (T_{\max}) is reached, the cohesive unit begins to enter the damage stage, and the unit's stiffness starts to degrade. The stiffness of the cohesive unit in the degradation stage is quantified by ABAQUS and a damage degradation coefficient D is introduced. $D=0$ indicates that the unit has not been damaged yet and $D=1$ means that the unit's stiffness has reached zero, i.e., the unit fails, and the crack propagates. ABAQUS provides three types of stiffness degeneration: linear, exponential, and tabular; the linear stiffness degeneration is chosen here. From the bilinear criteria shown in Fig. 14, The calculations of G_{TC} and K_n are shown in Eqs. (5) and (6):

$$G_{TC} = \frac{T_{\max} \cdot \delta_{\text{fail}}}{2}, \quad (5)$$

$$K_n = \frac{T_{\max}}{\delta_{\text{initial}}}, \quad (6)$$

where δ_{initial} is the displacement of the unit at the beginning of the damage stage; δ_{fail} is the displacement of the unit at complete failure; G_{TC} is the energy required during the failure process.

ABAQUS controls the damage and fracture behaviour of the cohesive unit by setting the three parameters of K_n , T_{\max} , and G_{TC} . Because of the characteristics of the parameters in the cohesive unit, it is difficult to obtain the accurate values of these parameters using the experimental method; this is one of the main factors restricting the development of the cohesive unit. Gren established a molecular dynamics model of WC particles and analysed the binding energy of two adjacent WC particles and the binding energy when Co was present; the results showed that the binding energy of two particles was smaller in the presence of Co. The parameters of the cohesive unit used in this study are based on the studies of Gren, in which the internal binding energy of the grains was 5.76 J/m², the binding energy at the grain boundary was 3.2 J/m², and the binding energy of the particles including Co was 2.7 J/m² [22]. The maximum tensile stress of the cohesive unit is T_{\max} , which is generally assumed to be part of Young's modulus of the material. Typically, the value of T_{\max} ranges from 0.1 % to 1 % of Young's modulus [23] and [24]. In this study, a value of $T_{\max} = 0.002 \times E$ is chosen. The values of Young's modulus of the phases corresponding to the T_{\max} values of the different phase are obtained from [25], and the specific parameters are shown in Table 3. K_n is the penalty stiffness of the cohesive unit and differs from the inherent elastic modulus of the material. To ensure that the embedded cohesive unit does not affect the overall model stiffness, K_n needs to be sufficiently large, but when the value is too large, it affects the computational efficiency of the model. The value of K_n is usually calculated by the ratio of δ_{initial} and δ_{fail} , which is 0.001 in this study based on Eqs. (5) and (6).

Table 3. The values of Young's modulus of the phases corresponding to the T_{\max} values

Phase	WC	Co
Young's Modulus [GPa]	696	211

1.3 Boundary Condition

During the cutting process, the contact area of the chips and tool is divided into a close contact area and a peak contact area; the stress state of the tool material in these two regions is not the same because of the adhesion effect. In the close contact area, the wear

of the rake face occurs mainly during the continuous cutting process, whereas in the intermittent cutting process, the chips remain on the rake face due to the adhesion effect in this region when the tool is cutting. The material in this area of the tool is subject to the shear force resulting from friction with the chips. In the peak contact area, the chips are about to separate from the rake face due to upward curling and the tool material in this area is mainly subject to the tensile force that is perpendicular to the rake face as a result of the chip swing and the tool-chip adhesion.

1.3.1 Reasons for the Removal of the Rake Face Material by the Chips

- (1) Since Fe and Co belong to the same family of elements, the tool and chips form a firm connection in the molten state of the workpiece material on the rake face;
- (2) Because of the effects of high temperature and high pressure, element diffusion occurs between the tool and the workpiece material and changes the composition of the tool material; this results in the decrease in the rake face strength.
- (3) The hard phase of the rake face is broken due to the impact load on the rake face. Coupled with the high temperature of the chips, microcracks occur in the surface and sub-surface layer of the rake face, resulting in the decrease in the tool strength.

1.3.2 Location of the Adhesion Failure on the Rake Face

- (1) The location of the adhesion failure is in the close contact area between the chip and rake face and the contact area is subject to high temperature and pressure. During intermittent cutting, a strong connection between the tool and chips occurs readily, and the material of the rake face is rapidly removed by the chips as a result of frequent cutting in and cutting out.
- (2) The location of the adhesion failure is in the contact area where the chips leave the rake face. Because of chip curling and frequent oscillation of the chips during curling, the material of the rake face in this region is subject to the periodic tensile stress of the chips, coupled with temperature changes during the swing process. Tool failure or breakage can easily occur because cemented carbide tools are resistant to compression but cannot bear the tension.

1.3.3 Force Analysis of Tool-Chip Adhesion

- (1) Removal of material in the close contact area

As shown in Fig. 15, the material of the rake face is peeled off from the close contact area and is subject to F_f in the same direction as the chip flow and the normal positive pressure F_n of the material (the resultant force of the positive pressure during the cutting process and the positive pressure of the material inside the tool; when the positive pressure in the internal material of the tool is larger than that during the cutting process, the peeling of the material occurs). F is the resultant force in this area. Because of the large compressive stress applied to the peeled area, the friction force is relatively large. During the intermittent cutting process, the temperature difference solidifies the joints between the tool and chips, thereby increasing the friction. The external force at this site is only the friction force F_f between the chip and the rake face; the direction of this force is parallel to the rake face, and the material of the rake face is easily removed.

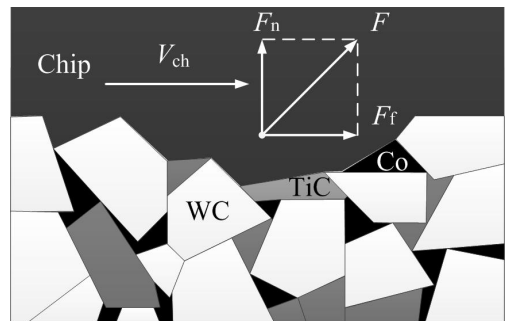


Fig. 15. Force analysis of tool-chip adhesion in the close contact area

- (2) Removal of material in the area where the chips are about to separate from the rake face

As shown in Fig. 16, when the chip material is about to leave the rake face, the peeled area is subject to the frictional force of the chips F_f and the tensile force F_t . Because the chip material on the rake face has a small positive pressure and the frictional force of the chips is much smaller in the peeled area than in the close contact area, a firm connection is formed between the tool and the chip material due to adhesion. The chip material generates a greater tensile force on the peeled area during the periodic swings; therefore, when the two external forces are combined, the direction of the force is almost perpendicular to the rake face, and the rake face material is easily removed due to the influence of the periodic tensile stress.

Based on the results of the force analysis of the adhesion layer on the rake face, two kinds of force models are used in this study. The first model is created based on the force of the adhesion layer in the close contact area, and the shear force parallel to the rake face is applied to the rake face, as shown in Fig. 17a; the direction of tangential displacement is forward along the Y-axis. The second model is created based on the adhesion layer of the future separation area between the rake face and the chip, and the tensile load is applied to the rake face, as shown in Fig. 17b; the direction of tension displacement is negative along the X-axis (red is the X-axis, green is the Y-axis, and blue is the Z-axis).

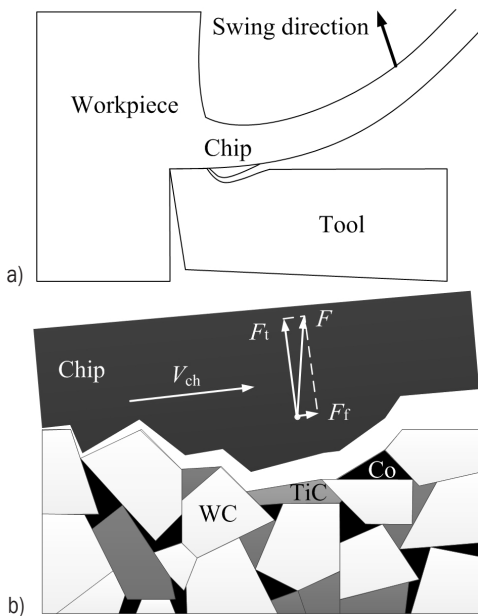


Fig. 16. Force analysis of the adhesion layer when the chips are removed from the rake face; a) schematic diagram of bond failure on the rake face during the cutting process, and b) the force condition of the cutting tool during the cutting process

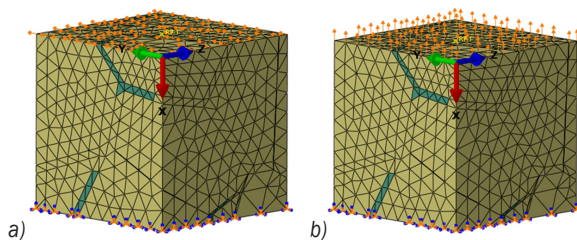


Fig. 17. Boundary condition settings; a) tangential displacement, and b) tensile displacement

2 SIMULATION RESULTS OF THE CRACK PROPAGATION

During the generation of the adhesion layer, the diffusion of the elements between the tool and the chip material affects the bonding strength between the constituent phases of the tool. Surface cracks also occur in the tool due to the thermal effect and affect the bond breakage behaviour of the tool. Therefore, the effects of the bonding strength of the different phases and the presence of initial cracks on the crack propagation are investigated.

2.1 Crack Propagation Based on Cohesion

The diffusion behaviour between the tool and chips affects the cohesive strength of the tool material, which influences the crack propagation path. Thus, the cohesive strength at the interface reflects the effect of the element diffusion on the crack propagation of the cemented carbide. It is generally assumed that the cohesive strength is lower than the grain strength. In this study, the cohesive strength is set to four levels that are 0.7, 0.8, 0.9, and 1.0 times the original cohesive strength. The grain fracture energy G_{TC} of the transgranular fracture can be expressed as [26]:

$$G_{TC} = \gamma_s, \quad (7)$$

where γ_s is the surface energy of the matrix grain per unit area [J/m^2].

When the Co structure is close-packed hexagonal (hcp), γ_s is $2.55 J/m^2$ [27]. In the cemented carbide, the Co structure is face-centred cubic (fcc), which has better plasticity than the hcp structure; therefore, the Co fracture energy setting is 1/3 larger than the reference value ($6.8 J/m^2$). This provides a more realistic model. The specific parameters are shown in Table. 4.

The simulation results under different cohesive strength are shown in Fig. 18. The simulation diagram indicates that the crack propagation paths extend along the WC-Co interface and the WC-WC interface under the four types of cohesive strength. When the cohesive strength is 0.7 times and 0.8 times the cohesive strength of the particles, the crack propagation path, which extends along the bonding surface with a relatively weak cohesive strength, is basically the same and the crack propagation surface is perpendicular to the load direction. When the cohesive strength is 0.9 times the cohesive strength of the particles, the crack propagation path is deflected around the stronger bonding surface due to the increase in the cohesive strength between the local

particles. When the cohesive strength is 1.0 times the cohesive strength of the particles, the edges of the local particles are fragmented due to the local increase in the cohesive strength between the particles.

Table 4. Parameters of the cohesive strength

Type of cohesive units	Grade	Fracture energy G_{TC} [J/m ²]	Maximum stress T_{max} [GPa]	Penalty stiffness K_n [GPa/m]
WC Co WC-WC WC-Co	0.7	5.76	1.39	1.68×10^{11}
		6.8	0.42	1.30×10^{10}
		3.2	0.97	1.47×10^{11}
		2.7	0.29	1.56×10^{10}
	0.8	5.76	1.39	1.68×10^{11}
		6.8	0.42	1.30×10^{10}
		3.2	1.112	1.93×10^{11}
		2.7	0.336	2.09×10^{10}
	0.9	5.76	1.39	1.68×10^{11}
		6.8	0.42	1.30×10^{10}
		3.2	1.251	2.45×10^{11}
		2.7	0.378	2.65×10^{10}
1.0	1.0	5.76	1.39	1.68×10^{11}
		6.8	0.42	1.30×10^{10}
		3.2	1.39	3.02×10^{11}
		2.7	0.42	3.27×10^{10}

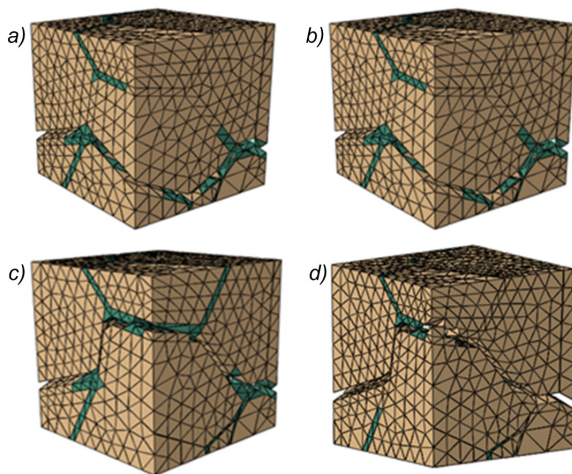


Fig. 18. Crack propagation path within the unit cells under tensile displacement for different cohesive strength; a) 0.7 times, b) 0.8 times, c) 0.9 times, and d) 1.0 times

The crack propagation through the WC particles does not occur during the simulation process, and the initial crack is enlarged as shown in Fig. 19. The cracks initiate from the WC-Co interface and extend to the WC-WC interface in the tensile state. When the WC-WC interface strength is equal to or slightly less than the particle strength, the direction of the crack

propagation is locally deflected; however, due to the occurrence of multiple cracks, the crack still expands and bridges along the relatively weak interface of the cohesive strength, eventually resulting in a fracture.

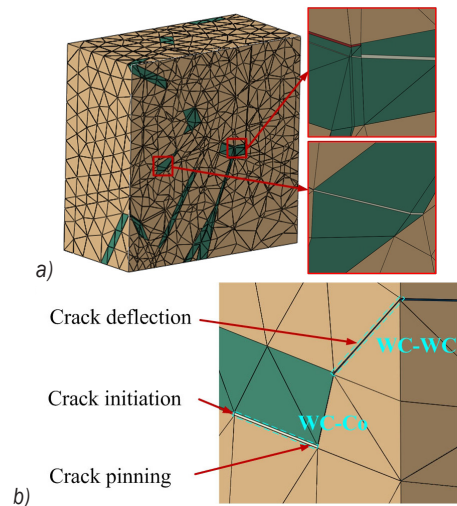


Fig. 19. Crack initiation and propagation; a) crack initiation, and b) crack propagation

2.2 Crack Propagation in the Absence of an Initial Crack

The simulation model is used in the ABAQUS display solver for analysis and calculation. The crack propagation paths of the model under different modes of loading are shown in Figs. 20 and 21. The crack propagation under a friction load imposed by applying a tangential displacement to the cemented carbide rake face is shown in Fig. 20, and the crack propagation under tensile displacement is shown in Fig. 21. The stress unit in Figs. 20 and 21 is 10^3 GPa.

According to Griffith's crack propagation theory [28], the crack initiation usually occurs in a material with internal defects or weak internal strength and cracks always propagate along the direction of highest energy dissipation. As can be seen from Figs. 20 and 21, the process of crack initiation is well simulated by the model. The crack initiation sites in the model are located at the WC-Co grain boundary where the cemented carbide is weakly bonded, and the crack propagation path is along the two-phase interface. The crack surface is perpendicular to the applied load direction, which is consistent with the results obtained by previous research [5]. At the same time, the changes in the stress during the crack propagation can be observed, and the maximum stress increases with the crack growth due to the extrusion deformation of the local grid. In the model without the presence of cracks, the stress distribution is not uniform under a

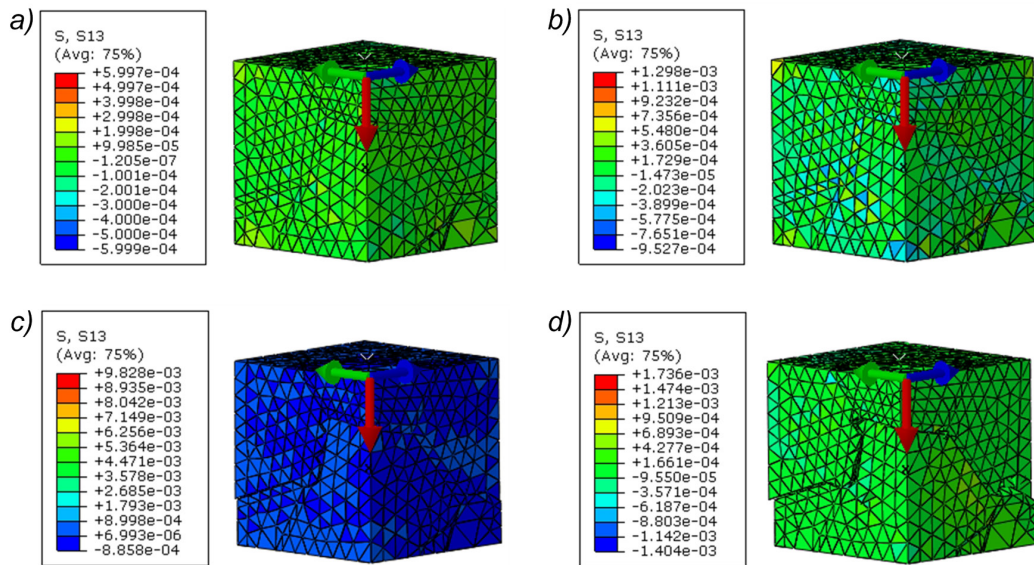


Fig. 20. Crack propagation under the effect of a tangential displacement; a) initial state, b) crack initiation, c) crack propagation, and d) final fracture

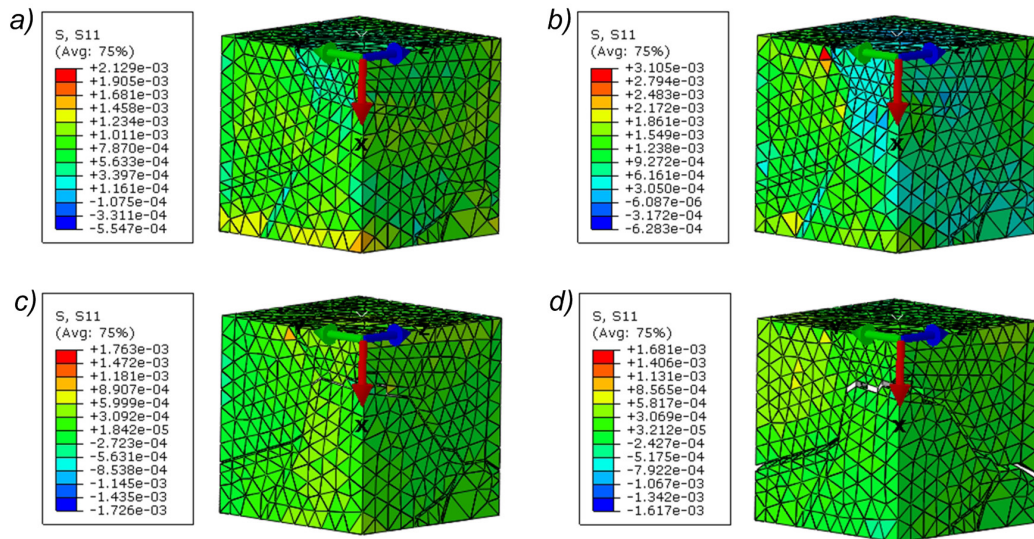


Fig. 21. Crack propagation under the effect of a tensile displacement; a) initial state, b) crack initiation, c) crack propagation, and d) final fracture

load, and the stress in the binder phase is generally lower. In contrast, in the model where cracks are present, the stress distribution tends to be uniform in most regions of the model, except for the part of the grid with the highest stress due to over-deformation.

2.3 Crack Propagation in the Presence of Initial Cracks

The rake face of the carbide tool is prone to cracking under the conditions of high temperature and high pressure, and the cracks on the tool rake face may

occur in the WC particles, the WC-WC bonding surface, and the WC-Co bonding surface. A simulation is conducted to systematically investigate the effect of the crack location on the crack propagation path in the cemented carbide. We focus on the adhesive layer produced by the rake face during the cutting process of the carbide tool and the peeling of the adhesive layer during the chip removal is simulated and analysed. Subsequently, cracks are added to the model, and the simulation study is conducted for two different crack locations.

2.3.1 Single Crack

2.3.1.1 Crack Location in the WC Particles

(1) The position, angle, and load direction of the prefabricated crack are shown in Fig. 22. The crack is located in the WC particles, and the length is about half the average size of the WC particles. Three cases of crack directions are investigated. In the first case, the crack surface is parallel to the rake face; in the second case, the crack plane is 45° to the rake face; in the third case, the crack surface is perpendicular to the rake face. The results of the crack propagation for the three cases are shown in Fig. 23. It is evident that the crack propagation process is similar when the prefabricated crack plane forms an angle of 0° and 45° with the rake face. The crack first expands from the WC-Co interface and the prefabricated cracks

and then forms multiple cracks; subsequently, the cracks join and eventually create fractures, which are transgranular and intergranular fractures. When the prefabricated crack plane is perpendicular to the rake face, the prefabricated crack has little effect on the crack propagation path and the crack propagates from the WC-Co interface and the WC-WC interface without passing through the WC particles.

(2) As shown in Fig. 24, a tangential load is applied in the model of the prefabricated crack. It can be seen from Fig. 25 that the crack propagation path is more sensitive to the 0° and 45° cracks and the propagation path of the crack passes through the two kinds of prefabricated cracks, whereas for the 90° crack, the prefabricated crack has little effect on the crack propagation path.

By comparing Fig. 25 and Fig. 20, Fig. 23 and Fig. 21 respectively, it turns out that when there

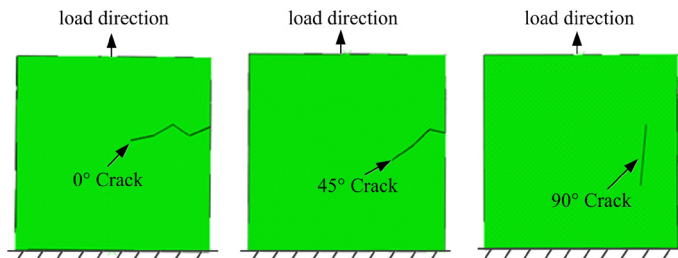


Fig. 22. Location of the crack angle in the WC particles and model load under a tensile displacement

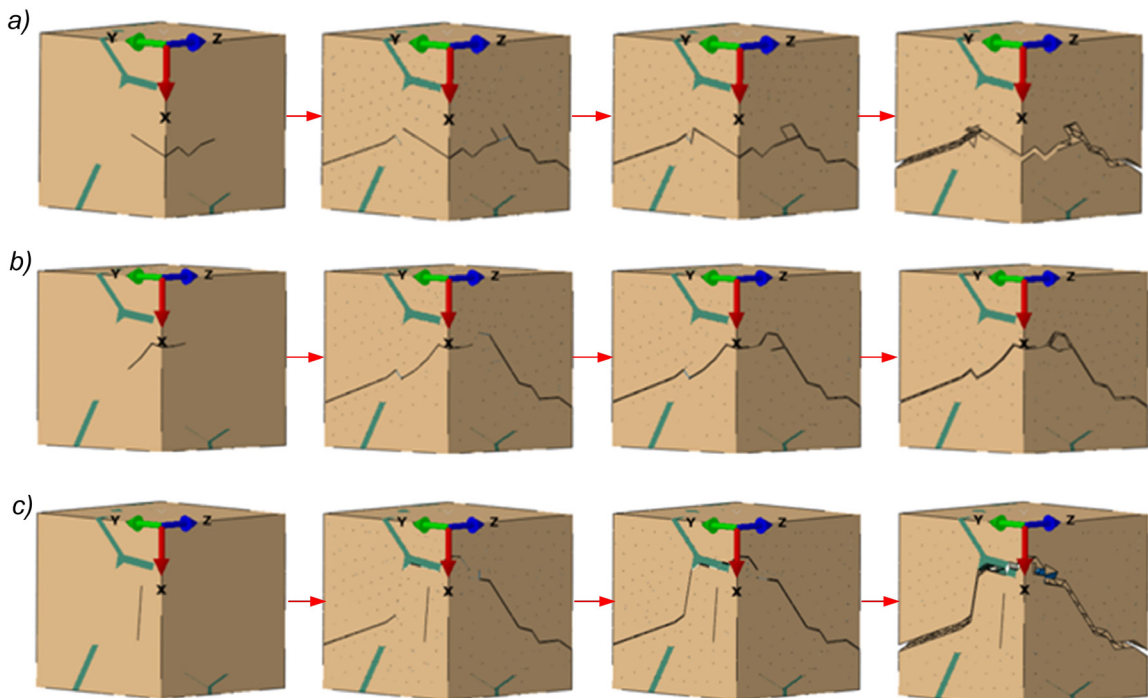


Fig. 23. Crack propagation under a tensile displacement: a) 0° crack, b) 45° crack, and c) 90° crack

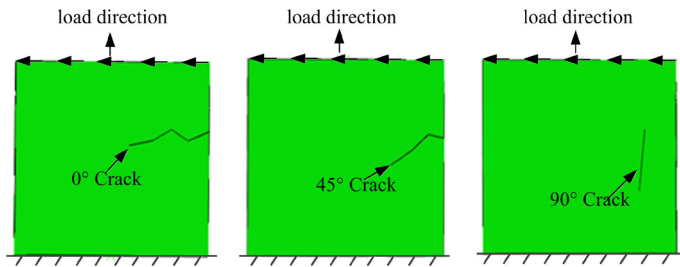


Fig. 24. Location of the crack angle in the WC particles and model load under a tangential displacement

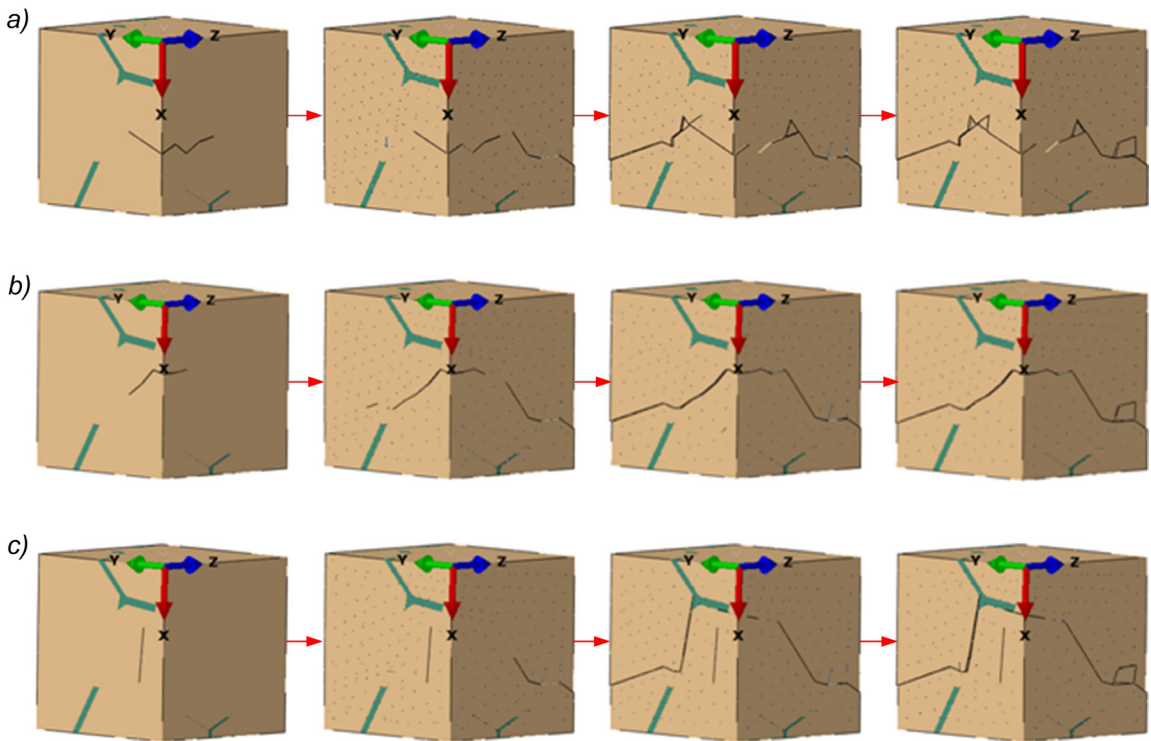


Fig. 25. Crack propagation under a tangential displacement: a) 0° crack, b) 45° crack, and c) 90° crack

is a crack in the WC particles in the adhesive layer of the carbide tool rake face, the adhesive layer is peeled off under the combined action of friction and the tool-chip force. The direction of the initial crack has a significant influence on the crack propagation path, which in turn affects the peeling volume of the adhesive layer, i.e., the larger the peeling volume, the faster the tool failure rate is and the shorter the tool life is due to the bond breakage. The analysis of the simulation results shows that the initial crack surface that is parallel to the rake face or at an angle of 45° to the rake face has a greater impact on the crack propagation path, whereas the initial crack that is perpendicular to the rake face has less of an effect on the crack propagation path.

2.3.1.2 Crack Location at the WC-Co and WC-WC Interfaces

As shown in Fig. 26, a uniaxial tensile load was applied to the model. The cracks are distributed at the WC-Co and WC-WC interfaces and mainly propagated along the grain boundaries. Fig. 26 shows

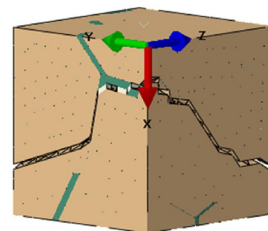


Fig. 26. Original crack propagation path

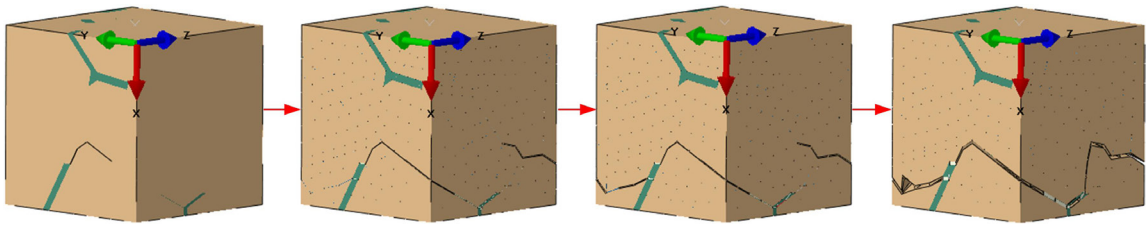


Fig. 27. Crack propagation paths of prefabricated cracks

the original crack propagation path. The intergrain cracks change the original crack propagation path, which can be seen from a comparison of Figs. 26 and 27.

2.3.2 Multiple Cracks

To further investigate the crack propagation paths, a number of prefabricated cracks are applied in the model to simulate the crack propagation for multiple cracks; Fig. 28 shows that 0° , 45° , and 90° cracks are applied in the model. A uniaxial tensile load is applied, and the simulation results are shown in Fig. 29.

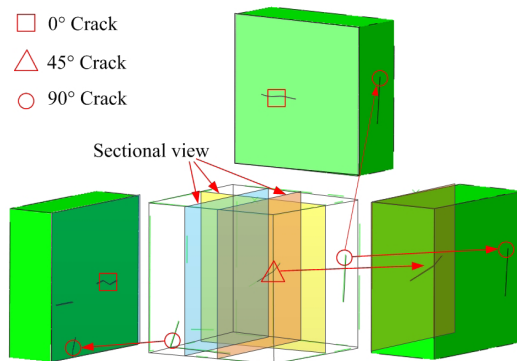


Fig. 28. Different crack distributions

The simulation results indicate that the crack propagation process is a self-expansion process of a single crack and the interconnection between the cracks. It can be seen from the fracture surface of the model that the crack propagation paths of multiple cracks pass through many prefabricated cracks. Although the crack perpendicular to the rake face is prefabricated in the WC particles, the crack still does not extend through the WC particles. For multiple cracks, the crack propagation path mainly passes through the prefabricated cracks at the WC-Co and WC-WC boundaries and due to the pinning action of the local particles, the cracks join, and the fracture occurs by bypassing the position with a higher bonding strength, resulting in the peeling of the adhesive layer.

A crack represents a form of energy release. When the energy inside the system accumulates to a certain extent and cannot be released, cracks reduce the energy and balance the system. The direction of crack propagation is in the direction of the highest energy dissipation. For uniform materials under a tensile load, the cracks tend to expand along the direction perpendicular to the load, whereas for composite materials, the crack propagation path is deflected and bypasses areas of higher bonding strength due to the local non-uniformity of the material; therefore, the energy is released more quickly.

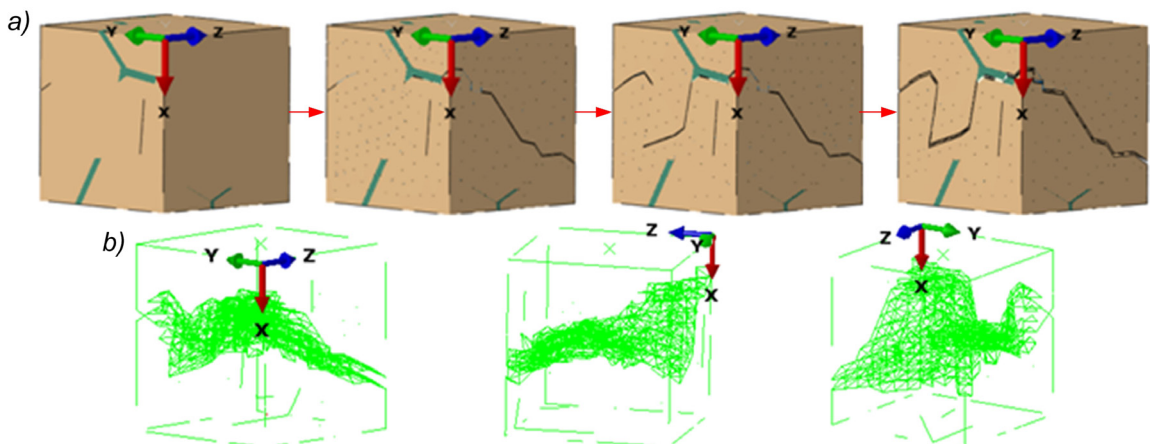


Fig. 29. Simulation results of multiple initial cracks; a) crack propagation process, and b) the fracture surface at different view angles

2.4 Effect of Crack on Tensile Strength

As shown in Fig. 30, the tensile strength of the model under different cohesive strength values is analysed. The tensile strength of the model varies greatly for different cohesion values, and the tensile strength increases with the increase in the cohesive strength of the cemented carbide. Therefore, increasing the combined force of the two phases helps to increase the strength of the cemented carbide.

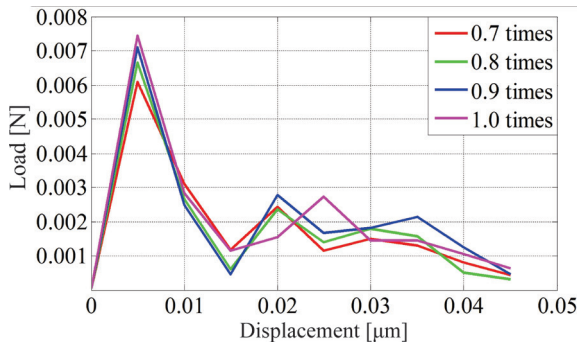


Fig. 30. Load-displacement curves of the unit cell under tensile load for different cohesive strength values

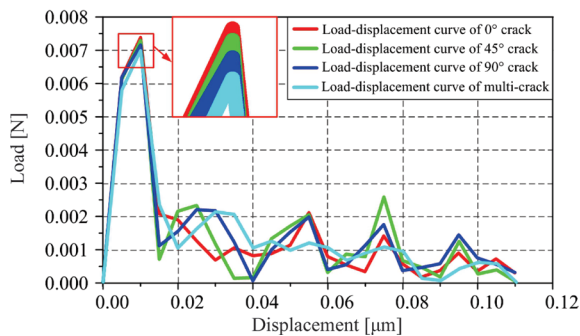


Fig. 31. Load-displacement curves of the unit cell under tensile load for different initial cracks

As shown in Fig. 31, the tensile strength in the presence of cracks is analysed in the model, and the maximum tensile load at the same position is obtained under different crack conditions. The differences in the tensile loads are small due to the small extent of the model. An analysis of the maximum tensile load shows that the presence of single cracks does not always reduce the tensile strength of the cemented carbide. Due to the stronger cohesive strength, the energy required for crack propagation is higher when the crack is in the interior of the particle and the local plastic zone at the tip of the crack has a pinning effect on the crack propagation. As a result, the tensile strength is increased and the maximum tensile load exhibits an overall increase. Due to the difference

in the tensile and shear strengths of the particles, the tensile strength shows some differences for the different crack angles. Under normal circumstances, the probability of crack occurrence within the WC particles is small; therefore, this condition has a minimal effect on the tensile strength of the material and can be ignored. When multiple cracks exist initially, the cracks appear at the WC-Co and WC-WC boundaries, and the increase in the number of these cracks reduces the tensile strength of the cemented carbide, which makes the material more prone to fracturing under a tensile load.

3 EXPERIMENTAL

A SEM is used to observe the bond breakage of the tool and the surface morphology of the pits on the tool's rake face after the adhesive layer is peeled off; the results are shown in Fig. 32. It is evident that the surface of the WC particles in the tool is relatively intact and some of the particles are exposed; this shows that the form of adhesive layer peeling consists mainly of an intergranular fracture. This indicates that the experimental results are similar to the simulation result.

The location and the proportion of sub-surface cracks or holes in the carbide cutting tool face can be observed to determine the crack propagation path of the adhesive layer and roughly estimate the volume of the peeled-off material and the service life of the tool. This provides data for follow-up research.

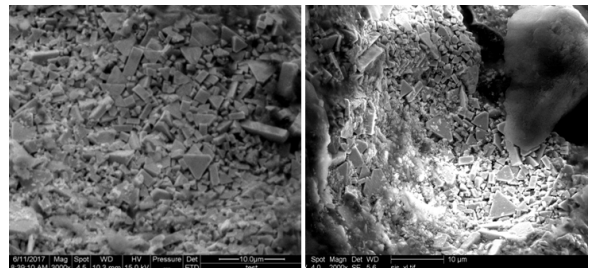


Fig. 32. Surface morphology after the peeling-off of the adhesive layer

4 CONCLUSIONS

Based on the simulation results and the tool-chip adhesion process, the following conclusions can be drawn:

- (1) For different cohesive strength values, the cracks are deflected by the increase in the combined force of the local particles. In the absence of an initial crack, the inner crack of the carbide

propagates along the bond plane of the WC-Co, and the crack propagation plane is generally perpendicular to the load direction.

- (2) The bond breakage of the cemented carbide tool's rake face occurs in conjunction with the crack occurrence. For a single crack, the initial crack surface parallel to the rake face or at an angle of 45° to the rake face has a large effect on the crack propagation path for the three types of initial cracks in the WC particles. When the initial crack is perpendicular to the rake face, there is only a small effect on the crack propagation path. For the cracks that are located in the WC-Co and WC-WC interfaces, the initial crack mainly changes the original crack propagation path.
- (3) When multiple cracks are present initially, the crack propagation path mainly passes through the prefabricated cracks and the WC-Co and WC-WC boundaries. Due to the pinning effect of the local particles, the cracks join and bypass the areas of high bonding strength to eventually produce a fracture, resulting in the peeling of the adhesion layer. The experimental results show that the particle surface is relatively intact after the cemented carbide is damaged, which indicates that an intergranular fracture occurred. This is consistent with the simulation results
- (4) In the absence of cracks, the stronger the cohesive strength of the carbide, the greater the tensile strength of the material is. When there is a crack in the cemented carbide, the crack propagation and crack pinning increases the tensile strength of the material to some extent; however, the increase in the number of intergranular cracks reduces the overall tensile strength of the material, which makes the material more prone to fracture.

5 ACKNOWLEDGEMENTS

The authors would like to thank the support of the National Natural Science Foundation of China (Grant No.51575146) and the Education and Research Project for young and middle-aged teachers of Fujian Province (Grant No.JAT170506).

6 NOMENCLATURES

A_V	area ratio, [-]
A	area, [μm^2]
c	grain adjacency, [-]
d	diameter, [μm]
D	damage degradation coefficient, [-]
E	Young's modulus, [GPa]

F	resultant force vector, [N]
F_f	friction force, [N]
F_n	normal positive pressure force, [N]
F_t	tensile force, [N]
G_{TC}	fracture energy, [J/m^2]
K_n	penalty stiffness, [GPa/m]
L	grain perimeter, [μm]
S	grain shape factor, [-]
T_{\max}	max stress, [GPa]
V_{ch}	cutting speed, [m/min]
V_V	volume ratio, [-]
δ_{initial}	the displacement at the beginning of the unit damage, [μm]
δ_{fail}	the displacement of the unit at the complete failure, [μm]

7 REFERENCES

- [1] Sun, F.L., Li, Z.J., Chen, B. (1997). Research on mechanism of adhering between chip and tool cutting 2.25Cr-1Mo steel. *Journal of Harbin University Ofence & Technology*, vol. 2, no. 5, p. 1-3, DOI:10.15938/j.jhust.1997.05.001. (in Chinese)
- [2] Cheng, Y.-N., Liu, X.-L., Li, Z.-J., Liu, L., Wang, H.-T. (2012). Adhering failure of the tool-chip in the process of extremely heavy cutting. *Chinese Journal of Mechanical Engineering*, vol. 48, no. 19, p. 169-176, DOI:10.3901/JME.2012.19.169. (in Chinese)
- [3] Tan, G.-Y., Liu, G.-J., Li, Z.-J., Liu, M.-J., Li, G.-H., Rong, Y.-M. (2004). 3D temperature field analysis and fuzzy comprehensive evaluation for milling insert with complex groove. *Chinese Journal of Mechanical Engineering*, vol. 40, no. 3, p. 106-110, DOI:10.3321/j.issn:0577-6686.2004.03.021. (in Chinese)
- [4] Gurland, J. (1963). The fracture strength of sintered tungsten carbide-cobalt alloys in relation to composition and particle spacing. *Transactions of the Metallurgical Society of AIME*, vol. 227, p. 1146-1150.
- [5] Editorial committee, Foreign cemented carbides. (1976). Foreign cemented carbides. Metallurgical Industry Press, Beijing. (in Chinese)
- [6] Sigl, L.S., Exner, H.E. (1987). Experimental study of the mechanics of fracture in WC-Co alloys. *Metallurgical Transactions A*, vol. 18, no. 7, p. 1299-1308, DOI:10.1007/BF02647199.
- [7] Ljungberg, A. B., Chatfield, C., Hehenberger, M., Sundstrom, B. (1986). Estimation of the plastic zone size associated with cracks in cemented carbides. *Proceedings of the Second International Conference on the Science of Hard Materials*, p. 619-630.
- [8] Fischmeister, H.F., Schmauder, S., Sigl, L.S. (1988). Finite element modelling of crack propagation in WC-Co hard metals. *Materials Science & Engineering: A*, vol. 105-106, p. 305-311, DOI:10.1016/0025-5416(88)90711-2.
- [9] Hönle, S. (1998). *Micromechanical Modelling of Deformation and Fracture of Graded WC-Co Hard Metals*, MSc thesis, University of Stuttgart, Stuttgart.

- [10] Connolly, P., McHugh, P.E. (2002). Fracture modelling of WC-Co hard metals using crystal plasticity theory and the Gurson model. *Fatigue & Fracture of Engineering Materials & Structures*, vol. 22, no. 1, p. 77-86, DOI:10.1046/j.1460-2695.1999.00153.x.
- [11] McHugh, P.E., Connolly, P.J. (2003). Micromechanical modelling of ductile crack growth in the binder phase of WC-Co. *Computational Materials Science*, vol. 27, no. 4, p. 423-436, DOI:10.1016/S0927-0256(03)00045-4.
- [12] Kim, C.S. (2004). *Microstructural-Mechanical Property Relationships in WC-Co Composites*, MSc. thesis, Carnegie Mellon University, Pittsburgh.
- [13] Kim, C.-S., Massa, T.R., Rohrer, G.S. (2006). Modeling the relationship between microstructural features and the strength of WC-Co composites. *International Journal of Refractory Metals and Hard Materials*, vol. 24, no. 1-2, p. 89-100, DOI:10.1016/j.ijrmhm.2005.04.011.
- [14] Park, S. (2007). *Development of a Microstructure-Level Finite Element Model for the Prediction of Tool Failure by Chipping in WC-Co Systems*, MSc. thesis, University of Illinois at Urbana-Champaign, Urbana-Champaign.
- [15] Sadowski, T., Nowicki, T. (2008). Numerical investigation of local mechanical properties of WC/Co composite. *Computational Materials Science*, vol. 43, no. 1, p. 235-241, DOI:10.1016/j.commatsci.2007.07.030.
- [16] Carlsson, K. (2013). *Modeling of Three Dimensional Microstructures Including Grain Boundary Mechanisms*, MSc. thesis, Chalmers University of Technology, Gothenburg, p. 10-20.
- [17] Park, S., Kapoor, S.G., DeVor, R.E. (2006). Microstructure-level model for the prediction of tool failure in WC-Co cutting tool materials. *Journal of Manufacturing Science and Engineering*, vol. 128, no. 3, p. 739-748, DOI:10.1115/1.2194233.
- [18] Park, S., Kapoor, S.G., DeVor, R.E. (2007). Microstructure-level model for the prediction of tool failure in coated WC-Co cutting tool materials during intermittent cutting. *Journal of Manufacturing Science and Engineering*, vol. 129, no. 5, p. 893-901, DOI:10.1115/1.2738507.
- [19] GB/T-6394:2002. *Metal-Methods for Estimating the Average Grain Size*. Standardization Committee of China, Beijing. (in Chinese)
- [20] Zhu, J.-F., Zhang, L., Xu, T., Zhang, Z.-J., Liu, X.-Z., Wang, Z. (2015). Quantificational characterization of microstructural parameters of cemented carbides based on Image J software. *Materials Science and Engineering of Powder Metallurgy*, vol. 20, no. 1, p. 26-31. (in Chinese)
- [21] Abaqus Analysis User's Manual (2011). *Defining the Constitutive Response of Cohesive Elements using a Traction-Separation Description*, vol. 4, sec. 31.5.6. SIMULIA, Providence.
- [22] Gren, M. (2013). *Molecular Dynamics Simulations of Grain Boundaries in Cemented Carbides*, MSc. thesis, Chalmers University of Technology, Gothenburg.
- [23] Tomar, V. (2008). Analyses of the role of the second phase SiC particles in microstructure dependent fracture resistance variation of SiC-Si₃N₄ nanocomposites. *Modelling and Simulation in Materials Science and Engineering*, vol. 16, no. 3, p. 1-17, DOI:10.1088/0965-0393/16/3/035001.
- [24] Xu, X.-P., Needleman, A. (1994). Numerical simulations of fast crack growth in brittle solids. *Journal of the Mechanics and Physics of Solids*, vol. 42, no. 9, p. 1397-1434, DOI:10.1016/0022-5096(94)90003-5.
- [25] MatWeb (2011). Engineering Materials Database Business, from <http://www.matweb.com/services/services.aspx>, accessed on 2011-4-4.
- [26] Jiao, S., Jenkins, M.L., Davidge, R.W. (1997). Interfacial fracture energy-mechanical behaviour relationship in Al₂O₃/SiC and Al₂O₃/TiN nanocomposites. *Acta Materialia*, vol. 45, no. 1, p. 149-156, DOI:10.1016/S1359-6454(96)00168-1.
- [27] de Boer, F.R., Boom, R., Mattens, W.C.M., Miedema, A.R., Niessen, A.K. (1989). *Cohesion in Metals*. North Holland, Amsterdam.
- [28] Griffith, A.A. (1921). The phenomena of rupture and flow in solids. *Philosophical Transactions of the Royal Society A*, vol. 221, no. 582-593, p. 163-198, DOI:10.1098/rsta.1921.0006.

LDM COMPACT – A Methodology for Development of Gas Engines for Use with Low Environmental Impact Non-Natural Gas

Igor Šauperl¹ – Andreas Wimmer² – Dimitar Dimitrov¹ – Jan Zelenka¹ –
Gerhard Pirker¹ – Eduard Schöneßl¹ – Hubert Winter¹

¹ LEC GmbH, Austria

² Graz University of Technology, Institute of Internal Combustion Engines and Thermodynamics, Austria

LDM COMPACT is a methodology, which permits the development of highly efficient combustion concepts for non-natural gas (NNG) engines without extensive testing on a multi-cylinder engine as well as tailor-made engine solutions for the special characteristics of NNG (LDM stands for LEC Development Methodology). Starting with a description of the baseline LDM, which incorporates the general approach for efficient engine development, this paper introduces the improved approach of LDM COMPACT and outlines each of the required steps, i.e., the preselection and basic design of essential engine parameters based on simulation, fundamental experiments on special test rigs, and experimental optimization of the concept on a single cylinder research engine. The fundamentals and main innovative features of the methodology are discussed. Two recent development projects (combustion of blast furnace gas and combustion of flare gases) are provided as examples of its application. In these examples, extensive use of simulation to evaluate different engine configurations permitted a significant share of optimization work to be completed in advance. The pre-optimized concepts were tested and validated on a single cylinder research engine. By applying LDM COMPACT, it was possible to develop the combustion concepts in a short amount of time and implement them into the multi-cylinder engine directly on-site.

Keywords: methodology, gas engines, combustion concept, non-natural gas, blast furnace gas, flare gas

Highlights

- A novel methodology for the development of combustion systems for engines fuelled by non-natural gas (NNG) is presented.
- The methodology relies on the combination of simulation, fundamental experiments and optimization of the concept on a single cylinder research engine.
- Combustion systems using NNG can be developed on the single cylinder engine and transferred to the multi-cylinder engine without extensive further testing.
- Recent results of successful application examples for waste gases (blast furnace gas and flare gas) are presented.
- The methodology facilitates the exploitation of waste gases at low cost, thus, enabling energy production with low environmental impact.

0 INTRODUCTION

The use of gas engines fuelled by non-natural gases (NNG) for power generation and heat is key to exploiting resources in a more environmentally friendly manner and achieving a general reduction in CO₂ emissions, Fig. 1. NNG encompasses landfill gas, flare gas, coal mine gas, sewage gas, biogas and a variety of other special gases. This group of special gases includes, above all, waste gases from industrial processes (e.g., gases from steel production). These gases are often used inefficiently or not at all to produce (thermal) energy. Large bore gas engines are best suited to exploit these waste gases.

Created during the steel production process, blast furnace gas (BFG) is a good example of a waste gas that would otherwise not be exploited that could be used to operate a gas engine. Another type of waste gas is flare gas that leaks from petroleum refineries, natural gas processing plants, and oil or gas production

sites. The energy content of flare gas can also be used for power generation and to operate the plant itself. In general, NNG vary widely in their composition depending on where and how they are produced and how much is produced.

Due to their particular characteristics, each of these gases requires a specially designed engine concept. Gas engines that burn NNG are normally more difficult to operate than those that run on natural gas (NG), mainly because of the greatly fluctuating gas compositions and the intermittent availability of these gases. The gas properties that vary, for example, lower calorific value and methane number, require very robust combustion concepts and sophisticated monitoring and control strategies. An overview of the wide variety of compositions of gaseous fuels including NNG used in combustion engines can be found in [1]. Research [2] provides examples of gas engine applications that use waste gases. An engine series capable of burning non-

natural gases is presented in [3] and [4]. These papers describe the engine concept, the design features, and the special adaptations of the engine for use with non-natural gases. Furthermore, [5] also presents the latest advances in NNG applications from simulation to single cylinder testing to the final customer applications.

Compared to conventional natural gas engines, which are often sold in large quantities, most NNG engine applications start off as individual solutions. On account of the very specific characteristics of each NNG, a specially designed engine concept is required for each gas. Due to the low production figures for engines that run on NNG, natural gas engines are modified for this application with the least amount of development effort, which results in disadvantages in efficiency and performance. Combustion system development of a multi-cylinder engine (MCE) on the site where the gas is produced is in most cases not economically viable. Consequently, these challenges prevent the expedient use of NNG. Likewise, the combustion system development of a multi-cylinder engine on the test bed of the engine manufacturer is equally unfeasible from an economic perspective. In this case, the factor that drives costs is the fuel since it must be mixed together from the main components. In addition, fuel consumption by the multi-cylinder engine is very high. The lower the number of engines initially expected for commercialization, the more economic concerns become aggravated. With gases with unfavourable properties, implementation is only possible if the cost of development is limited.

Given these boundary conditions, it is critical to employ a method for the economically viable design and optimization of a combustion concept for gas engines that apply to a wide variety of NNG. To achieve sufficient economic viability, it is vital that the method does not require testing on a multi-cylinder engine and that the result obtained from simulation and single cylinder engine measurements can be transferred directly to the on-site facility without any additional multi-cylinder engine tests.

It should be feasible to use the methodology with niche applications in which only a small number of engines are produced. It allows optimization of the combustion concept to be well directed and combined with an adapted control concept to achieve high-efficiency values and competitive mean effective pressures even with gases with unfavourable properties, such as large shares of inert gases or low calorific value. By enabling combustion system and controls optimization, this methodology can extend the applicability of large gas engines to NNG, thereby contributing to the environmentally sound and efficient exploitation of NNG. As a result, the application of the methodology described in this paper significantly reduces CO₂ emissions and consumption of natural gas from fossil fuels.

1 APPROACH

1.1 Baseline Methodology

The classic LEC development methodology (LDM) was elaborated in order to support efficient engine

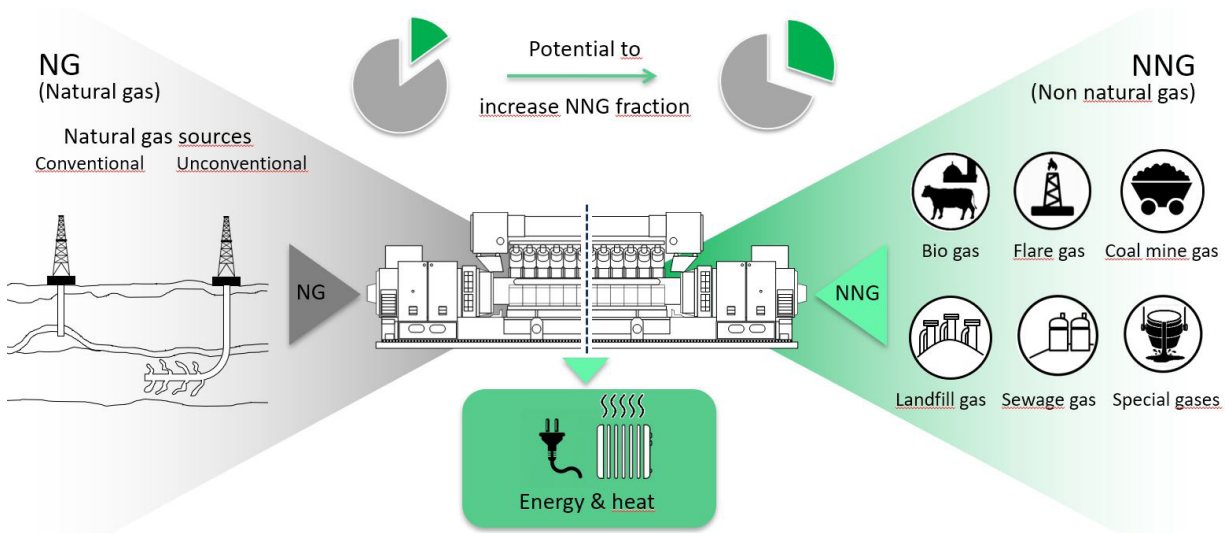


Fig. 1. Low-emission energy production that maximizes the use of non-natural gases

development [6] and [7]. It is a general methodology for developing and optimizing combustion concepts for large engines and is based on an intensive interaction between simulation and experimental investigation of single-cylinder research engines (SCE). Since its creation, many manufacturers and research institutions have come to rely on this method, which has established itself as the standard for large engines [8] to [10]. A more holistic approach to general performance and emissions development is described in [11] and applied in [12]; the key features are also intensive use of various simulation tools, a model-based development approach as well as experiments on a single-cylinder research engine. The use of a single-cylinder research engine as a tool for combustion system development can be regarded as a generally recognized approach [13].

Like the classic methodology, the improved methodology makes use of 0D and 1D engine cycle simulation as well as 3D CFD (3-dimensional computational fluid dynamics) simulation. While 3D CFD simulation is employed above all to optimize the details of relevant processes (e.g., piston geometry, charge motion), 0D/1D engine cycle simulation is applied to pre-optimize significant engine parameters (e.g., compression ratio, valve timing). In addition to the basic development of combustion concepts for steady-state engine operation, the methodology comprises integrated treatment of all combustion-related processes such as durability, wear, ignition and fuel supply as well as the development of transient combustion concepts and controls.

1.2 Improved Methodology

The main innovation of the approach presented in this paper is the further enhancement of LDM to meet the requirements for the development of NNG combustion concepts: LDM COMPACT methodology can be applied to development processes that are carried out without extensive testing on a multi-cylinder engine. These processes primarily rely on simulation tools as well as measurements on a single-cylinder research engine; they can be directly transferred to the engine operator's facility, Fig. 2.

LDM COMPACT consists of two basic steps:

- preselection and basic design of essential engine parameters based on simulation,
- experimental optimization of the concept on a single cylinder research engine.

1.3 Determining of Engine Parameters

To preselect the combustion concept including all required parameters, each gas composition is first characterized by determining several characteristic values. These values include knock index, laminar flame speed, and the density and lower calorific value of the gas composition.

First, an appropriate knock index must be selected. Various knock detection criteria can be applied depending on the fuel gas composition. These criteria yield major differences, especially for gas mixtures that contain hydrogen or higher hydrocarbons [14] and [15]. Knock occurs when the remaining fresh charge is suddenly consumed as ignition conditions are reached. In lean burn gas engines, knocking is monitored using the in-cylinder pressure signal (if available) by applying appropriate algorithms that focus on the sudden superposition of the in-cylinder pressure signal by high-frequency pressure oscillations [16] to [18].

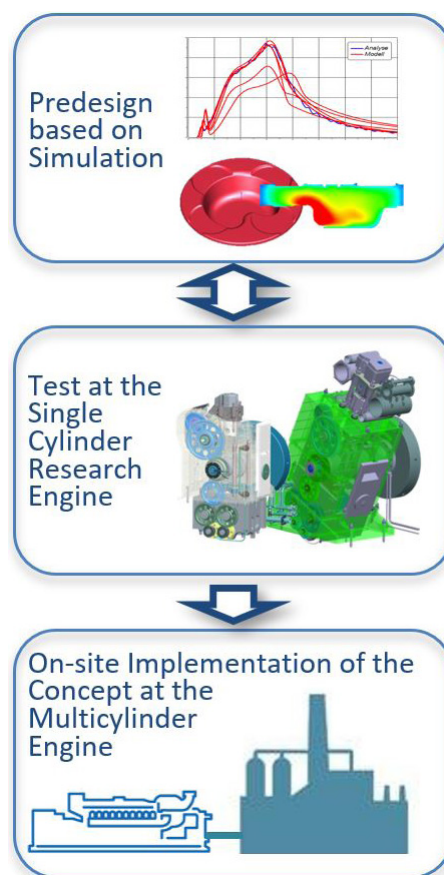


Fig. 2. LDM Compact

After the knock criterion is selected, the expected laminar flame speed of the gas composition under investigation has to be determined [19] by either performing experiments or making reaction kinetic calculations. Experimentally determined laminar flame speeds of methane-air mixtures [20], reference fuels (e.g., n-heptane, iso-octane) [21] and alternative gaseous fuels [22] are available in the literature. Most of the experimental values stated in the literature are measured at ambient conditions; however, some are relevant at engine conditions. In any case, to obtain values for engine-related operation areas, extrapolations should be avoided so as to prevent major inaccuracies. Instead, reaction kinetics calculations are performed to determine the laminar flame speed. However, these calculations are possible only if an appropriate reaction mechanism exists for the specific gas composition. Such a mechanism is often not available for NNG due to their highly specific compositions. To obtain reasonable values for NNG, it is possible to make flame propagation measurements in a rapid compression expansion machine (RCEM) under different conditions (pressure and temperature) and with different gas mixtures. This data can also be applied to characterize flame front propagation and to validate reaction kinetics and combustion models. Fig. 3 shows a rapid compression expansion machine with a highly flexible optical access. In the combustion chamber, different pressure and temperature conditions can be achieved. A gas mixing device (up to 10 components) allows investigation of a variety of gas mixtures.



Fig. 3. Rapid compression expansion machine (RCEM) with a highly flexible optical access

After all the properties required for gas characterization have been determined, the combustion concept can be preselected. The possible concepts and the basic engine parameters are

listed systematically in a table according to the gas category. 0D and 1D engine cycle calculations are then conducted to describe the operating parameters in detail. Trends are quickly estimated with the 0D simulation methodology, which uses models that calculate ignition delay, burn rate, NO_x formation and knocking. Gases with a very high share of inert gas components typically have extremely small lower calorific values and thus very challenging characteristics. Stable and efficient combustion of such gases requires a high degree of turbulence in the combustion chamber. In certain applications, the laminar flame speed of NNG compared to that of pure CH₄ is very small because of the high inert proportion of CO₂ in some NNG. In these cases, it is preferable to increase the turbulence level in the combustion chamber in order to obtain higher reaction rates and subsequently accelerate the combustion process with the result of acceptable efficiency at low emission levels. To increase the turbulence level, an adequate combustion chamber design is necessary. 3D CFD simulation is applied to design and optimize the combustion chamber geometry. Based on the results from 3D CFD simulation, it can be decided whether the gas composition under investigation requires a combustion system with a prechamber or whether it can be operated in an open chamber combustion system. 3D CFD simulation is also preferable for pre-designing the combustion chamber geometry in order to avoid locations where knocking might occur; this is especially important with gases with very challenging compositions as well as gases that have a low calorific value. Further simulations are conducted to determine an appropriate excess air ratio (EAR) for the derived combustion concept so that the emission limits for nitric oxides are met. With each gas, the maximum load possible under the previously defined boundary conditions is determined, thereby ensuring stable, robust and knock-free combustion.

1.4 Experimental Optimization of the Concept

A very efficient and flexible test bed infrastructure was set up for experimental investigations on a single cylinder research engine. Progressive developments in the areas of gas mixing (up to 6 different gas components), gas supply, gas storage and safety technology enable testing of almost any gas composition on the single cylinder research engine. After the required engine components have been procured, the relevant engine operating areas are typically determined in a screening phase. To reduce test time when determining the optimal

parameters, intensive use is also made of statistical design of experiments (DoE) methods. The focus of experimental investigations is on determining the efficiency and load potential of each gas while at the same time achieving the lowest possible emissions. Sensitivity observations that consider fluctuations in gas quality are also carried out. These fluctuations are critical to the design of an engine control concept and to the determination of whether higher quality gases need to be added. The results of this iterative process of just simulation and single-cylinder research engine measurements are ultimately used to directly implement the concept into the on-site multi-cylinder engine, Fig. 3.

The main innovation of the methodology presented here is that it improves the characterization of different gases and simulation possibilities to the point that a very advanced combustion concept for each gas can be achieved in combination with experimental development on the single cylinder research engine. As a result, it is finally economically viable to implement the concept in a variety of applications of NNG that could otherwise not be exploited. Critical to the development of the methodology are both the systematic evaluation of basic gas components with regard to their influence on knock behaviour and the derivation of a catalogue of basic combustion concepts selected based on prior NNG developments.

2 APPLICATION EXAMPLES FOR THE DEVELOPMENT OF COMBUSTION CONCEPTS FOR WASTE GASES

The development methodology presented in this paper is the result of many years of research and several successful projects at the LEC that have developed NNG combustion concepts for large gas engines that are almost exclusively concerned with sustainable solutions for energy production and transportation. The available database consists of several thousand measurements of different single cylinder research engines. The following section presents two examples of the development of combustion concepts for sustainable power generation in large gas engines that efficiently and flexibly exploit blast furnace gas (BFG) and flare gases.

2.1 Combustion of Blast Furnace Gas

Blast furnace gas (BFG) is an important yet difficult-to-exploit by-product of the steelmaking process. The objective was to develop a highly efficient, high power output combustion concept for a large gas

engine in the 4 MW power range using blast furnace gas [23]. This concept must comply with the TA Luft emission limits, ensure sufficient combustion stability despite fluctuations in gas quality and exhibit good starting behaviour. As on-site development on the multi-cylinder engine was not feasible due to the reasons stated in the previous section, the innovative development methodology was applied.

2.1.1 Selection and Pre-Optimization of the Combustion Concept Using Simulation

In the first step, a suitable concept for the combustion of BFG was selected and pre-optimized mainly with simulation. The extremely unfavourable properties of BFG, which contains a large share of inert gases and whose calorific value is lower than 1 kWh/m³, require a very specific combustion concept. Large gas engines may employ pre-chamber concepts that are gas scavenged, mixture scavenged or un-scavenged as well as open chamber concepts. Engines of the size selected for the development of this combustion system are normally equipped with prechambers. However, 0D/1D simulation revealed that ignition could not be successfully induced due to the unfavourable mixture composition in the pre-chamber at ignition timing. This finding was obtained before any experiments were conducted by determining the mixture composition in the pre-chamber at ignition timing with a 1D simulation model. Based on the conditions in the pre-chamber, the simulation provides a detailed description of the mass overflow between the pre-chamber and the main combustion chamber. Thus, the main focus of combustion system development was on the open chamber concept. With this type of concept, a sufficient level of turbulence induced by charge motion must be achieved to obtain an appropriate flame speed. To achieve this level of turbulence in the combustion chamber during combustion, a very high swirl level was combined with an appropriate piston shape. 3D CFD simulation was extensively used during the optimization process.

Fig. 4 presents selected results from this process. The locally averaged turbulent kinetic energy (TKE) was chosen to evaluate the different variants.

The chart shows the optimized variant as well as two intermediate development steps (variants A and B) in relation to the baseline variant. Based on these investigations, the most promising piston shapes in combination with the swirl level were determined and preselected for experimental tests on the single-cylinder research engine. Further information on this study can be found in [24].

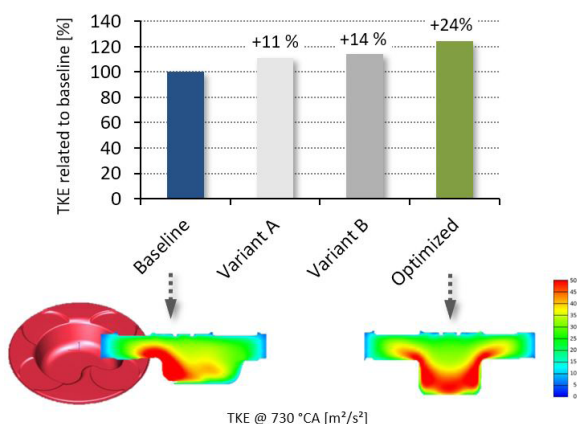


Fig. 4. Predesign of the combustion concept using 3D CFD simulation [24]

2.1.2 Experimental Development on the Single Cylinder Research Engine

Measurements were taken on a single cylinder research engine to verify the simulation results and to determine certain engine performance values (e.g., efficiency, emission level, combustion stability). Combustion chamber variants with increased turbulent kinetic energy had a shortened combustion duration, which resulted in significantly faster fuel conversion with the optimized variant. After the best piston variant had been chosen and the optimal compression ratio determined, the engine operating parameters (e.g., ignition timing, mixture temperature, charge pressure) were optimized. The goal was to obtain the largest operating range possible, i.e., the range between knock limit and misfire limit, which is crucial for robust gas engine operation.

The fluctuations in the composition of blast furnace gas cause dramatic changes in the combustion behaviour of the gas. If the share of hydrogen (H_2), in particular, noticeably varies, combustion is greatly impacted. Thus, investigations were carried out on the single cylinder research engine to evaluate the sensitivity of the engine concept to fluctuations in H_2 content. Figs. 5 and 6 present selected results of these investigations with the optimal variant; the misfire limit and the knock limit restrict the operating range. While Fig. 5 depicts the achievable engine efficiency versus load and H_2 content, Fig. 6 shows combustion stability versus the same parameters. Further information on these investigations can be found in [25]. The fundamentals that the study is based on can be found in [26].

A special control concept adapted to the blast furnace gas application was developed for the multi-

cylinder engine in order to ensure stable engine operation with variable load and fluctuating gas quality. Through continuous optimization of both combustion and gas mixing, a maximum energy yield can be guaranteed at any time and at any operating point. The simulation-based control concept relies upon on-board cylinder pressure measurement and admixing of an additional gas (e.g., coke gas).

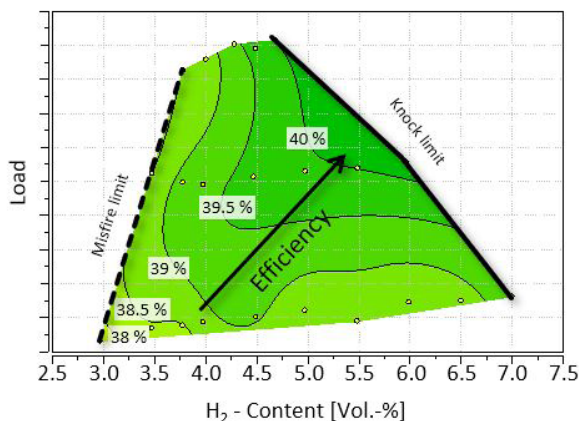


Fig. 5. Operating range: Efficiency versus load and H_2 content [25]

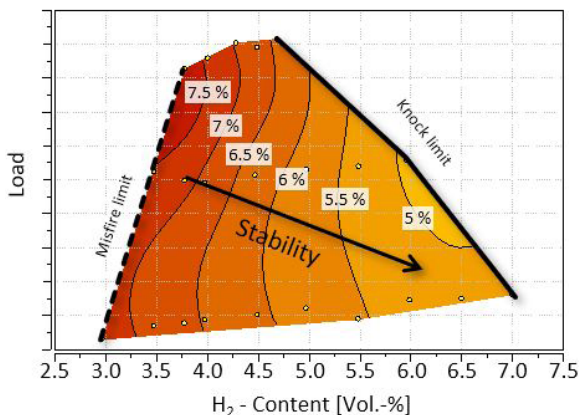


Fig. 6. Operating range: Combustion stability versus load and H_2 content [25]

2.2 Combustion of Flare Gases

As previously stated, a large amount of energy is lost from the flaring of waste gases from oil and gas production. According to [27], 150 billion cubic metres of natural gas resources are wasted each year worldwide by flaring, thereby generating the equivalent of 400 million metric tons of CO_2 greenhouse gas emissions. Instead of flaring these gases, efficient use of their energy content should be pursued.

Besides methane, flare gases originating from oil production contain a great share of nitrogen and carbon dioxide as well as ethane, propane and other higher hydrocarbons.

For the investigations conducted in this example, three representative gas compositions feasible for power generation with large gas engines were selected based on their gas properties, which are mainly characterized by different methane numbers in order to be comparable to pure methane.

2.2.1 Combustion Concept Predesign using Simulation

In the first step, 0D and 1D engine cycle simulation was applied to pre-select the combustion concept and define basic engine parameters such as compression ratio and pre-chamber volume. The simulation of certain engine operating parameters and limits such as exhaust gas temperature enabled the selection of potential hardware variants in the process of combustion concept predesign. 1D modelling is especially useful for investigating temperature and charge composition in the pre-chamber at ignition timing; these two parameters are critical to the ignition of the mixture. An important parameter for robust and stable ignition as well as NO_x formation, the excess air ratio (EAR) in the pre-chamber can be controlled by regulating the amount of gas that flows through the gas valve into the pre-chamber. Pre-chamber size and compression ratio are also important parameters. Fig. 7 compares the excess air ratio traces of three different gas scavenged pre-chambers: a baseline configuration, a pre-chamber with a larger volume and a pre-chamber with double the amount of energy. 3D CFD methods are applied to predetermine the combustion in detail. The rate of heat release history that results from 3D CFD simulation is then used in 1D simulation.

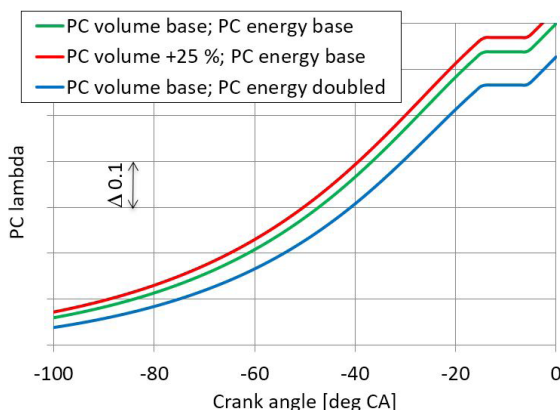


Fig. 7. Excess air ratio in the pre-chamber calculated with 1D simulation

Similar results can be obtained by applying 0D simulation alone. The advantage of 0D simulation is its short calculation times. Due to the missing gas exchange calculation, however, the initial values have to be estimated. Therefore, it is feasible to apply 0D simulation for determining the EAR in the pre-chamber within the methodology loop after the first measurement results are available. Improved boundary conditions for simulation can be derived from the measurements.

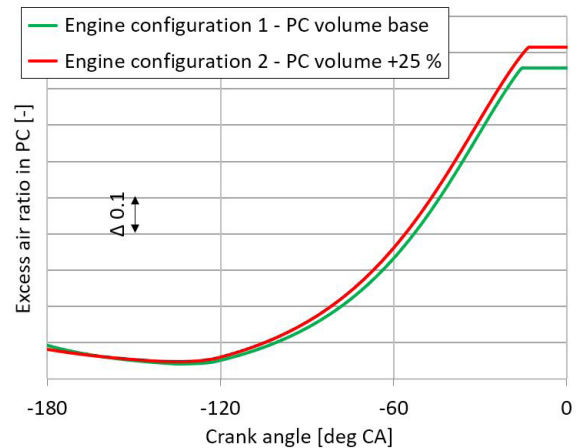


Fig. 8. Excess air ratio (EAR) in the pre-chamber calculated with 0D simulation

While Fig. 7 shows the 1D simulation results, Fig. 8 shows the 0D simulation results for the baseline pre-chamber and the pre-chamber with increased volume. The EAR with the larger pre-chamber is higher due to the flow of more of the lean mixture from the main chamber into the pre-chamber. Furthermore, the ignition timing is slightly retarded, which results in a longer mixing time.

2.2.2 Experimental Development on the Single Cylinder Research Engine

Since the simulation-based predesign process revealed that a scavenged pre-chamber combustion concept is the most feasible solution, such a concept was chosen for the experimental investigations on the single-cylinder research engine. Three different engine configurations were chosen to validate knock tendency and determine the maximum load possible with each gas composition. These configurations differ in terms of compression ratio and pre-chamber volume.

The first step of the testing process involved performing a load variation in order to determine the maximum achievable brake mean effective pressure

(BMEP) at a certain NO_x level limited by knocking combustion. The combustion timing (represented by the centre of gravity of combustion) was kept constant with all the gas compositions to ensure good comparability. Fig. 9 shows the measurement procedure that was applied. From a baseline of approximately 50 %, the load was continuously increased until the knock limit was reached. At constant combustion timing, the engine load can be further increased by leaning out the mixture, which leads to reduced NO_x emissions. Taking into account the further constraints of the misfire limit and exhaust gas temperature limit, the procedure was continued until either 10 % overload operation was reached or a NO_x emission level of 250 mg/nm^3 was achieved. Further information on these investigations can be found in [28].

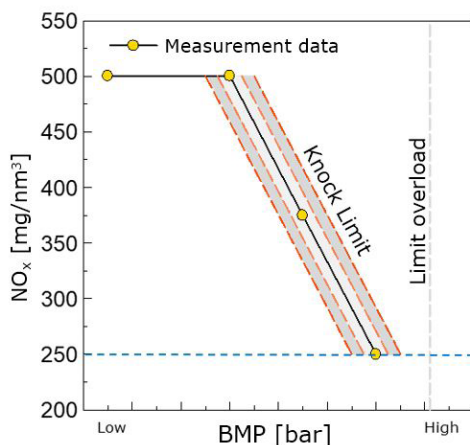


Fig. 9. Maximum achievable BMEP limited by knocking [28]

Although it cannot be guaranteed that full load operation is possible with all NNG, the tests of the selected gas compositions showed that in the cases considered, full load operation could be achieved by varying the excess air ratio and ignition timing (IT). Fig. 10 shows the operating ranges obtained with the three gas compositions.

Based on these results, it can be concluded that state-of-the-art combustion concepts for large gas engines are able to provide a sufficiently large operating range when they operate with the gas compositions of the flare gases that were investigated. Furthermore, with all three of the selected engine configurations, overload operation as well as compliance with the TA Luft [29] emission level of 500 mg/nm^3 of NO_x were possible with all the gas compositions. It was shown that a high hydrogen content in the fuel gas significantly shifts the misfire limit to lower NO_x

emission levels. An increased engine compression ratio can further widen the operating window because the exhaust gas temperature decreases, and the lean limit is shifted to even lower NO_x emissions.

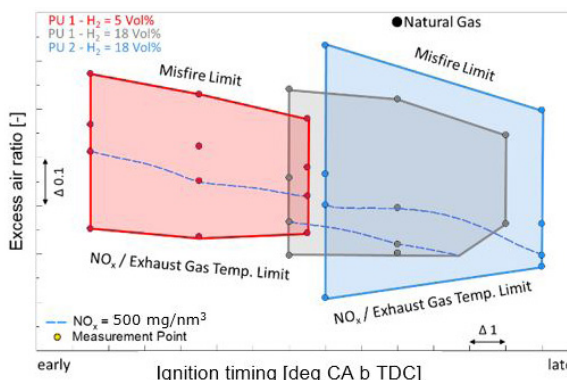


Fig. 10. Operating range of selected gas compositions

As shown in Fig. 3, simulation and measurement interact closely. The development methodology provides a loop that reuses the results from the single-cylinder research engine measurements to improve the simulation or to gain further insight into the processes being investigated. On the one hand, the measurement results serve to validate and optimize 3D CFD simulation models so that new piston shapes or pre-chamber designs can be developed. On the other hand, when the 1D simulation model is supported by measurement results, important parameters that cannot be measured can be determined by simulation.

3 OUTLOOK AND POTENTIAL

On a global level, there is enormous potential for economically and ecologically viable implementation of NNG applications into large gas engines. For example, the losses from drilling for natural gas alone are estimated to be about 5 % of global natural gas production [27]; these losses arise to a great extent from the flaring of components unable to be directly exploited. In terms of CO_2 emissions, this translates into almost 400 million tons of CO_2 [27] that could be saved by exploiting these gases for energy. Even if only a small fraction is saved, the potential is extremely high. Operation of gas engines with a variety of NG and NNG is contingent upon the adaptation of a combustion concept that runs on the type of gas currently in use. Developing individual combustion concepts for each gas is a time-consuming and cost-intensive process. LDM COMPACT combines state-of-the-art 0D/1D and 3D simulation tools and experiments on the single-cylinder research

engine test bed and allows direct implementation of an engine concept into the on-site multi-cylinder engine without prior cost-intensive tests on a multi-cylinder engine. In this way the methodology is an important enabler for the implementation of technologies for the energy production with a low environmental impact.

4 ACKNOWLEDGEMENTS

The authors would like to acknowledge the financial support of the “COMET – Competence Centres for Excellent Technologies Programme” of the Austrian Federal Ministry for Transport, Innovation and Technology (BMVIT), the Austrian Federal Ministry of Science, Research and Economy (BMWFW) and the Provinces of Styria, Tyrol and Vienna for the K1-Centre LEC EvoLET. The COMET Programme is managed by the Austrian Research Promotion Agency (FFG).

5 REFERENCES

- [1] Merker, G.P., Schwarz, Ch., Teichmann, R. (eds.) (2012). *Combustion Engines Development*. 6th ed., Springer, Berlin, Heidelberg, DOI:10.1007/978-3-642-14094-5.
- [2] Amplatz, E., Schneider, M., Trapp, C. (2011). Utilization of special gases in stationary gas engines, 6. *Internationale MTZ-Fachtagung*, DOI:10.1365/s40353-011-0009-2.
- [3] Ernst, A., Sander, U., Kibele, C., Odermatt, M., Wasgindt, A. (2011). The New MTU Series 4000 for Non-Natural-Gas Applications, 7th *Dessau Gas Engine Conference Proceedings*.
- [4] Sander, U., Ernst, A., Kibele, C., Odermatt, M., Wasgindt, A. (2010). Die neue MTU Baureihe 4000 für Biogasanwendungen. *MTZ- Konferenz Heavy Duty-, On- und Off- Highway-Motoren*. (In German)
- [5] Prankl, S., Trapp, C., Böwing, R., Zuschnig, A., Schiestl, S., Schneßl, E., Wimmer, A. (2016). Fortschritte bei Sondergasen - GE Gasmotoren mit hoher Leistung für wasserstoff- und kohlenmonoxidreiche Gase, *Die Zukunft der Großmotoren IV*, p. 227-243. (in German)
- [6] Wimmer, A., Winter, H., Schnessl, E., Pirker, G., Dimitrov, D. (2011). Combustion concept development for the next generation of GE Jenbacher gas engines. 7th *Dessau Gas Engine Conference*.
- [7] Wimmer, A., Pirker, G., Schnessl, E., Trapp, C., Schaumberger, H., Klinkner, M. (2012). Assessment of simulation models for the development of combustion concepts for the new generation of large gas engines. 10th *International Symposium on Combustion Diagnostics*.
- [8] Auer, M., Friedrich, C., Waldenmaier, U., Knafl, A., Stiesch, G. (2013). Combustion development methodology for MAN diesel & turbo large bore gas engines. 14th *The Working Cycle of the Internal Combustion Engine Conference*.
- [9] Schlemmer-Kelling, U., Hamm, T., Reichert, E., Struckmeier, D. (2013). FEV single cylinder engine family for large engine applications of MAN. 22nd *Aachen Colloquium Automobile and Engine Technology*.
- [10] Trapp, Ch. (2013). The future of gas engines – A technology comparison with diesel engines in the light of legislation and market. 14th *The Working Cycle of the Internal Combustion Engine Conference*.
- [11] Murakami, S. (2016). Holistic approach for performance and emission development of high speed gas and dual fuel engines. *CIMAC Proceedings*, paper no. 273.
- [12] Murakami, S., Baufeld, T. (2013). Current status and future strategies of gas engine development. *CIMAC Proceedings*, paper no. 413.
- [13] Menzel, F., Seidel, T., Schmidt, W., Pape, J., Stiegler, L. (2006). Einzylindermotor als Werkzeug zur Entwicklung neuer Brennverfahren. *Motortechnische Zeitschrift MTZ*, vol. 67, no. 3, p. 168-173, DOI:10.1007/BF03226771.
- [14] Zelenka, J., Kammel, G., Pichikala, K.C., Tritthart, W. (2017). The quality of gaseous fuels and consequences for gas engines. 10. *Internationale Energiewirtschaftstagung*. (in German)
- [15] Wimmer, A., Chmela, F., Kirsten, M., Pirker, G., Christiner, P., Trapp, C., Schaumberger, H. (2013). LEC-GPN – a new index for assessing the knock behavior of gaseous fuels for large engines. *Knocking in Gasoline Engines*, p. 239-254.
- [16] Worret, R. (2002). *Zylinderdruckbasierte Detektion und Simulation der Klopfgrenze mit einem verbesserten thermodynamischen Ansatz*. PhD. Thesis, University of Karlsruhe, Karlsruhe. (in German)
- [17] Dimitrov, D., Chmela, F., Wimmer, A. (2005). Eine Methode zur Vorausberechnung des Klopfverhaltens von Gasmotoren. 4. *Dessauer Gasmotoren Konferenz*. (in German)
- [18] Dimitrov, D., Strasser, Ch., Chmela, F., Wimmer, A. (2006). Vorhersage des Klopfverhaltens für Groß-Gasmotoren mit Direktzündung oder Vorkammer. 2. *Tagung Klopfregelung für Ottomotoren – Trends für Serienentwickler*. (in German)
- [19] Hann, S., Urban, L., Grill, M., Bargende, M. (2017). Influence of binary CNG substitute composition on the prediction of burn rate, engine knock and cycle-to-cycle variations. *SAE International Journal of Engines*, vol. 10, no. 2, p. 501-511, DOI:10.4271/2017-01-0518.
- [20] Hu, E., Li, X., Meng, X., Chen, Y., Cheng, Y., Xie, Y., Huang, Z. (2015). Laminar flame speeds and ignition delay times of methane air mixtures at elevated temperatures and pressures. *Fuel*, vol. 158, p. 1-10, DOI:10.1016/j.fuel.2015.05.010.
- [21] Jerzembeck, S., Peters, N., Pepiot- Desjardins, P., Pitsch, H. (2009). Laminar burning velocities at high pressure for primary reference fuels and gasoline: Experimental and numerical investigation. *Combustion and Flame*, vol. 156, no. 2, p. 292-301, DOI:10.1016/j.combustflame.2008.11.009.
- [22] Park, O., Veloo, P.S., Liu, N., Egolfopoulos, F.N. (2011). Combustion characteristics of alternative gaseous fuels. *Proceedings of the Combustion Institute*, vol. 33, no. 1, p. 887-894, DOI:10.1016/j.proci.2010.06.116.
- [23] Schneßl, E., Pirker, G., Wimmer, A. (2009). Optimierung von Brennverfahren für Sondergasanwendungen auf Basis der Simulation und Versuch am Einzylinder-Forschungsmotor. *MTZ-Konferenz Heavy Duty-, On- und Off-Highway-Motoren*. (in German)

- [24] Schneßl, E., Wimmer, A., Prankl, S. (2018). Combustion development methodology for non-natural gas applications. MTZ industrial, **DOI:10.1007/s40353-018-0002-0**.
- [25] Zauner, S., Arnold, G., Kopecek, H., Kumar, C., Spreitzer, C., Trapp, C., Schneßl, E., Wimmer, A. (2014). Großgasmotorenkonzepte für Gase mit extrem niedrigem Heizwert. 3. Rostocker Großmotoren Tagung. (in German)
- [26] Schneßl, E., Kogler, G., Wimmer, A. (2009). Großgasmotorenkonzepte für Gase mit extrem niedrigem Heizwert. 6. Dessauer Gasmotoren Konferenz. (in German)
- [27] Farina, M.F. (2010). Flare gas reduction – Recent global trends and policy considerations. GE White Paper, from http://www.ge-spark.com/spark/resources/whitepapers/Flare_Gas_Reduction.pdf.
- [28] Zelenka, J., Kirsten, M., Schneßl, E., Kammel, G., Wimmer, A. (2017). LDM Compact – An efficient methodology for the development of combustion concepts for non-natural gas. MTZ-Konferenz Heavy Duty-, On- und Off-Highway-Motoren.
- [29] Federal Ministry for Environment (2002). *Nature Conservation and Nuclear Safety: "Technical Instructions on Air Quality Control – TA Luft"* of 24 July 2002.

The Importance of Friction Coefficient between Vehicle Tyres and Concrete Safety Barrier to Vehicle Rollover - FE Analysis Study

Jovan Trajkovski* – Miha Ambrož – Robert Kunc

University of Ljubljana, Faculty of Mechanical Engineering, Slovenia

The most important mechanical factors in an impact scenario of a vehicle into a concrete safety barrier are vehicle speed, the impact angle, the static stability factor of the vehicle as well as the concrete safety barrier design and conditions. Concrete safety barriers (CSBs) are primarily designed to minimize vehicle damage by allowing a vehicle to be lifted when riding up on the lower slope and then redirected back onto the road. In some cases, though, the vehicle-CSB contact might end with a rollover, often with fatal consequences. To reduce the rollover risk, different concrete barrier shapes were designed in the past, while omitting the importance of the friction coefficient between the tyre and barrier. Therefore, the aim of this paper is to research and emphasize the importance of the friction coefficient between vehicle tyres and a CSB in rollover accidents. For that purpose, a series of finite element analyses were performed using different values of the friction coefficient between vehicle tyres and a CSB. Experimental measurements of the coefficient of friction between the rubber and CSB blocks of different surface were additionally performed in dry and wet conditions in order to examine the real onsite friction characteristics. The results show that the coefficient of friction can have a crucial impact in vehicle rollover scenarios and should therefore be kept as low as possible by the CBS manufacturers and maintainers.

Keywords: concrete safety barrier, rollover, friction, simulation, finite element method

Highlights

- Vehicle-concrete safety barrier (CSB) crash analyses were performed using finite element models.
- Rubber-CSB coefficient of friction was experimentally measured for aged and new blocks.
- Vehicle tyres-CSB coefficient of friction has a significant impact on a vehicle rollover.
- Vehicles with higher centre of gravity are prone to rollover upon collision with common CSBs.

0 INTRODUCTION

According to the World Health Organization (WHO), over 3,400 people die on the world's roads every day and tens of millions of people are injured or disabled every year, 90 % of which belong to low income countries [1]. In the European (EU) countries, the number of road deaths (55,000) has been reduced by 43 % between 2001 and 2010 and additionally reduced by 17 % until 2015 [2]. After two years of stagnation, the number of deaths was reduced again in 2016 by 2 %. Although the European roads are the safest in the world [2], a lot more has to be done to achieve the "vision zero" in road fatalities.

One aspect of traffic safety assurance is separating the vehicles driving in opposite directions by means of traffic barriers providing physical lane separation. An ideal traffic barrier would redirect a vehicle back into its traffic lane safely enough to allow the driver to take control of the steering, avoiding secondary accidents. According to Gabler and Gabauer [3], in vehicle-to-traffic barrier crashes, more than 25 % of all fatalities involve a rollover. Therefore, it is very important to reduce the rollover risk during vehicle collisions with safety barriers.

Concrete safety barriers (CSBs) have greatly increased the traffic safety since their first usage in New Jersey, U.S., in 1955 [4]. In Europe, they first appeared in Belgium and France in the 1970s as a replacement for the guardrail steel structures [4]. They have long lifetime and require almost no maintenance while offering a relatively high degree of safety. CSBs are designed as median barriers to prevent vehicles crossing into the opposite traffic lanes or as roadside barriers to protect the traffic from roadside obstacles. They are used on major city roads, ring roads, and limited-width highways to reduce the consequences passengers suffer in the event of an accident [5]. These roads are characterised as high-traffic roads, and it is therefore important to ensure fluent and safe traffic while minimising the traffic congestion. In Slovenia as well as in other EU countries, the existing steel safety barriers are often replaced with CSBs due to the limited space available for widening [6]. In some specific situations, the CSBs in combination with other factors such as vehicle type, road and tyre conditions, vehicle speed, impact angle and driver reaction can cause a vehicle rollover, which may have fatal consequences to the vehicle occupants [7]. For that purpose, considerable research effort has

*Corr. Author's Address: University of Ljubljana, Faculty of Mechanical Engineering, Aškerčeva c. 6, Ljubljana, Slovenia, jovan.trajkovski@fs.uni-lj.si

been devoted to improving and optimising the profile of concrete traffic barriers [8] to [11]. McDevit [8] designed the so-called F-shape concrete barrier in order to improve the safety characteristics of the New Jersey barriers. The need to have a more consistent performance than that of a vertical face concrete wall led to the development of constant slope barriers [8]. Albuquerque and Sicking [12] evaluated the in-service safety performance of safety shaped (New Jersey and F-shaped) and vertical concrete barriers based on rollover propensity and occupant injury severity. It was surprisingly pointed out that vertical concrete barriers are actually safer than shaped barriers. In addition to the profile shape of a CSB, the coefficient of friction between vehicle tyres and a CSB also has an important role in the effective vehicle redirection without causing a rollover crash [13]. However, its influence has not yet been thoroughly examined. Most of the papers do not even mention the used value in their simulation studies [11], [14] and [15], or they simply use constant values [16] to [19]. The publicly available experimental data obtained from full-scale crash testing focusing on a vehicle rollover on a CSB is very limited in quantity and quality and mainly consists of video recordings of experiments without any documented parameter values.

In Europe, CSBs are produced and tested according to EN 1317-2 [20] and EN 1317-5 [21], while the concrete mixture is specified by EN 206-1 and EN 13369. However, the above-mentioned standards do not specify the surface roughness or acceptable value of the friction coefficient between the concrete barrier surface and the vehicle tyre. One possible means of reducing the friction coefficient is by using low-friction coatings for concrete [22] to [24]. Although these low-friction coatings are becoming popular, their wider application is limited due to the chemical and impact non-resistance, environmental impact, and their price.

Preliminary data analyses was performed for rollover traffic accidents, which occurred in Ljubljana's ring road between January 1st, 2000 and December 31st, 2015. The data implied a 3 times higher number of vehicle rollovers per kilometre for the northern part of the ring road where median CSBs were installed as compared to the rest of the ring road where steel safety barriers were installed. Although the types of rollover causation in the database were not categorized well enough to allow exclusion of other factors such as road slopes on the sides of the northern part of the ring road, differences in the speed limit, etc., we believe that a significant share of the recorded rollover accidents was caused by CSBs.

The over-involvement of larger vehicles in a rollover, such as SUVs, pickups, and minivan vehicles in fatal crashes, has been well documented in the U.S. in the past studies [9] and [25]. The share of these vehicles in day-to-day traffic in Europe was negligible until recently. However, the vehicle market share presented in Fig. 1 clearly shows that this group of vehicles recorded a nearly 550 % growth in 2015 as compared to 2001 [25]. Their percentage in traffic accidents is expected to increase, also increasing the percentage of rollover accidents. It is thus important to take measures that will prevent the increase in the number of fatalities [26].

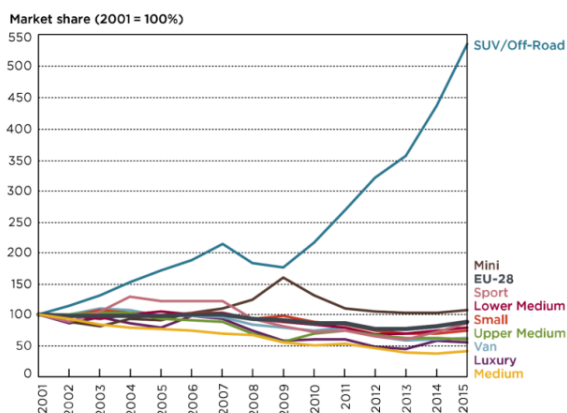


Fig. 1. Vehicle market share according to ICCT [25]

The finite element (FE) method has consistently proved to be a very suitable tool for numerical simulation of a wide range of real-life processes. It simplifies and reduces the cost of examination and product development by allowing precise description of the materials behaviour and the detailed geometry to be incorporated in simulating the reality of the physical process. This study examines the influence of the coefficient of friction between vehicle tyres and the surface of a CSB on the vehicle response after the vehicle-CSB crash scenario. For that purpose, three different finite element vehicle models of Chevrolet C 1500, Suzuki Swift, and Chevrolet Silverado 1500 were used in a numerical crash scenario simulating an impact test with initial conditions taken from the TB11 test case, according to EN 1317-5 [21]. The simulations were performed using the actual measured values of the coefficient of friction between a rubber material and new and aged CSB blocks in dry and wet conditions.

1 METHODS

1.1 Numerical FE Vehicle Models

All three vehicles (Fig. 3) used in the numerical examination of this study are publicly available and were successfully validated by the National Crash Analyses Center (NCAC) [27]. For a more detailed description of the FE vehicle models, an interested reader is referred to the validation reports given in references [28] to [32] for Chevrolet C-1500, [29] for Suzuki Swift and [30] for the Chevrolet Silverado 1500. After the introduction of the FE vehicle models, they were successfully used in different crash analysis studies. Yin [11] used the Silverado 1500 model to optimise the MASH TL-3 concrete barrier, and Kunc et al. [33] and [34] used the Suzuki Swift model to compare different protective structures in tunnel emergency-stop-area-walls [33] to [36]. FE vehicle models are also used in a variety of different applications and purposes [14], [36] to [42]. The FE vehicle models used in this study have only limited capabilities in terms of recreating realistic strain-

stress response of the wheel suspension elements. The fracture prediction of particular parts due to this is thus not taken into account. Even if the detachment of the suspension components does occur, the forces causing it can still cause a rollover before they reach the magnitudes causing the links between suspension components to fail. It is thus assumed that this has little influence on the simulation results as far as a vehicle rollover is concerned.

In all the numerical simulations in this study, the vehicles were initially placed at an impact angle of 20° (Fig. 2) in front of the CSB, hitting it with an initial velocity of 100 km/h. These initial parameters correspond with the TB11 test requirements as described in EN 1317-2 [20]. The friction coefficients between the body pairs involved in contacts used in the simulations are presented in Table 1. The values used are those that, according to measurements (section 2.1), can be realistically expected on manufactured CSBs (from 1.0 down to 0.6) and those that are significantly lower but can be achieved and sustained by special treatment [23] and [24] of the surface (0.6 down to 0.4). The coefficients of friction lower than

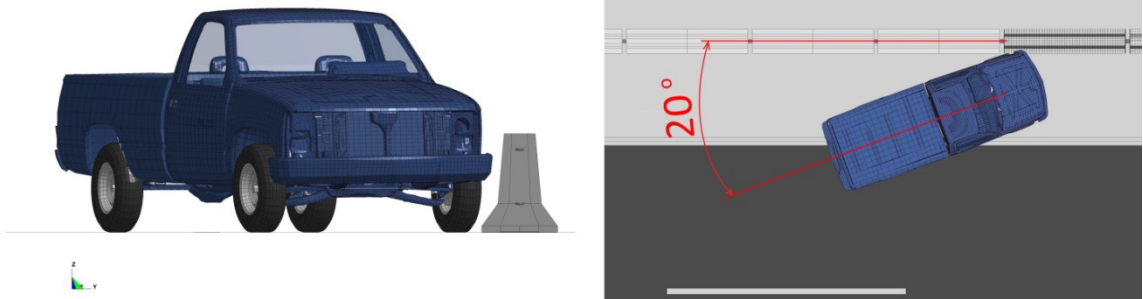


Fig. 2. Initial placement of FE vehicle models before impact (Chevrolet C 1500)

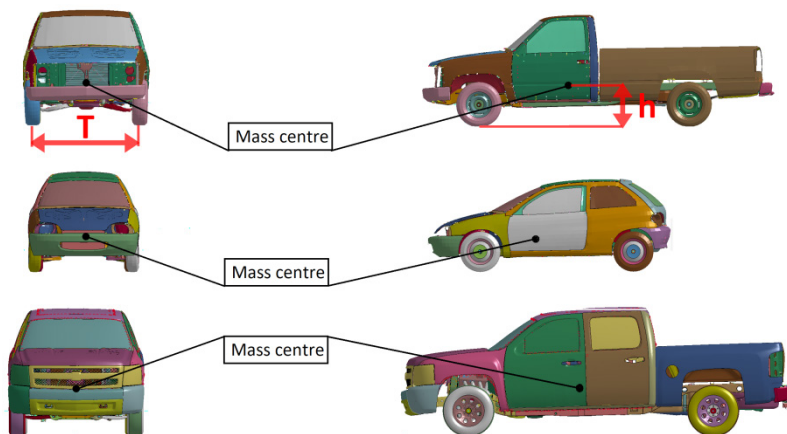


Fig. 3. FE vehicle models

0.4 are unlikely to be encountered on installed CSBs and were thus not included in the research.

Table 1. Summary of the coefficients of friction used in the numerical models

Contact	Friction coefficient	
	static μ	dynamic μD
Vehicle tyres – CSB	0.4	0.3
	0.6	0.5
	0.8	0.7
	1.0	0.9
Vehicle tyres – road surface	0.8	0.7
Vehicle body – CSB	0.3	0.2
Vehicle body – road surface	0.3	0.2

Mass and geometry characteristics of the FE models are summarised in Table 2. The static stability factor (SSF) and static rollover angle α given in Table 2 are calculated using Eq. (1):

$$SSF = \tan \alpha = \frac{T}{2h}, \quad (1)$$

where T is the vehicle track width and h is the height of the vehicle centre of mass as per Fig. 3. As can be seen from Table 2, the values of SSF vary between 1.207 for Chevrolet Silverado and 1.305 for Suzuki Swift.

Table 2. Summary of the coefficients of friction used in the numerical models

Vehicle	Characteristic				
	Mass [kg]	Track width (T) [m]	Centre of mass height (h) [m]	Static stability factor (SSF) [-]	Static rollover angle (α) [°]
Chevrolet C 1500	2013	1.65	0.664	1.242	51.16
Suzuki Swift	894	1.33	0.510	1.305	52.53
Chevrolet Silverado 1500	2622	1.76	0.731	1.207	50.35

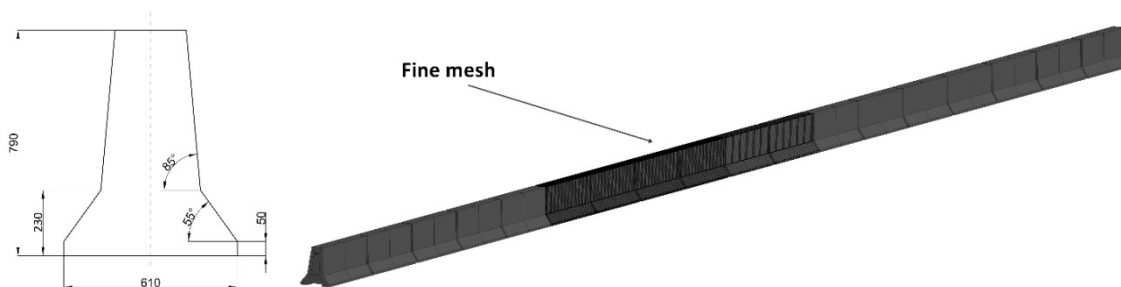


Fig. 4. FE vehicle models

1.2 Median Barrier Anchored

For the purpose of this study, the FE model of the F-shape CSB profile according to EN 1317-5 [21] also available by NCAC [27] was used. A straight barrier section of 55 m was built using 18 blocks (Fig. 4) joined together by pinning the embedded loops from two adjacent blocks.

A typical mass of a 3 m long F-shape profile shown in Fig. 4 is 2000 kg. Although this barrier FE model allows dynamic deflection during vehicle impact, for the purpose of this study it was fixed to the ground. The finite element mesh size of the blocks that are in contact with the vehicle was reduced to 15 mm on the side of the element.

2 EXPERIMENTAL

2.1 Assessment of Actual Coefficients of Friction between Tyre and Concrete Barrier

The processes taking place during the phase of the impact between a rubber vehicle tyre and the surface of a concrete barrier involve several relevant physical phenomena [43] and [44]. The authors of [45] classify these phenomena into three classes regarding the mechanism of dissipation of energy: deformation of the bulk of the rubber due to the substrate asperities, very large viscoelastic deformations close to the opening crack tips that may occur resulting in locally very large energy dissipation, and the energy dissipation from shearing a thin contamination film on the rubber surface and/or on the substrate surface. If such a film is not present, direct bonding between the rubber molecules and the substrate, followed by viscoelastic deformation and bond breaking, also contributes to energy dissipation and sliding friction. The authors of the same paper further present the experimental data which show that the combined

coefficient of friction due to the described phenomena increases with the relative velocity of the contact surfaces, reaching values close to $\mu = 1$ at velocities in the 10^0 m/s to 10^1 m/s range.

To assess the sliding friction coefficient on real concrete barriers, a set of sample tests were performed using a device measuring the pulling force F_t versus the device weight G during sliding from still-stand (Fig. 5). Since all barrier faces of a specific CSB have similar surface quality, the measurements were performed on the top face of the barriers, assuming that the results apply to the entire CSB surface.

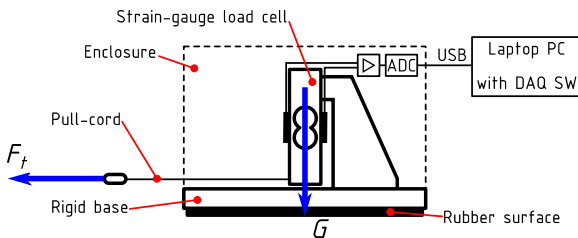


Fig. 5. Schematics of the friction measuring device

The tests were conducted on several concrete barrier blocks with two different types of surface, each in dry and wet conditions. The first type of surface was the rough concrete surface of an aged block (Fig. 6a), while the second type of surface was the smooth surface of a new out-of-mould block (Fig. 6b). The

sliding velocities during the tests were in the 10^{-1} m/s range.

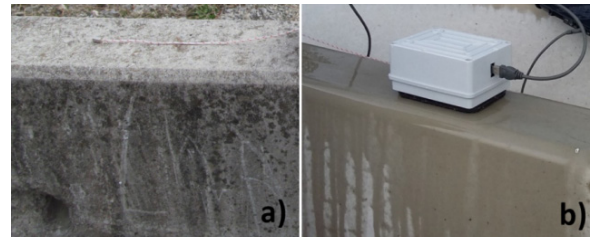


Fig. 6. Measured concrete barrier surfaces: a) rough surface of an aged block in dry condition, b) smooth surface of a new block in wet condition

3 RESULTS

3.1 Pickup Chevrolet C 1500

Fig. 7 visually shows the simulation results obtained using different coefficients of friction between the vehicle tyres and the CSB. As the coefficient of friction increases, the tyre-concrete grip also increases.

Consequently, the vehicle front-end is raised higher along the side of the CSB (Fig. 7). Additionally, the tyre-CSB coefficient of friction is also important in the second stage of the vehicle-CSB contact at which the rear tyre comes into contact with the CSB (Fig.

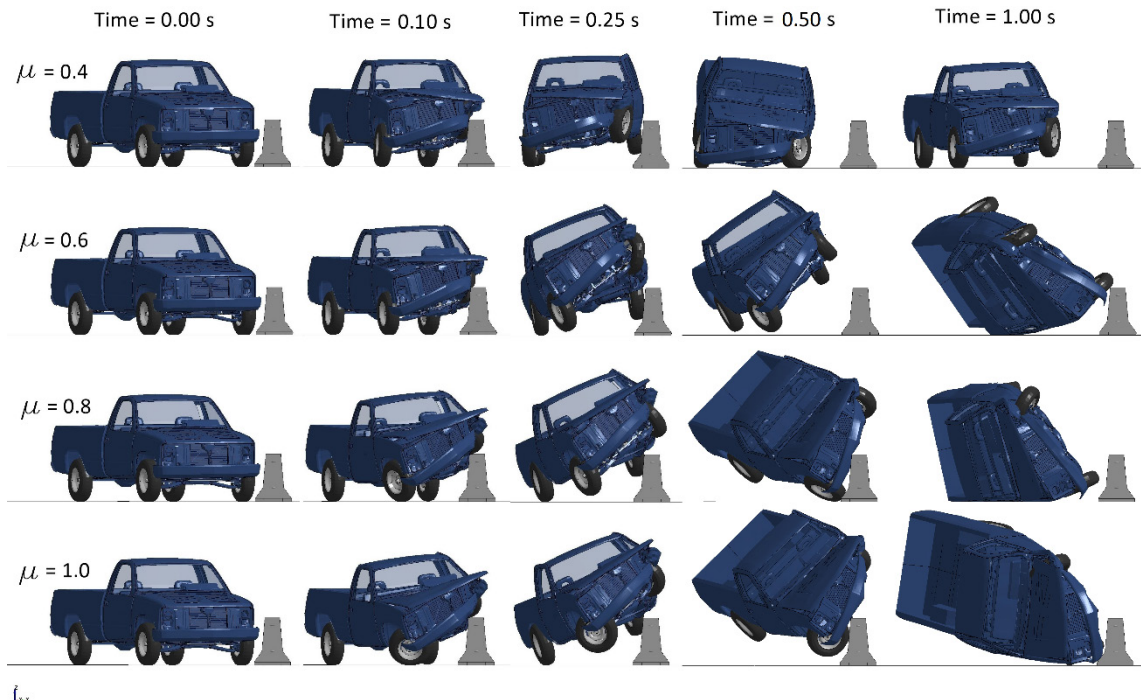


Fig. 7. Pickup Chevrolet C 1500 – CSB contact. Front view

7, time 0.25 s). Depending on the friction coefficient value, the contact could induce or prevent a vehicle rollover. The simulation results show that in the case of low tyre-CSB coefficient of friction ($\mu = 0.4$), the Chevrolet C 1500 is successfully redirected into its driving lane without a rollover, while in all other cases a vehicle rollover occurs. Fig. 8 shows the top view of the simulation results of the vehicle CSB impact at different simulation time frames and different coefficient of friction values.

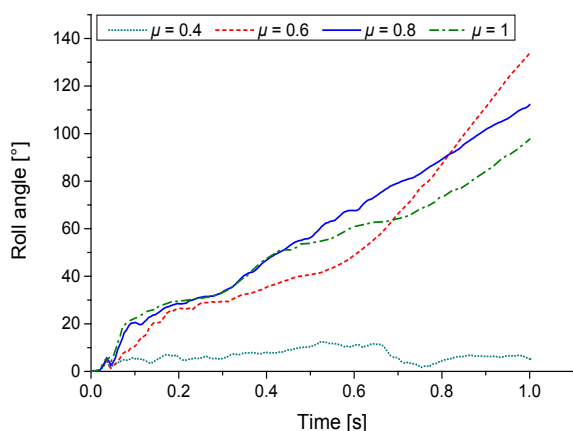


Fig. 8. Roll angle results comparison – Pickup Chevrolet C 1500

The roll angles presented in Fig. 8 were extracted selecting two nodes of the vehicle initially placed at the vertical passing through the vehicle mass centre. From this figure it is also obvious that a vehicle rollover occurs in all cases except in the one with the lowest value of the friction coefficient ($\mu = 0.4$). The roll angles for $\mu = 0.6$, $\mu = 0.8$ and $\mu = 1.0$ greatly exceed the static rollover angle given in Table 2.

3.2 Suzuki Swift

Fig. 9 visually presents the simulation results obtained using different coefficients of friction between the vehicle tyres and the CSB. In this case, no visible vehicle lifting can be noticed.

Fig. 10 presents the roll angles for all cases of the friction coefficient. Although higher roll angle values can be noticed corresponding to higher coefficients of friction, in all the cases the Suzuki Swift vehicle is successfully redirected into its lane without a rollover. The maximal values of the roll angles are significantly below the static roll angle value for the Suzuki Swift vehicle presented in Table 2.

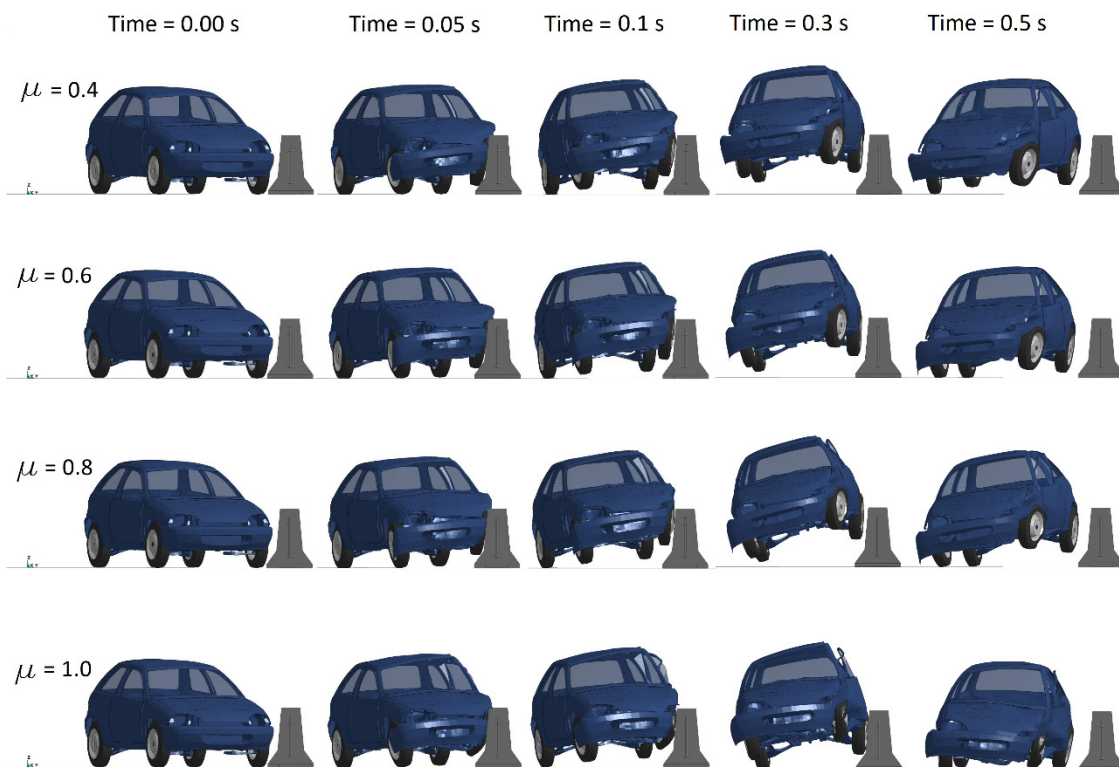


Fig. 9. Suzuki Swift – CSB contact. Front view

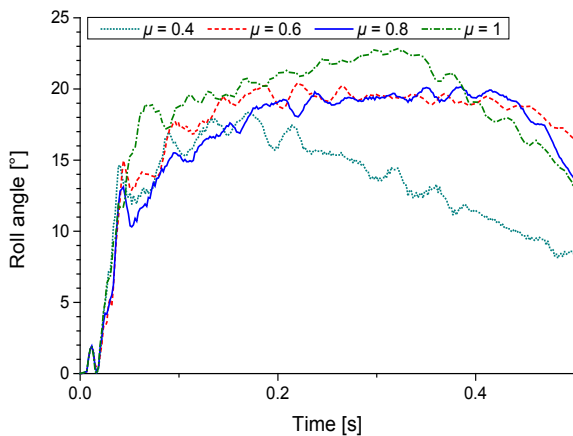


Fig. 10. Roll angle results comparison – Suzuki Swift

3.3 Pickup Chevrolet Silverado 1500

Fig. 11 shows the simulation results obtained using different coefficients of friction between the vehicle tyres and the CSB. As can be seen in Fig. 11, at time = 0.15 s the tyre-concrete grip increases for higher values of the coefficient of friction, and consequently the vehicle's front is raised higher. Similarly to the Pickup Chevrolet C 1500 vehicle, the tyre-CSB coefficient of friction is also important in the second stage of the vehicle-CSB contact at which the rear tyre comes into contact with the CSB. Depending on the friction coefficient value, it could

contribute to the vehicle rollover. In order to reduce the calculation time, different simulation termination times were defined for this model ensuring that the vehicle redirection or rollover was completely covered. Unlike the C 1500 model, the Silverado 1500 vehicle was successfully redirected into its lane for the lower values of the tyre-CSB coefficient of friction ($\mu = 0.4$ and $\mu = 0.6$). At $\mu = 0.8$, the vehicle rotated mainly around its yaw axis without rolling over (Fig. 11, Time = 1.20 s). At $\mu = 1.0$, a vehicle rollover occurs (Fig. 11, Time = 1.40 s).

Fig. 12 presents the roll angles for all cases of the coefficient of friction for the Chevrolet Silverado vehicle. It can be noticed that the roll angles in all cases are well below the static rollover angle presented in Table 2, except in the case of $\mu = 1.0$ at which the roll angle increases significantly over the value of the static rollover angle causing the vehicle to roll over.

3.4 Coefficients of Friction between Tyre and Concrete Barriers

The results of the measurements are summarized in Fig. 13. The test measurements on the smooth surface of the new out-of-the-mould block show that mean values of the coefficient of the sliding friction on its surface range from 0.69 in dry conditions to 0.70 in wet conditions. The average maximum values for the coefficient of the static friction on the surface of this

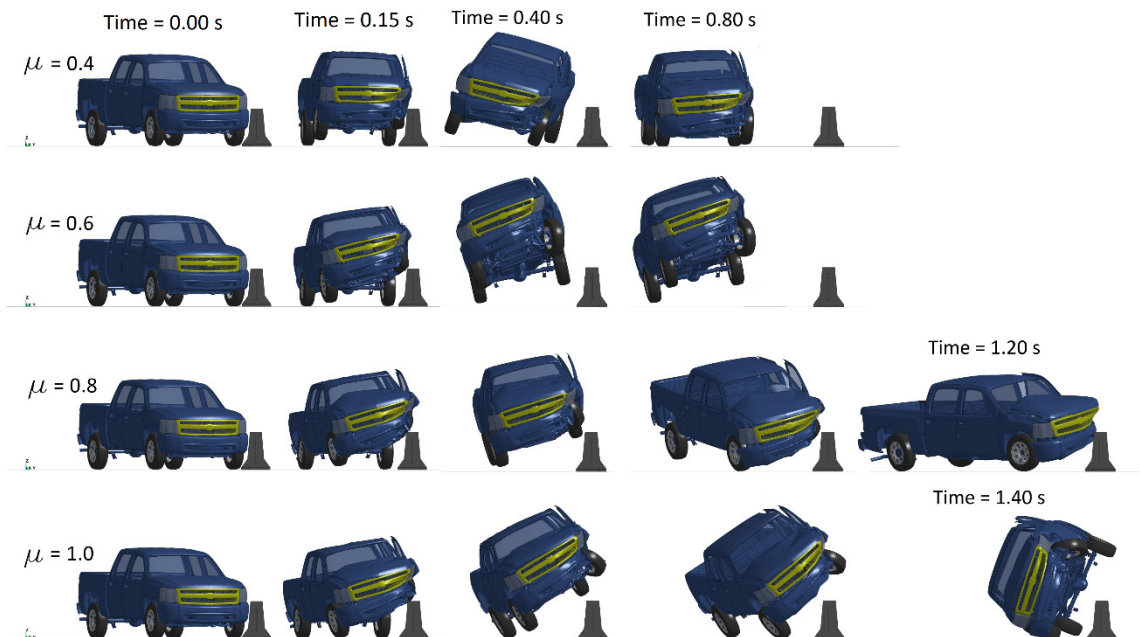


Fig. 11. Pickup Chevrolet Silverado 1500 – CSB contact. Front view

block range from 0.75 in wet conditions to 0.76 in dry conditions. The test measurements on the rough surface of the aged block show that the mean values of coefficient of the sliding friction on its surface range from 0.75 in wet conditions to 0.80 in dry conditions. The average maximum values for the coefficient of the static friction on the surface of this block range from 0.89 in wet conditions to 0.95 in dry conditions.

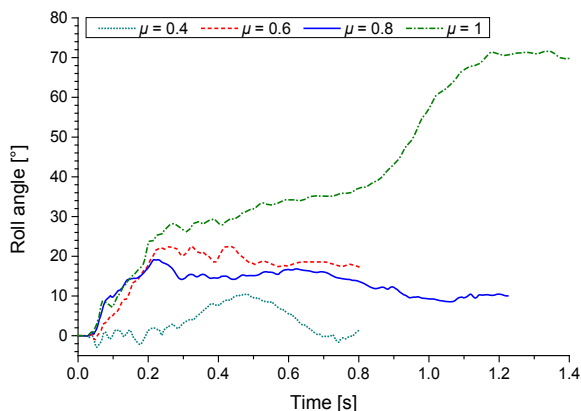


Fig. 12. Roll angle results comparison – Pickup Chevrolet Silverado 1500

The friction coefficients have been measured on installed new and old concrete safety barrier blocks. The new and the old blocks have been exposed to dust and debris. The particles thereof were found to reduce the friction on the dry blocks to some extent, especially on the new blocks. These particles were washed away when a layer of water was applied to the block surface, causing the friction to increase slightly. By doing so, we intended to simulate the natural way of changing the conditions on the block surface, where the dust and debris deposit is periodically washed away with water by rain or by cleaning.

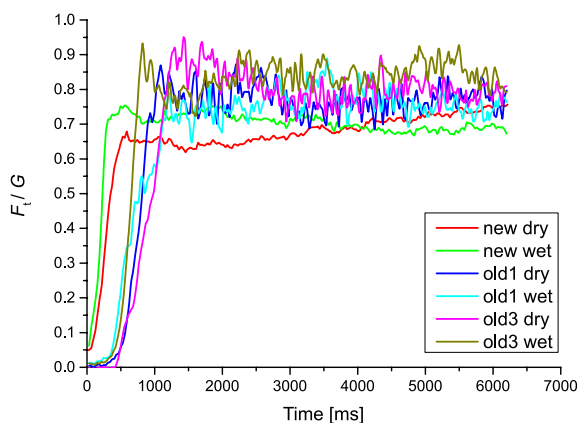


Fig. 13. Measurement results on test surfaces

The results are summarized in Table 3. The coefficients of friction have been measured with low contact surface relative velocities, meaning that the energy dissipation due to opening crack tips and due to direct bonding between the rubber molecules and the substrate [45] did not occur at all. Considering this, the expected real values of friction coefficients on the contact between the barrier and the vehicle tyre on impact are higher than the measured values and can easily exceed the values found to cause a vehicle rollover.

Table 3. Measured friction coefficient values

CSB surface description	avg avg μ	avg max μ
smooth surface, new block, dry	0.69	0.76
smooth surface, new block, wet	0.70	0.75
rough surface, aged block 1, dry	0.77	0.87
rough surface, aged block 1, wet	0.76	0.89
rough surface, aged block 2, dry	0.80	0.95
rough surface, aged block 2, wet	0.84	0.93

4 CONCLUSIONS

The influence of the coefficient of friction between vehicle tyres and CSB on a vehicle rollover was studied in detail. Additionally, the rubber-CSB coefficient of friction was experimentally determined for aged and new CSB blocks under wet and dry conditions. The results showed that the values of the coefficient of friction can be high enough to cause a vehicle rollover. This is especially true for large vehicles with a higher center of mass, such as pickups, SUVs and minivans, which are becoming increasingly more frequent on the European roads. Apart from the geometry optimization of the CSB profile, it is very important to reduce the coefficient of friction between the surface of a CSB and the vehicle tyre rubber compound in order to reduce the rollover risk in case of a vehicle-CSB contact. To achieve this, different strategies such as reducing the friction coefficient by determining the surface roughness of CSBs or development and application of low friction coatings should be applied in order to reduce the rollover risk for vehicles from this group.

5 ACKNOWLEDGEMENT

The research presented in this article has been partly funded by the Slovenian Research Agency as part of the “Modelling in technics and medicine” (code P2-0109 (C)) research programme.

8 REFERENCES

- [1] WHO (2015). *Global Status Report on Road Safety 2015*. World Health Organization, Geneva.
- [2] European Commission - Fact Sheet (2017). *2016 Road Safety Statistics: What is behind the Figures*, European Commission La Valette.
- [3] Gabler, H.C., Gabauer, D.J. (2007). Opportunities for reduction of fatalities in vehicle-guardrail collisions. *Annual Proceedings of the Association for the Advancement of Automotive Medicine*, p. 31.
- [4] EUPAVE (2012). *Concrete Safety Barriers: A Safe and Sustainable Choice*. European Concrete Paving Association (EUPAVE), Brussels.
- [5] Artimovich, N. (2010). *Concrete barriers*. FHWA Office of Safety, Roadway Departure Team, Washington.
- [6] DARS (2017). Družba za avtoceste v Republiki Sloveniji, from <https://www.dars.si/>, accessed on 2017-02-12.
- [7] Grzebieta, R.H., Zou, R., Jiang, T., Carey, A. (2005). Roadside hazard and barrier crashworthiness issues confronting vehicle and barrier manufactures and government regulators. *Proceedings of the 19th International Technical Conference on the Enhanced Safety of Vehicles*, Washington.
- [8] McDevitt, C.F. (2000). Basics of concrete barriers. *Public Roads*, vol. 63, no. 5, p. 10-14.
- [9] Polivka, K.A., Faller, R.K., Sicking, D.L., Rohde, J.R., Bielenberg, B.W., Reid, J.D., Coon, B.A. (2006). *Performance Evaluation of the Permanent New Jersey Safety Shape Barrier-Update to NCHRP 350 test no. 4-12 (2214NJ-2)*. Midwest Roadside Safety Facility, University of Nebraska-Lincoln, Lincoln.
- [10] Zain, M.F.B.M., Mohammed, H.J. (2015). Concrete road barriers subjected to impact loads: An overview. *Latin American Journal of Solids and Structures*, vol. 12, no. 10, p. 1824-1858, DOI:10.1590/1679-78251783.
- [11] Yin, H., Fang, H., Wang, Q., Wen, G. (2016). Design optimization of a MASH TL-3 concrete barrier using RBF-based metamodels and nonlinear finite element simulations. *Engineering Structures*, vol. 114, p. 122-134, DOI:10.1016/j.engstruct.2016.02.009.
- [12] Albuquerque, F.D.B., Sicking, D.L. (2013). In-service safety performance evaluation of roadside concrete barriers. *Journal of Transportation Safety & Security*, vol. 5, no.2, p. 148-164, DOI:10.1080/19439962.2012.715618.
- [13] Mak, K.K., Sicking, D.L. (1990). *Rollover Caused by Concrete Safety-Shaped Barrier*, Transportation Research Record, no. 1258, p. 71-81.
- [14] Marzougui, D., Zink, M., Zaouk, A., Kan, C.D., Bedewi, N. (2004). Development and validation of a vehicle suspension finite element model for use in crash simulations. *International Journal of Crashworthiness*, vol. 9, no. 6, p. 565-576, DOI:10.1533/ijcr.2004.0311.
- [15] Sheikh, N.M., Bligh, R.P., Menges, W.L. (2009). *Development and Testing of a Concrete Barrier Design for Use in front of Slope or on MSE Wall*. Report 405160-13-1. Texas Transportation Institute, College Station.
- [16] Itoh, Y., Liu, C., Kusama, R. (2007). Dynamic simulation of collisions of heavy high-speed trucks with concrete barriers. *Chaos, Solitons & Fractals*, vol. 34, no. 4, p. 1239-1244, DOI:10.1016/j.chaos.2006.05.059.
- [17] Thiyahuddin, M.I., Thambiratnam, D.P., Gu, Y.T. (2014). Effect of joint mechanism on vehicle redirection capability of water-filled road safety barrier systems. *Accident Analysis & Prevention*, vol. 71, p. 60-71, DOI:10.1016/j.aap.2014.05.010.
- [18] Abraham, N., Ghosh, B., Simms, C., Thomson, R., Amato, G. (2016). Assessment of the impact speed and angle conditions for the EN1317 barrier tests. *International Journal of Crashworthiness*, vol. 21, no. 3, p. 211-221, DOI:10.1080/1358265.2016.1164444.
- [19] Bielenberg, R.W., Faller, R.K., Reid, J.D., Schmidt, J.D., Pajouh, M.A., Emerson, E. (2016). Development of a retrofit, low-deflection temporary concrete barrier system. *Journal of Transportation Safety & Security*, DOI:10.1080/19439962.2017.1420717.
- [20] EN 1317-2 (2010). *Performance Classes, Impact Test Acceptance Criteria and Test Methods for Safety Barriers*. European Committee for Standardization, Brussels.
- [21] EN 1317-5 (2010). *Product Requirements and Evaluation of Conformity for Vehicle Restraint Systems*. European Committee for Standardization, Brussels.
- [22] Kulkarni, S. (2012). *Environmentally Friendly Low Friction Coating for Concrete Barriers*, SBIR & STTR, SBA, Washington.
- [23] NanoSonic Anti-Rollover Concrete Barrier Coating (2014). from <http://www.nanosonic.com/anti-rollover-concrete-barrier-coating/>, accessed on 2017-02-12.
- [24] Kalenborn Abresist Corp. (2014). KALCOAT 595, from <http://www.abresist.com>, accessed on 2017-02-09.
- [25] ICCT (2017). *European Vehicle Market Statistics: Pocketbook 2016/17*. The International Council on Clean Transportation (ICCT), Berlin, p. 118.
- [26] Farmer, C.M., Lund, A.K. (2002). Rollover risk of cars and light trucks after accounting for driver and environmental factors. *Accident Analysis & Prevention*, vol. 34, no. 2, p. 163-173, DOI:10.1016/S0001-4575(01)00010-0.
- [27] NHTSA (2017). *National Highway Traffic Safety Administration*, US Department of Transportation, Washington.
- [28] NCAC (2008). *Finite Element Model of C1500 Pickup Truck*, National Crash Analysis Center, US Department of Transportation, Washington.
- [29] NCAC (2008). *Development & Validation of a Finite Element Model for the 1997 Geo Metro Passenger Sedan*, National Crash Analysis Center, US Department of Transportation, Washington.
- [30] NCAC (2012). *Extended Validation of the Finite Element Model for the 2007 Chevrolet Silverado Pick-Up Truck*, National Crash Analysis Center, US Department of Transportation, Washington.
- [31] Zaouk, A., Bedewi, N.E., Kan, C.-D., Marzougui, D. (1996). Development and evaluation of a C-1500 pickup truck model for roadside hardware impact simulation. *Proceedings of the FHWA Vehicle Crash Analysis Crash Conference*, McLean, p. 1-31.
- [32] Zaouk, A.K., Bedewi, N.E., Kan, C.-D., Marzougui, D. (1996). Validation of a non-linear finite element vehicle model using multiple impact data. *ASME Applied Mechanics Division - Publications - AMD 218*, p. 91-106.

- [33] Kunc, R., Omerović, S., Ambrož, M., Prebil, I. (2014). Comparative study of European tunnel emergency-stop-area-wall protection measures. *Accident Analysis & Prevention*, vol. 63, p. 9-21, DOI:10.1016/j.aap.2013.10.020.
- [34] Kunc, R., Omerović, S., Ambrož, M., Prebil, I. (2016). How to protect the tunnel SOS niche wall in the event of vehicle impact. *Transportation Research Procedia*, vol. 14, p. 1305-1314, DOI:10.1016/j.trpro.2016.05.203.
- [35] Teng, T.-L., Liang, C.-C., Tran, T.-T. (2015). Effect of various W-beam guardrail post spacings and rail heights on safety performance. *Advances in Mechanical Engineering*, vol. 7, no. 11, DOI:10.1177/1687814015615544.
- [36] Sheikh, N.M., Bligh, R.P., Albin, R.B., Olson, D. (2010). Application of precast concrete barrier adjacent to steep roadside slope. *Transportation Research Record: Journal of the Transportation Research Board*, vol. 2195, no. 1, p. 121-129, DOI:10.3141/2195-13.
- [37] Marzougui, D., Kan, C.D., Opiela, K.S. (2013). Crash test & simulation comparisons of a pickup truck & a small car oblique impacts into a concrete barrier. *Proceedings of the 13th International LS-DYNA Users Conference*, Dearborn.
- [38] Hu, B., Li, G.-Q., Sun, J.-Y. (2014). Numerical investigation of K4-rating shallow footing fixed anti-ram bollard system subjected to vehicle impact. *International Journal of Impact Engineering*, vol. 63, p. 72-87, DOI:10.1016/j.ijimpeng.2013.08.006.
- [39] Pawlak, M. (2016). The acceleration severity index in the impact of a vehicle against permanent road equipment support structures. *Mechanics Research Communications*, vol. 77, p. 21-28, DOI:10.1016/j.mechrescom.2016.08.005.
- [40] Sassi, S., Sassi, A., Ghrib, F. (2017). Effect of crushable blockouts on a full-scale guardrail system. *International Journal of Crashworthiness*, vol. 22, no. 1, p. 63-82, DOI:10.1080/13588265.2016.1223525.
- [41] Vesenjaj, M., Ren, Z. (2003). Computer-aided design of a road restraint barrier. *Strojniški vestnik - Journal of Mechanical Engineering*, vol. 49, no. 10, p. 509-519.
- [42] Borovinšek, M., Vesenjaj, M., Ulbin, M., Ren, Z. (2006). Simulating the impact of a truck on a road-safety barrier. *Strojniški vestnik - Journal of Mechanical Engineering*, vol. 52, no. 2, p. 101-111.
- [43] Blackford, J.R., Skouvaklis, G., Purser, M., Koutsos, V. (2012). Friction on ice: Stick and slip. *Faraday Discussions*, vol. 156, p. 243-254, DOI:10.1039/c2fd00128d.
- [44] Persson, B.N.J. (1998). On the theory of rubber friction. *Surface Science*, vol. 401, no. 3, p. 445-454, DOI:10.1016/S0039-6028(98)00051-X.
- [45] Lorenz, B., Persson, B.N.J., Dieluweit, S., Tada, T. (2011). Rubber friction: Comparison of theory with experiment. *The European Physical Journal E*, vol. 34, no. 129, p. 1-11, DOI:10.1140/epje/i2011-11129-1.

Effects of Advanced Manufacturing Technologies on Manufacturing Company Performance

Jasna Prester¹ – Borut Buchmeister² – Iztok Palčič^{2,*}

¹ University of Zagreb, Faculty of Economics and Business, Croatia

² University of Maribor, Faculty of Mechanical Engineering, Slovenia

Literature findings on the effects of advanced manufacturing technology (AMT) on company performance measures is currently inconclusive. There is also a lack of recent research on this issue from a contingency perspective. It is also a fact that the majority of research is conducted in developed countries. This research is based on the contingency theory perspective, and it attempts to add value to the observed literature gaps by exploring two less developed countries Slovenia and Croatia. Using survey data from 138 manufacturing companies from Croatia and Slovenia, we tested the effects of twenty technologies on different performance measures through five ordinary least squares regression analyses. Contingency factors in terms of company size, batch size, product complexity, included as control variables in analyses, proved insignificant for technologies' use and their effect on profits before tax, decrease in the scrap rate, material and staff costs. On the other hand, AMT has impact on material consumption, scrap rate and profits, but not in a positive hypothesised relationship.

Keywords: advanced manufacturing technology, manufacturing company, operations' performance, contingency theory, European manufacturing survey

Highlights

- The impact of advanced manufacturing technologies (AMT) use on manufacturing company performance is studied.
- The research of AMT use and their impact on company performance is based on the contingency theory approach.
- Contingency factors such as batch size, company size and product complexity do not influence staff costs, innovation revenues, scrap rate or profit before tax significantly.
- AMT have impact on material consumption, scrap rate and profits, but not in a positive relationship.

0 INTRODUCTION

Today, many market environments are characterised by the rising costs of raw materials, technological and economic uncertainty and decreasing profit margins. There is a general trend towards an increase in the use of technology in manufacturing plants, due to the belief that this will improve some performance measures (e.g. reductions in costs or human resources, improved quality or flexibility) and profitability [1]. Empirical evidence has shown mixed results of the advanced manufacturing technology (AMT) use on performance, therefore, calling for additional research on this specific field of operations management. Some research showed positive effects, while others demonstrated negative or non-significant effects. For the purpose of our study, we follow Baldwin and Sabourin [2], who defined AMT as “a group of integrated hardware-based and software-based technologies which, if properly implemented, monitored, and evaluated, will lead to improving the efficiency and effectiveness of the firm in manufacturing a product or providing a service”.

The discrepant findings in the literature suggest there is a need to identify contingencies that may govern the AMT–performance relationships [3]. Contextual variables are strategic context, company

size, production processes type, or product complexity [4]. Except for Raymond [5] who shows positive effects of technology use on the performance of SMEs, no other research focused on differences in performance depending on company size. Therefore, our first question is how contextual variables such as company size, production processes type, or product complexity affect performance through the use of AMT.

Moreover, technology evolves on an almost yearly basis. When analysing literature, it is important to consider the year in which the research was conducted. Analysing current research on AMT through the contingency theory, most research was conducted between 1990 and 2001, with later research not even mentioning the year it was conducted. Additionally, the majority of studies explore a single manufacturing technology [6]. Therefore, these facts present a clear gap in literature and a need to show recent results of different AMT use and their impact on manufacturing company performance.

1 LITERATURE REVIEW ON CONTINGENCY THEORY AND AMT IMPACT ON COMPANY PERFORMANCE

The contingency theory explains that the same set of contingencies will not lead to the same result due

*Corr. Author's Address: University of Maribor, Faculty of Mechanical Engineering, Smetanova ulica 17, 2000 Maribor, iztok.palcic@um.si

to different contextual factors [7]. Contextual factors are often situational factors, usually exogenous to the company. These factors can be changed, but this can happen only in the long run and with substantial effort [8]. The mentioned contextual variables are strategic context, company size, production processes type, or product complexity [4]. The contingency theory suggests that performance should increase when there is a fit between a company's use of practices and dimensions of the organisational context in which it takes place [5] – a better fit yields better performance [9]. Performance variables are the dependent measures, and they measure the fit between the contextual variables and contingency variables for a situation under consideration [8]. As far as performance variables are concerned, there is a plethora of variables used in literature, ranging from growth to operations performance measures, so it is not easy to compare different research studies and their findings. According to Sousa and Voss [8], operations performance measures are not used enough and survey research is appropriate for identifying contingency effects.

A comprehensive review of literature shows there are only few research studies dealing with AMT through contingency theory, among which Boyer et al. [10] appears to be the most influential one. Careful inspection of the researched AMT in Boyer et al. [10] shows that those were the most used technologies at the time of the publication of the paper, and the majority of authors later referred to them in their research. Kotha and Swamidass [11] show that the main reason for employing AMT is the potential to improve business performance, and not to reduce costs. They define AMT as all technologies that use computers or microprocessors. Technology is divided into four groups: Product design technology, process technology, logistics and planning technologies and information exchange technologies. They found that the level of AMT implementation depends on the size of the company, possibly because larger companies have more resources. Swink and Nair [3] provide a thorough literature review, based on which they propose 23 AMTs divided into process AMT and planning AMT, but they, in fact, also researched the technologies shown in Boyer et al. [10].

According to Goyal and Grover [12], manufacturing evolves continuously and the adoption of AMT is usually due to the intention to improve some of the competitive factors, such as delivery, cost, quality, or flexibility, in line with Kotha and Swamidass [11]. Percival [13] finds that, besides the widely stated benefits of improving own

performance, AMT can also represent an entry barrier for competition. Her main theoretical findings are that AMT reduces the need for unskilled workers, but it augments the demand for skilled workers, which eventually may not reduce labour costs. On the other hand, due to automation and eliminating human error, there is a decrease in scrap rate [14].

AMT is more present in larger companies than in the small ones, and it is also more present in more innovative industries than in low tech industries, proving that size and industry are contextual factors. Except for Raymond [5], who shows positive effects of technology use on the SMEs' performance, no other research focused on differences in performance depending on company size. We therefore hypothesise that size has impact on performance through AMT use.

Empirical studies have reported non-significant or even negative direct associations of AMT adoption to performance. The discrepant findings in the literature suggest the need to identify contingencies that may govern the AMT–performance relationships. Prior examinations of the AMT–performance moderating factors addressed mainly infrastructural and demographic variables such as worker empowerment, quality programmes, and production process type [3].

All research studies investigated some sort of infrastructural element, which was proven to be a significant predictor of AMT benefits (e.g., quality management practices, workers' training and empowerment). Therefore, there is a clear gap in research as to how technology per se influences materials' consumption, staff costs, scrap rate, innovation and profitability. In this research, we use the [15] notion that the operating characteristics of a company are determined by its production structure, product type and product complexity. Therefore, it is important to look at product type (simple to complex) and production process type, which, in fact, distinguishes between make to order (MTO) versus make to stock (MTS). Also, company size is considered in terms of the number of employees.

Schroeder and Flynn [16] warn that it is better to adopt certain technologies for specific objectives. There is also a warning that the same technology will not lead to the same results in two different plants [17] to [24]. Thus, there is a need to observe the effects of each technology separately. In this paper, the impact of technology on quality, material consumption, labour expenses (cost) and innovation are examined, as those are important manufacturing concerns today. Material consumption is measured through cost of inputs (purchased parts, material, raw materials) as a

percent of annual turnover. Staff costs are measured through payroll costs as a percent of annual turnover. We address quality through the scrap rate adapted from Nair et al. [25]. Innovation is measured through revenues from new products that were introduced by the company in the last 3 years. Likewise, we also studied how technology affects the bottom line, that is, returns on sales before tax.

Based on literature research of each technology and its characteristics, we hypothesise relationships for each manufacturing technology on the dependent variables (Table 1).

If a positive relationship is assumed, a plus sign respectively denotes the hypothesised relationship (a minus sign denotes a negative relationship). As can be seen in Table 1, most technologies are intended to reduce costs of production. Robots are supposed to lower staff costs, but also to increase precision and reduce errors [26]. Technologies for safe human-machine cooperation and supply chain management are intended to reduce errors and, therefore, reduce operating costs. Technologies that are supposed to increase innovation are product lifecycle management system, because monitoring of equipment use enables its improvement. Moreover, energy and resource

efficiency technologies and additive manufacturing technologies are aimed at using resources efficiently. It is hypothesised that they would reduce manufacturing costs, but not necessarily material and staff costs. Therefore, this group of technologies will influence profits directly. Technologies under digital group factory are hypothesised to reduce error of handling, timely information so as to reduce costs of mistakes, not necessarily reducing material or staff costs, therefore we hypothesise that they will affect return on sales before tax positively.

More specifically, our research seeks to answer the following research questions:

- How do AMT affect certain performance measures?
- How do contingency factors measured through control variables affect certain performance measure?

2 RESEARCH METHODOLOGY

The research data was collected using the European manufacturing survey (EMS), coordinated by the Fraunhofer Institute for Systems and Innovation Research – ISI, the largest European survey of

Table 1. Hypothesised relationships of technologies on cost, quality and innovation

Technology	Share of use [%]	Material consumption	Staff cost	Quality	Innov. revenue	Profit
Automation and robotics	Industrial robots for manufacturing processes	28.3	–	–	+	+
	Industrial robots for handling process	22.5	–	–		+
	Control system for shut down	13.8	–			+
Energy and resource efficiency	Control-automation systems for energy efficient production	14.5				+
	Technologies for recuperation of energy	21.0				+
	Manufacturing technologies for micromechanical components	3.6			+	+
Processing techniques for new materials	Nano-technological production processes	6.5			+	+
	Processing techniques for composite materials	4.3			+	+
	Biotechnology / genetic engineering methods	1.4			+	+
	Processing techniques for alloy construction materials	5.8			+	+
Additive manufacturing technologies	Additive manufacturing technologies for prototyping	13.0	-			+
	Additive manufacturing technologies for mass production	15.9	-			+
Digital factory	Software for production planning and scheduling	52.2		-		+
	Near real-time production control system	31.2				+
	Digital exchange of product/process data	28.3				+
	Systems for automation and management of internal logistics	13.0				+
	Devices for programming and handling of machines	13.0				+
	Product lifecycle management (PLM) systems	12.3			+	+
	Technologies for safe human-machine interaction	8.7				+
	Digital visualization	11.6				+

manufacturing activities. The survey is conducted among manufacturing companies (NACE Rev.2 codes from 10 to 32) having at least 20 employees. The survey is conducted on a three-year basis and new concepts are added to the questionnaire, while obsolete concepts are excluded. The 2015 survey round had extensive changes, especially in the technology part. A basic questionnaire is developed in English and then translated, including backwards translation. Second, pre-tests are conducted in each participating country. Third, identical data harmonization processes are applied.

Questionnaires were sent to Chief Executive officers of manufacturing companies, and they were completed by several persons, usually by operations management and accounting staff. After two weeks, companies which did not respond were called by telephone and asked to fill in the questionnaire, or they were asked to specify the reasons why they could not respond. In Croatia, 106 responses were collected, representing an 8 % response rate. A non-response base was tested with the χ^2 test between early and late responders and there was no significant difference between responders. The same procedure was applied in Slovenia, obtaining a sample of 91 manufacturing companies with a 13 % return rate.

The representativeness of the sample was checked by size and industry, and it shows generalizability for Croatian and Slovenian manufacturing. However, we included in the analysis only sectors that are equally present in both countries, resulting in a decrease of the sample from 197 to 138 companies.

For each researched technology presented in Table 1 we asked about its use (yes/no) – use frequency is presented in the second column. The analysis was performed using five independent ordinary least squares regression analyses in order to find the impact of each technology on a specific parameter, that is, on a dependent variable. The dependent variables are profits, revenues from new products, scrap rate and costs (material and staff). Therefore, five independent regressions are made. The independent variables were technologies, that is, a dichotomous value (0 – not using it, 1 – using it).

Company size, product complexity, and production process type were used as control variables. It is believed that larger companies have more resources to invest into technology, so size should be considered as an important factor. Moreover, more complex products might require more AMT, therefore complexity is also used as a control variable. Production process type was included,

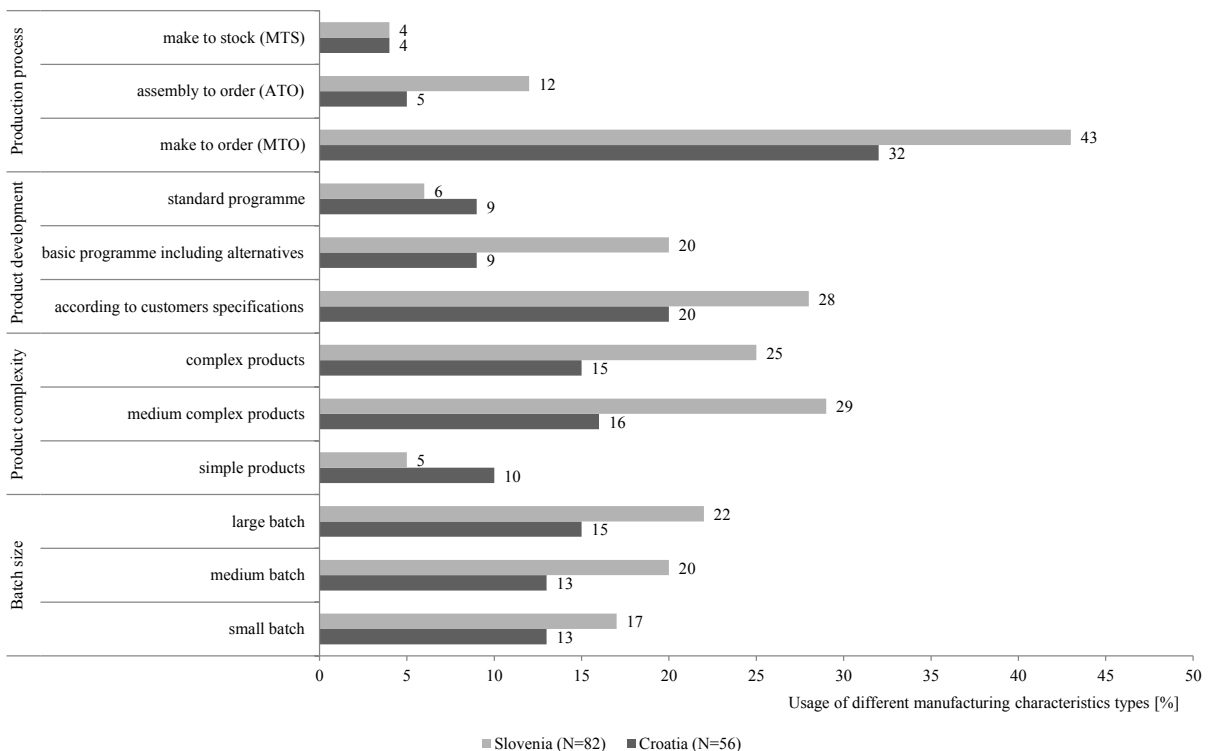


Fig. 1. Manufacturing characteristics of the Croatian and Slovenian sample

since it is connected with business strategy. MTS is generally associated with low cost strategy, while MTO with differentiation. Those control variables are also contextual factors from the contingency theory perspective.

3 RESULTS AND DISCUSSION

Our sample includes 28 % small companies (less than 50 employees), 53 % medium-sized companies (between 51 and 250 employees) and 20 % large companies (more than 50 employees). According to the industry structure, 39 % of companies are from NACE 25 (metal products except machinery), 20 % from NACE 28 (machinery), 12 % from NACE 22 (rubber and plastics), 9 % from NACE 27 (electronic equipment), 8 % from NACE 23 (Non-metallic), etc.

It is known that there might be different types of manufacturing characteristics inside each manufacturing sector. Fig. 1 therefore displays the four groups of the basic characteristics of Croatian and Slovenian manufacturing companies: Product development (3 properties), production process type (3), batch size (3) and product complexity (3), observed by the company size.

Measurement results are presented in Table 2. The Table 2 shows the results from five independent regression analyses, standardised regression coefficients, model characteristics (R, Adjusted R², F and Sig.) as well as the hypothesised relationships presented in Table 1. Covariance and correlations between variables was also checked, as it is a standard output of the SPSS software package. Those data are all available on demand because of a lack of space in the paper. The data show that inter-correlations are not high. Multicollinearity diagnosis shows the highest condition index of 13.207 (lower than 30) and all the variance proportions are less than 0.5 in accordance with the prescriptions by Meyers et al. [27]. Variance inflation factors (VIF) are all less than 2.

Looking into the first regression, where the dependent variable was material consumption, one can observe that contextual factors do not play a significant role. Industrial robots for manufacturing do decrease material consumption, although not significantly. On the contrary, it was hypothesised that industrial robots for handling would decrease material consumption, but the sign is positive, although not significant, meaning that robots for handling use more material resources usually for packing. It was hypothesised that control system for shut down would decrease material consumption by automatically

shutting down the machine, but this was also proved non-significant.

Additive manufacturing technologies for mass production augments material costs, which is contrary to our hypothesis, because this technology was designed to build products layer by layer instead of the need to drill, scrape and carve from material, and should therefore contribute to material savings. However, current research on 3D systems shows that 3D manufacturing is still slow and expensive, and time will pass before it gets used for mass production. The augmentation of material use might be resulting from companies experimenting with the technology, not necessarily using it for mass production. Eleven out of twenty AMT reduce material consumption, although not significantly. Six AMT have almost no impact on material consumption but are also not significant. This first regression (Table 2) shows this model is not overall significant and, therefore, cannot be generalised. It can only be concluded that some of AMT do in fact reduce material consumption, but there is a significant raise in material consumption using 3D technologies for production, even though this technology is still not widespread, rather more used for building prototypes.

Percival [13] concluded that the need for unskilled workers may have diminished with the use of robots, but the need for skilled personnel has risen, so in effect there would be no change in staff costs. Our analysis indeed shows that contribution of AMT on staff cost is indeed non-significant. Robots do, in fact, decrease staff costs, but the reduction is not significant. Thirteen AMT out of twenty reduce staff cost, but the significant reduction is in using software for production planning and scheduling which was done manually before and is now replaced by software. A near real-time production control system shows a significant increase in staff costs, and that is in line with Percival [13] for the need of skilled personnel even though much of the manufacturing is computerised.

The third regression (innovation revenues) is significant, explaining 42.8 % of innovation revenues. Here one contingency (country) plays an important role, showing that Slovenian companies obtain significantly higher revenues from innovation. Especially profitable technology for innovation is processing techniques for composite materials, which shows a significant positive effect. On the contrary, devices for programming and handling of machines in innovation show a negative impact, probably due to a lot of work for each new product. Half of AMT do affect innovation revenues positively, but

Table 2. Results of the regression analyses (in parenthesis are hypothesised relationships)

Variables	Material consumption		staff costs		innovation revenue		scrap rate		profit	
	Stand. Beta	Sig.	Standard. Beta	Sig.	Standard. Beta	Sig.	Standard. Beta	Sig.	Standard. Beta	Sig.
Country (Slovenia, Croatia)	0.021	0.857	0.031	0.769	-0.482	0	0.036	0.673	0.096	0.391
Batch size	-0.122	0.302	-0.089	0.408	0.037	0.736	0.053	0.543	-0.097	0.407
Complexity	0.05	0.651	0.048	0.637	0.189	0.071	0.097	0.252	0.1	0.356
Product development	0.021	0.865	-0.122	0.277	-0.144	0.188	-0.016	0.86	0.037	0.753
Production process type	-0.005	0.964	0.01	0.927	-0.131	0.252	-0.131	0.144	-0.112	0.347
Number of employees	-0.016	0.893	-0.006	0.955	-0.012	0.921	-0.07	0.448	0.138	0.246
Industrial robots for manufacturing processes	-0.119 (-)	0.322	-0.033 (-)	0.76	0.026	0.815	-0.006 (+)	0.944	0.105 (+)	0.37
Industrial robots for handling process	0.039 (-)	0.766	-0.027 (-)	0.82	0.092	0.453	0.017	0.861	0.028 (+)	0.825
Control system for shut down	0.084 (-)	0.455	-0.06	0.56	-0.015	0.885	0.305	0.001	0 (+)	0.997
Control-automation systems for energy efficient production	0.07	0.606	-0.021	0.862	0.041	0.751	0.242	0.02	-0.105 (+)	0.431
Technologies for recuperation of energy	0.02	0.883	0.276	0.029	0.069	0.574	-0.062	0.544	-0.15 (+)	0.252
Manufacturing technologies for micromechanical components	-0.187	0.129	0.005	0.967	0.019 (+)	0.865	0.09	0.296	-0.193 (+)	0.103
Nano-technological production processes	0.014	0.908	-0.13	0.236	-0.167 (+)	0.114	-0.009	0.923	-0.041 (+)	0.734
Processing techniques for composite materials	-0.19	0.159	0.11	0.372	0.275 (+)	0.022	-0.604	0	0.118 (+)	0.416
Biotechnology / genetic engineering methods	0.175	0.165	-0.144	0.21	-0.079 (+)	0.504	-0.255	0.008	-0.269 (+)	0.037
Processing techniques for alloy construction materials	-0.06	0.602	-0.08	0.444	0.002 (+)	0.985	0.201	0.02	0.066 (+)	0.567
Additive manufacturing technologies for prototyping	0.051 (-)	0.664	0.096	0.378	0.118	0.262	-0.097	0.261	-0.191 (+)	0.119
Additive manufacturing technol. for mass production	0.306 (-)	0.014	-0.062	0.578	-0.065	0.553	-0.178	0.053	-0.052 (+)	0.667
Software for production planning and scheduling	-0.06	0.601	-0.219	0.038	0.249	0.017	-0.011 (-)	0.899	-0.018 (+)	0.871
Near real-time production control system	-0.112	0.359	0.258	0.021	-0.093	0.392	-0.142	0.116	-0.139 (+)	0.241
Digital exchange of product/process data	-0.035	0.766	0.104	0.335	-0.108	0.354	0.007	0.94	0.006 (+)	0.955
Systems for automation and management of internal logistics	-0.04	0.75	-0.212	0.067	-0.054	0.624	0.008	0.931	-0.101 (+)	0.402
Devices for programming and handling of machines	-0.077	0.5	-0.133	0.201	-0.227	0.033	-0.062	0.471	0.113 (+)	0.303
Product lifecycle management systems	0.13	0.25	-0.086	0.404	-0.049 (+)	0.647	0.073	0.383	0.119 (+)	0.267
Technologies for safe human-machine interaction	0.008	0.946	-0.168	0.136	-0.145	0.221	0.161	0.083	-0.015 (+)	0.899
Digital visualization	-0.087	0.497	0.376	0.002	0.244	0.049	0.168	0.079	0.245 (+)	0.055
R		0.375		0.533		0.654		0.731		0.516
R ²		0.141		0.284		0.428		0.534		0.267
F		0.612		1.48		2.27		4.192		1.23
Sig.		0.924		0.088		0.003		0		0.235
Max V/F		2.098		2.098		2.065		2.144		2.489

only processing of composite materials increases revenues significantly. It was hypothesised that nano-technological production processes and biotechnology/genetic engineering methods enhance innovation revenues but, in fact, we obtained a negative, although non-significant sign. This might be because these technologies are not widespread and mostly in the trial phase.

The fourth regression (scrap rate) is significant, although there are no important contingencies. However, there seems to be a trade-off between AMT for different purposes. For example, a control system for shut down and control-automation systems for energy efficient production in fact augment scrap rate, probably due to the abrupt shutting down of machines. Processing techniques for composite materials and biotechnology/genetic engineering methods decrease scrap rate. On the other hand, processing techniques for alloy construction materials augments scrap rate significantly. These technologies are still not widespread and they are probably still used on a trial basis.

The fifth regression (profit) shows that none of the AMT increases profits significantly. Thirteen out of twenty AMT affect profit before tax positively, although not significantly. This fifth model is non-significant and thus cannot confirm our hypotheses from Table 2 that the majority of AMT will actually affect profit before tax positively. We do not find evidence in line with Kotha and Swamidass [11], according to whom AMT is more beneficial to larger companies. With some exceptions, we do not see profit benefits of AMT for manufacturing companies in Slovenia and Croatia, and that might be because it is in line with Zhou et al. [28], claiming that AMT adoption shows positive results in developed countries but not necessarily in less developed countries.

4 DISCUSSION AND IMPLICATIONS

Our main results show that contingency factors such as batch size, company size and product complexity do not influence staff costs, innovation revenues, scrap rate or profit significantly. Only contingency was for innovation revenues, which is significantly higher for Slovenia. So, context is important for innovation results but not for profitability. That is in line with Zhou et al. [28] which shows that developed countries have higher benefits from AMT than less developed countries. We did not find evidence of the positive effects of AMT use on the performance of SMEs as Raymond [5] found. Our control variable of company size was non-significant in all five regression analyses.

Our findings concur with the findings of Abd Rahman and Bennett [29] that less developed countries have lower benefits from AMT.

On the other hand, the researched AMT are really advanced, and they have impact on material consumption, scrap rate and profits, but not in the positive hypothesised relationship. For example, additive manufacturing technologies for mass production increase material consumption significantly. This might be because this technology is not yet widespread in mass production, so companies are probably using it on a trial basis. This trial basis then, affects profits negatively, although not significantly.

Biotechnology / genetic engineering methods – this technology is really in its infant stage, so the negative relationships to profits for now is understandable. Probably in current conditions, companies are only experimenting with the technology, but the negative impact on profits is due to investment into technology, which might bring benefits in the long run.

This research shows that investments into AMT do not have a positive effect on profits, that is, seven out of twenty AMT decrease profit before tax (but not significantly). This may be explained by the unfavourable economic conditions in the two countries in the research period, and that acquiring AMT actually demands investments, which may even be substantial, but might bring positive results in the long run. A longitudinal research would be beneficial to see whether AMT would bring benefits in time, when market conditions are more favourable.

However, as shown in Table 2, the same technology might hinder some other operative measures, so in terms of adopting a new technology one should follow the advice of Sahin [30] that investment into technology should be accompanied with continuous improvement. This is in line with Swink and Nair [3] who said that AMT requires a significant amount of overhead resources, including highly trained engineering, maintenance, and other technical staff. Costs associated with these resources, as well as significant capital equipment costs, may offset the direct cost efficiencies offered by AMT. The importance of aligning organisational processes with strategy through AMT is stressed in Gouvea da Costa and Pinheiro de Lima [31] and their integrated approach, which actually reinforces the concluding remarks of Swink and Nair [3]. In our case, control system for shut down and control-automation systems for energy efficient production are supposed to diminish material use, but they also increase scrap

rate. That is a clear trade off which managers should be aware of.

This research represents an empirical examination of how twenty AMTs affect operational and performance measures of the company. It should be noted that merely having AMT will not necessarily produce the desired results. There is still a substantial worker input, so workers' skills can increase positive effects arising from technology. This means that the implementation of AMT has to be planned carefully [32]. This work shows that AMT help companies in today's globally competitive market, but not in terms of profits. It was shown that AMT in fact augments the use of materials. This might be in accordance with Kotha and Swamidass [11] that technology should primarily be used for achieving growth and increasing revenue and not for cutting costs. Processing techniques for composite materials show a significant positive increase in innovation revenues and the whole model is significant. Processing techniques for composite materials and biotechnology / genetic engineering methods, even though still not in widespread use, do in fact reduce scrap rate significantly and the whole model is significant.

5 CONCLUSION AND LIMITATIONS

Our research studied company characteristics and contingencies, which was not done in previous literature. In this paper, five regression equations were performed, identifying the positive or negative impact of AMT on the researched variables. Our first research question, which contingencies affect technology use, did not turn out to be important for technology use and their effect on profits, decrease in the scrap rate, material and staff costs as a percentage of revenues. However, we did find a significant difference in innovation revenue by countries, and Slovenia is more developed than Croatia [33].

The technology section of the EMS instrument is displayed here and can be used to test the results on a larger scale. Our sample contains 138 companies, which may be considered relatively large. However, all the companies are from two neighbouring countries – Croatia and Slovenia – severely hit by recession, and both with very small markets, depending thus on exports. Moreover, Croatian and Slovenian manufacturing companies do not have large-scale production, but they rather embrace niche differentiation strategy. Therefore, there is a need for a study which would also involve companies with other strategies (such as cost leadership).

There are a limited number of papers researching the contingency theory in operations' management literature, but the problem is that, even articles having "AMT" in their title, still talk about technologies from the 1990 that were first categorised in Boyer et al. [10]. We add to the literature by researching real AMT, which are not even used widely in western developed countries.

6 ACKNOWLEDGEMENTS

This work is funded by the Croatian Scientific Foundation under Grant 1861-3535 – "Building Competitiveness of Croatian manufacturing". The authors also acknowledge the financial support from the Slovenian Research Agency (Research Core Funding No. P2-0190). This work was also supported by the Croatian Science Foundation under Grant 0-1861-2014-3535.

7 REFERENCES

- [1] Schuh, G., Graw, M., Schön, N. (2014). Exploitation-oriented manufacturing technology development. *Procedia CIRP*, vol. 17, p. 680-685, DOI:10.1016/j.procir.2014.02.026.
- [2] Baldwin, J.R., Sabourin, D. (2002). Advanced technology use and firm performance in Canadian manufacturing in the 1990s. *Industrial and Corporate Change*, vol. 11, no. 4, p. 761-789, DOI:10.1093/icc/11.4.761.
- [3] Swink, M., Nair, A. (2007). Capturing the competitive advantages of AMT: Design-manufacturing integration as a complementary asset. *Journal of Operations Management*, vol. 25, no. 3, p. 736-754, DOI:10.1016/j.jom.2006.07.001.
- [4] Kalchschmidt, M. (2012). Best practices in demand forecasting: Tests of universalistic, contingency and configurational theories. *International Journal of Production Economics*, vol. 140, no. 2, p. 782-793, DOI:10.1016/j.ijpe.2012.02.022.
- [5] Raymond, L. (2005). Operations management and advanced manufacturing technologies in SMEs: A contingency approach. *Journal of Manufacturing Technology Management*, vol. 16, no. 8, p. 936-955, DOI:10.1108/17410380510627898.
- [6] Machuca, J.A.D., Jiménez, C.H.O., Garrido-Vega, P., de los Ríos, J.L.P.D. (2011). Do technology and manufacturing strategy links enhance operational performance? Empirical research in the auto supplier sector. *International Journal of Production Economics*, vol. 133, no. 2, p. 541-550, DOI:10.1016/j.ijpe.2010.12.010.
- [7] Donaldson, L. (2001). *The Contingency Theory of Organizations*, Sage Publications, London, DOI:10.4135/9781452229249.
- [8] Sousa, R., Voss, C.A. (2008). Contingency research in operations management practices. *Journal of Operations Management*, vol. 26, no. 6, p. 697-713, DOI:10.1016/j.jom.2008.06.001.

- [9] Sirmon, D.G., Hitt, M.A. (2009). Contingencies within dynamic managerial capabilities: interdependent effects of resource investment and deployment on firm performance. *Strategic Management Journal*, vol. 30, no. 13, p. 1375-1394, DOI:10.1002/smj.791.
- [10] Boyer, K.K., Leong, G.K., Ward, P.T., Krajewski, L.J. (1997). Unlocking the potential of advanced manufacturing technologies. *Journal of Operations Management*, vol. 15, no. 4, p. 331-347, DOI:10.1016/S0272-6963(97)00009-0.
- [11] Kotha, S., Swamidass, P.M. (2000). Strategy, advanced manufacturing technology and performance: empirical evidence from U.S. manufacturing firms. *Journal of Operations Management*, vol. 18, no. 3., p. 257-277, DOI:10.1016/S0272-6963(99)00025-X.
- [12] Goyal, S., Grover, S. (2012). Advanced manufacturing technology effectiveness: A review of literature and some issues. *Frontiers of Mechanical Engineering*, vol. 7, no. 3, p. 256-267, DOI:10.1007/s11465-012-0330-7.
- [13] Percival, J. (2004). *Complementarities in the Implementation of Advanced Manufacturing Technologies*, PhD thesis, University of Waterloo, Waterloo, from: <http://citeseerx.ist.psu.edu/viewdoc/download?doi=10.1.1.72.6685&rep=rep1&type=pdf>, accessed on 2018-04-10.
- [14] Oliveira, M.L.M., Montevechi, J.A.B., Pinho, A.F., Miranda, R.C. (2017). Using hybrid simulation to represent the human factor in production systems. *International Journal of Simulation Modelling*, vol. 16, no. 2, p. 263-274, DOI:10.2507/IJSIMM16(2)7.378.
- [15] Ketokivi, M.A., Schroeder, R.G. (2004). Strategic, structural contingency and institutional explanations in the adoption of innovative manufacturing practices. *Journal of Operations Management*, vol. 22, no. 1, p. 63-89, DOI:10.1016/j.jom.2003.12.002.
- [16] Schroeder, R. G., Flynn, B. B. (eds.) (2002). *High Performance Manufacturing: Global Perspectives*. John Wiley & Sons, New York.
- [17] Crawford, K.M., Blackstone Jr., J.H., Cox, J.F. (1988). A study of JIT implementation and operating problems. *International Journal of Production Research*, vol. 26, no. 9, p. 1561-1568, DOI:10.1080/00207548808947966.
- [18] Nassimbeni, G. (1996). Factors underlying operational JIT purchasing practices: Results of an empirical research. *International Journal of Production Economics*, vol. 42, no. 3, p. 275-288, DOI:10.1016/0925-5273(95)00190-5.
- [19] He, S.H., Li, X.D., Wang, Y., Zhu, H.H. (2017). An optimization model for automobile mixed assembly line under multiple constraints. *International Journal of Simulation Modelling*, vol. 16, no. 4, p. 720-730, DOI:10.2507/IJSIMM16(4)C018.
- [20] Budak I., Mirkovic S., Sokac M., Santosi Z., Puskar T., Vukelic D. (2016). An approach to modelling of personalized bone grafts based on advanced technologies. *International Journal of Simulation Modelling*, vol. 15, no. 4, p. 637-648, DOI:10.2507/IJSIMM15(4)5.357.
- [21] Garcia-Alcaraz, J.L., Maldonado-Macias, A.A., Alor-Hernandez, G., Sanchez-Ramirez, C. (2017). The impact of information and communication technologies (ICT) on agility, operating, and economical performance of supply chain. *Advances in Production Engineering & Management*, vol. 12, no. 1, p. 29-40, DOI:10.14743/apem2017.1.237.
- [22] Lerher, T., Borovinsek, M., Ficko, M., Palcic, I. (2017). Parametric study of throughput performance in SBS/RS based on simulation. *International Journal of Simulation Modelling*, vol. 16, no. 1, p. 96-107, DOI:10.2507/IJSIMM16(1)8.372.
- [23] Dragic, M., Sorak, M. (2016). Simulation for Improving the Performance of Small and Medium Sized Enterprises. *International Journal of Simulation Modelling*, vol. 15, no. 4, p. 597-610, DOI:10.2507/IJSIMM15(4)2.343.
- [24] Rosi, B., Grasic, L., Dukic, G., Opetuk, T., Lerher, T. (2016). Simulation-based performance analysis of automated single-tray vertical lift module. *International Journal of Simulation Modelling*, vol. 15, no. 1, p. 97-108, DOI:10.2507/IJSIMM15(1)8.328.
- [25] Nair, A., Ataseven, C., Swamidass, P.M. (2013). An examination of the use of manufacturing technologies and performance implications in US plants with different export intensities. *International Journal of Production Research*, vol. 51, no. 11, p. 3283-3299, DOI:10.1080/00207543.2013.765069.
- [26] Finžgar, M., Podržaj, P. (2017). Machine-vision-based human-oriented mobile robots: A review. *Strojniški vestnik - Journal of Mechanical Engineering*, vol. 63, no. 5, p. 331-348, DOI:10.5545/sv-jme.2017.4324.
- [27] Meyers, L.S., Gamst, G., Guarino, A.J. (2006). *Applied Multivariate Research*, Sage Publication, Thousand Oaks.
- [28] Zhou, H., Leong, G.K., Jonsson, P., Sum, C-C. (2009). A comparative study of advanced manufacturing technology and manufacturing infrastructure investments in Singapore and Sweden. *International Journal of Production Economics*, vol. 120, no. 1, p. 42-53, DOI:10.1016/j.ijpe.2008.07.013.
- [29] Abd Rahman, A., Bennett, D. (2009). Advanced manufacturing technology adoption in developing countries: The role of buyer-supplier relationships. *Journal of Manufacturing Technology Management*, vol. 20, no. 8, p. 1099-1118, DOI:10.1108/17410380910997236.
- [30] Sahin, F. (2000). Manufacturing competitiveness: different systems to achieve the same results. *Production and Inventory Management Journal*, vol. 41, no. 1, p. 56-65.
- [31] Gouvea da Costa, S.E., Pinheiro de Lima, E. (2008). Advanced manufacturing technology adoption: an integrated approach. *Journal of Manufacturing Technology Management*, vol. 20, no. 1, p. 74-96, DOI:10.1108/17410380910925415.
- [32] Zhang, Q., Vonderembse, M.A., Cao, M. (2006). Achieving flexible manufacturing competence: The roles of advanced manufacturing technology and operations improvement practices. *International Journal of Operations & Production Management*, vol. 26, no. 6, p. 580-599, DOI:10.1108/01443570610666957.
- [33] CIA Fact Book, (2017). From <https://www.cia.gov/library/publications/the-world-factbook/rankorder/2003rank.html>, accessed on 2018-04-11.

Buckling Analysis of Axially Functionally Graded Tapered Nanobeams Resting on Elastic Foundations, Based on Nonlocal Elasticity Theory

Ma'en S. Sari¹ – Wael G. Al-Kouz^{2,*} – Anas Atieh³

¹German Jordanian University, Mechanical and Maintenance Engineering Department, Jordan

²German Jordanian University, Mechatronics Engineering Department, Jordan

³German Jordanian University, Industrial Engineering Department, Jordan

The stability analysis of nonlocal axially functionally graded tapered beams has been investigated. Euler-Bernoulli beams at the micro- or nanoscale are modeled using Eringen's nonlocal elasticity theory. The governing equations are derived using the differential constitutive relations, and the Chebyshev collocation method is utilized to convert the differential equation of motion into a set of algebraic equations. Next, the boundary conditions are applied, and the resulting eigenvalue problem is solved to obtain the critical buckling loads. The effects of the Winkler modulus parameter, the shear modulus parameter, the breadth taper ratio, the height taper ratio, the nonlocal scale coefficient, and the boundary conditions on the critical buckling loads have been studied.

Keywords: buckling, axially functionally graded beams, Eringen's nonlocal elasticity theory, Chebyshev collocation method, eigenvalue problem

Highlights

- The research aims to study the buckling behaviour of axially functionally graded nonlocal nanobeams.
- Effects of nonlocal scale parameter, Winkler modulus parameter, the shear modulus parameter, the breadth taper ratio, the height taper ratio, and the boundary conditions were investigated.
- The nonlocal elasticity theory and the Chebyshev collocation method were utilized.
- It was found that the afore-mentioned parameters have a significant influence on the critical buckling loads.

0 INTRODUCTION

Micro- and nanoelectromechanical systems have gained appreciable attention for their significant role in many engineering and modern technology fields such as aerospace, nuclear, composites, and electronics due to their excellent mechanical, electrical, and thermal properties in comparison to other structures at the normal (macro) length scale. During manufacturing, producing, assembling, and packaging, some micro- and nanostructures may have geometrical non-uniformities, as variations in the height and the width that may affect the dynamical behaviour of these structures.

For more efficient vibration control, and to provide weight reduction for greater structural efficiency, tapered structures can be used in different engineering applications. Therefore, it is worthwhile to model these non-uniform micro- and nanostructures to predict their dynamical behaviour. Besides, to increase the strength to weight ratio, orthotropic, anisotropic, composite, and functionally graded structures are commonly used in several industrial applications such as civil and aerospace structures. Moreover, the micro- and nanomaterials such as carbon nanotubes and graphene sheets cannot be considered as homogeneous due to the influence

of lattice distance or grain size on their mechanical properties.

To ensure that these properties vary smoothly and continuously within the structure, functionally graded (FG) materials, which are made from a mixture of ceramics and metal, can be used, and the properties of these FG materials can be tailored for specific purposes. In contrast, composite materials suffer from premature failure due to the abrupt change in material properties from the matrix to fibre and between the layers [1]. Additionally, these materials may experience the decay in the elastic characteristics as a result of delaminations and chemically unstable medium and lamina adhesives [1]. However, to date, no report has been found in the literature on the buckling behaviour of non-uniform functionally graded nonlocal beams resting on the linear elastic foundation. Motivated by these considerations and to improve the design of MEMS/NEMS, this article aims to study the buckling of nonlocal, double-tapered thin beams resting on elastic foundations.

It is known that the experimental and atomistic simulations and models are capable of showing the influence of the small-scale on the behaviour of micro- or nanostructures; however, these methods are expensive and restricted by computational capacity.

Since the local continuum theories for different structures are scale-free, they are not able to capture the small scale effect on the different properties for structures at the micro- or nanoscale. This makes them inadequate in predicting the dynamical behaviour for these structures [2]. To apply the continuum mechanics approach to the analysis of the micro- and nanostructures, logical and reasonable modifications that take into consideration the scale effect, should be introduced. For this purpose, several theoretical models have been proposed. Among these are the strain gradient theory, the modified coupled stress theory, and the nonlocal elasticity theory [3] and [4] that will be used in this article to carry out the buckling behaviour of nonlocal axially functionally graded Euler-Bernoulli beams resting on elastic foundations.

Calculating natural frequencies and understanding the buckling behaviour are the main issues from a design point of view, since the natural frequencies and the critical buckling loads can be considered to be dynamic properties of a structure. Thus, many researchers have been interested in investigating the free vibration and stability analyses of structures at the nanoscale. For example, Thang et al. [5] illustrated an analytical approach to analyse the nonlinear static buckling of imperfect functionally graded carbon nano-reinforced composite plates subjected to axial compression, for which several linear distributions of the volume fraction of carbon nanotubes were assumed to be graded through the thickness direction according to formulations that are based on Kirchhoff plate theory with Von Karman-type of nonlinearity.

Buckling characteristics of heated FG annular nanoplates resting on an elastic foundation and subjected to various types of thermal loadings were investigated by Ashoori et al. [6]. In their work, an exact analytical solution was introduced for three different types of thermal loadings, and the thermo-mechanical properties for the FG nanoplate were assumed to follow the power law model. The adjacent equilibrium criterion was analyzed by solving the nonlocal stability equations of FG annular. Moreover, a parametric study was conducted to examine the effects of different parameters on the critical buckling temperatures of the size-dependent FG nanoplates. It was concluded that the small-scale effects and thermal loading have a significant effect on thermal stability characteristics of FG annular nanoplates

In the study conducted by Challamel et al. [7], the small length scale effect of microstructured plates was investigated utilizing three different kinds of nonlocal plate theories, namely, the classical stress gradient Eringen's theory, continualization

of the discrete lattice model, and the combination of Eringen's model with some additional gradient curvature terms. Analytical solutions for the vibration and buckling of these equivalent continuous systems were obtained, and it was shown that the small length scale coefficient is dependent on the buckling mode and the geometry of the plate. Liu et al. [8] formulated the general equation for transverse vibration of a double-viscoelastic-FGM-nanoplate system with a visco-elastic Pasternak medium in between and each nanoplate subjected to in-plane edge loads based on the Eringen's nonlocal elastic theory and the Kelvin model. Many different factors, such as the structural damping, medium damping, small size effect, loading ratio, and Winkler modulus and shear modulus of the medium are included in the general equation. It was illustrated that the vibrational frequency of the system for the out-of-phase vibration is dependent on different factors, such as structural damping, small size effect and viscoelastic Pasternak medium, and it was found that the buckling load of the system for the in-phase buckling case is independent of the viscoelastic Pasternak medium. It was concluded that the buckling load for the out-of-phase case is a function of the small size effect, loading ratio, and Pasternak medium.

Golmakani and Rezatalab [9] analysed the non-uniform biaxial buckling analysis of an orthotropic single-layered graphene sheet embedded in a Pasternak elastic medium using the nonlocal Mindlin plate theory. All edges of the sheet were subjected to linearly varying normal stresses. The governing equations were derived based on first-order shear deformation theory, and the differential quadrature method was used to solve the governing equations for various boundary conditions. Effects of scale, aspect ratio, polymer matrix properties, type of planar loading, mode numbers, and boundary conditions were discussed in details. Taati [10] utilized the differential operator method to investigate the buckling and post-buckling behaviour of uniform functionally graded microbeams subjected to axial compressive force and thermal loading. It was assumed that the beams were resting on an elastic foundation. The modified couple stress theory and the principle of minimum potential energy were used to derive the governing equations. Moreover, Ebrahimi and Barati [12] applied the nonlocal strain gradient theory to examine the buckling behaviour of axially functionally graded nanobeams resting on a variable elastic medium. Hamilton's principle was used to obtain the governing equations, and a Galerkin-based solution was implemented to obtain

the buckling loads. Ebrahimi et al. [12] carried out the vibrational and buckling behaviour of nanotubes utilizing Eringen's nonlocal elasticity theory and considering the surface effects. The governing equation was derived using Hamilton's principle, and the natural frequencies, as well as the buckling loads, were obtained by applying the differential transform method. Latifi et al. [13] investigated the buckling problem of thin rectangular functionally graded plates subjected to proportional biaxial compressive loadings with arbitrary edge supports. The classical plate theory based on the physical neutral plane was applied, and the displacement function was considered to be in the form of a double Fourier series. The effects of the plate aspect ratio, the loading proportionality factor on the buckling load of the plate with different common boundary conditions were studied.

Pradhan and Murmu [14] implemented the nonlocal elasticity theory to study the buckling behaviour of single-layered graphene sheets embedded in an elastic medium modelled by Winkler-type and Pasternak-type foundations. The governing differential equations based on the principle of virtual work were derived. It was shown that the buckling loads are strongly dependent on the small-scale coefficients and the stiffness of the surrounding elastic medium. Shahidi et al. [15] developed a nonlocal continuum model based on Eringen's theory for vibration analysis of orthotropic nanoplates (modelled as Kirchhoff plates) with arbitrary variation in thickness. The variational principle and Ritz functions were employed, and the effect of thickness variation on natural frequencies was investigated for different nonlocal parameters, mode numbers, geometries and boundary conditions.

Moreover, Asbaghian Namin and Pilafkan [16] investigated the free vibration of defective graphene sheets via nonlocal elasticity theory, and the first-order shear deformation was used to derive the governing equations, which were solved using a generalized differential quadrature method. It was shown that the shapes and distributions of the structural defects, the number of missing atoms, and the vacancy defect reconstruction have a noticeable effect on the natural frequencies of the graphene sheets. Zhang et al. [17] applied the nonlocal elasticity theory to carry out the vibration behaviour of quadrilateral single-layered graphene sheets (modelled as Kirchhoff plates) in a magnetic field. The governing equations were solved by employing the element-free kp-Ritz method. The effects of the skew angles, nonlocal parameter, the magnetic field, and the boundary conditions on

the fundamental frequencies of the single-layered graphene sheets were discussed.

Furthermore, Li and Hu [18] studied the free torsional vibration behaviour of tubes made of a bi-directional functionally graded material. It was assumed that the material properties of the nanotube vary in the length direction according to an exponential distribute function and in the radius direction according to a power-law function. It was concluded that the torsional frequencies are increased by decreasing nonlocal parameters, and it was observed that this parameter does not affect the mode shapes of the nanotubes. The vibration formulation for a nanoscaled beam embedded in an elastic matrix under the effect of thermal environments was presented by Demir and Civalek [19]. The governing equations were obtained using Hamilton's principle, the variational approach, and the nonlocal elasticity theory. A new Finite element method was utilized to solve for the vibrational frequencies that were affected by the Pasternak foundation parameter, the small-scale parameter, and the thermal effect.

Additionally, Murmu and Adhikari [20] considered the nonlocal vibration of a double-nanoplate-system bonded by an elastic medium. Closed form solutions were obtained for the natural frequencies of a nonlocal double-nanoplate-system. It was concluded that the increase of the stiffness of the coupling springs in the system reduces the small-scale effects during the asynchronous modes of vibration.

In the present article, Eringen's nonlocal elasticity theory is utilized to study the small-scale effect on the buckling behaviour of axially functionally graded (AFG) tapered Euler-Bernoulli beams resting on an elastic foundation. The governing equation is derived using Eringen's nonlocal constitutive relations along with Hamilton's principle. The Chebyshev spectral collocation method is applied to transform the governing differential equation into a system of algebraic equations, and then the resulted eigenvalue problem is solved to obtain the natural frequencies and the critical buckling loads. In this study, the variable height, breadth, cross-sectional area, second moment of area, mass density, and Young's modulus will be presented as the variable coefficients of the governing differential equation. It is believed that the results of this study can be used for the design and optimization of double-tapered nanodevices made of axially functionally graded materials and are embedded in elastic medium, and may help in studying the buckling response of double-tapered nanodevices (that can be modeled as thin beams) when

used as mechanical resonators, sensors, actuators, and vibrating components.

1 THEORY

1.1 Chebyshev Spectral Collocation

The Chebyshev points are the points that represent the projections on the interval $[-1, 1]$ of equally spaced points of a unit circle. These points are given as [21]:

$$x_j = \cos(j\pi / N), \quad j = 0, 1, \dots, N. \quad (1)$$

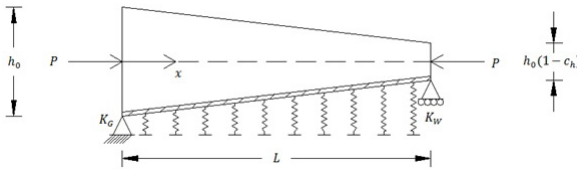


Fig. 1. Nonlocal AFG tapered Euler-Bernoulli beam resting on Elastic foundation and subjected to a constant axial compressive load

The Chebyshev differentiation Matrix DN of size $(N+1) \times (N+1)$ can be obtained by interpolating a Lagrange polynomial of degree N at each Chebyshev point, differentiating the polynomial, and then finding its derivative at each Chebyshev point. The entries of the D_N matrix are found in [21]. The Chebyshev collocation method can be used to solve ordinary or partial differential equations by representing the n th derivative of a function by $Dn = (D_N)^n$.

2.2 Nonlocal Theory

At the macro scale, the stress at a point in a body depends on the strain at the same point. However, in the nonlocal elasticity theory pioneered by Eringen [3], the stress at a point in an elastic domain is related to the stress field at all points in the domain. Eringen's theory is based on the atomic theory of lattice dynamics and experimental results on phonon scattering and dispersion [3].

The stress tensor t_{ij} is defined for nonlocal linear elastic solids as [3]:

$$t_{ij} = \int_V \alpha(|x' - x|) \sigma_{ij}(x') dV(x'), \quad (2)$$

where x is a reference point in the elastic domain, $\alpha(|x' - x|)$ is the non-local kernel attenuation function which introduces the nonlocal effects at the reference point x produced by the local stress σ_{ij} at any point x' , and $|x' - x|$ is the Euclidean form of the distance. Eringen [3] introduced a linear differential operator

ζ , defined by $\zeta = 1 - (e_0 l)^2 \nabla^2$, where e_0 is a material constant estimated by experiments, simulations, or other models and theories. In Eringen's analysis, the value of e_0 was taken to be 0.39. Furthermore, the constant l represents the characteristic internal length which (for structures at the nanoscale) is of the same order of the external length. The Laplace operator ∇^2 is given as:

$$\nabla^2 = \frac{\partial^2}{\partial x^2}. \quad (3)$$

According to Eringen [3], the integral constitutive relation of Eq. (3) could be simplified to the following form [4]:

$$(1 - (e_0 l)^2 \nabla^2) t_{ij} = \sigma_{ij}. \quad (4)$$

Due to its simple form, Eq. (4) has been used by many researchers in applying the nonlocal theory to study and analyze the buckling, vibration, and mechanics of micro- and nanostructures.

Fig. 1. shows a Euler-Bernoulli beam resting on an elastic foundation and subjected to a constant compressive force P . The governing differential equation of motion for this system is given by [22] and [23]:

$$\frac{d^2}{dx^2} \left[E(x) I(x) \frac{d^2 \hat{w}}{dx^2} \right] + P \frac{d^2 \hat{w}}{dx^2} + k_w \hat{w} - k_G \frac{d^2 \hat{w}}{dx^2} = 0, \quad (5)$$

where x is the spatial coordinate, \hat{w} is the transverse deflection, $I(x)$ is the beam's area moment of inertia of the cross-section, $E(x)$ is Young's modulus of Elasticity, and k_w and k_G are the Winkler modulus and the shear modulus parameters of the surrounding medium, respectively.

For a Euler-Bernoulli beam, the bending moment is given as:

$$M(x) = -E(x) I(x) \frac{d^2 \hat{w}}{dx^2}. \quad (6)$$

In light of Eq. (5), $d^2 M(\hat{x}) / d\hat{x}^2$ is given by:

$$\frac{d^2 M}{dx^2} = P \frac{d^2 \hat{w}}{dx^2} + k_w \hat{w} - k_G \frac{d^2 \hat{w}}{dx^2}. \quad (7)$$

From Eq. (5) and utilizing Hooke's law, the constitutive relation for the moment $M(\hat{x}, \hat{t})$ is given as:

$$M(x) - (e_0 a)^2 \frac{d^2 M}{dx^2} = -E(x) I(x) \frac{d^2 \hat{w}}{dx^2}. \quad (8)$$

Inserting Eq. (8) into Eq. (7), yields:

$$M(x) = (e_0 a)^2 \left[P \frac{d^2 \hat{w}}{dx^2} + k_w \hat{w} - k_G \frac{d^2 \hat{w}}{dx^2} \right] - E(x) I(x) \frac{d^2 \hat{w}}{dx^2}. \quad (9)$$

Substituting Eq. (9) into Eq. (6), the equation of the transverse motion of the nonlocal Euler-Bernoulli beam resting on an elastic foundation and subjected to a constant compressive force is given as:

$$(e_0 a)^2 \left[P \frac{d^2 \hat{w}}{dx^2} + k_w \hat{w} - k_G \frac{d^2 \hat{w}}{dx^2} \right] - E(x) I(x) \frac{d^2 \hat{w}}{dx^2} - (e_0 a)^2 \left[(e_0 a)^2 \left(P \frac{d^4 \hat{w}}{dx^4} + k_w \frac{d^2 \hat{w}}{dx^2} - k_G \frac{d^4 \hat{w}}{dx^4} \right) \right] + (e_0 a)^2 \frac{d^2}{dx^2} \left[E(x) I(x) \frac{d^2 \hat{w}}{dx^2} \right] = -E(x) I(x) \frac{d^2 \hat{w}}{dx^2}. \quad (10)$$

Simplifying and collecting terms yields:

$$\frac{d^2}{dx^2} \left[E(x) I(x) \frac{d^2 \hat{w}}{dx^2} \right] + P \frac{d^2 \hat{w}}{dx^2} - (e_0 a)^2 P \frac{d^4 \hat{w}}{dx^4} + k_w \hat{w} - k_G \frac{d^2 \hat{w}}{dx^2} - (e_0 a)^2 k_w \frac{d^2 \hat{w}}{dx^2} + (e_0 a)^2 k_G \frac{d^4 \hat{w}}{dx^4} = 0. \quad (11)$$

In the present study, $E(x)$ and $I(x)$ are given as [22]:

$$E(x) = E_0 \left(1 + \frac{x}{L} \right), \quad I(x) = I_0 \left(1 - c_b \frac{x}{L} \right) \left(1 - c_h \frac{x}{L} \right)^3, \quad (12)$$

where E_0 and I_0 are respectively the modulus of elasticity, and area moment of inertia at $x=0$, c_b is the breadth taper ratio, and c_h is the height taper ratio. To obtain the normalized equations, the dimensionless parameters are introduced as:

$$X = \frac{x}{L}, \quad W = \frac{\hat{w}}{L}, \quad \mu = \frac{e_0 a}{L}, \quad \lambda = \frac{PL^2}{E_0 I_0}, \quad K_w = \frac{k_w L^4}{E_0 I_0}, \quad K_G = \frac{k_G L^2}{E_0 I_0}, \quad E(X) = \frac{E(x)}{E_0}, \quad I(X) = \frac{I(x)}{I_0}. \quad (13)$$

Substituting Eq. (13) into Eq. (11) and rearranging, yields:

$$\frac{d^2}{dX^2} \left(E(X) I(X) \frac{d^2 W}{dX^2} \right) + K_w W - K_G \frac{d^2 W}{dX^2} - \mu^2 K_w \frac{d^2 W}{dX^2} + \mu^2 K_G \frac{d^4 W}{dX^4} = \lambda \left(-\frac{d^2 W}{dX^2} + \mu^2 \frac{d^4 W}{dX^4} \right). \quad (14)$$

The critical buckling loads are determined by solving Eq. (14) as an eigenvalue problem.

2 SOLUTION PROCEDURE

The Chebyshev spectral collocation method is used to discretize the governing equation and the boundary conditions. It is known that for structures modelled as Euler-Bernoulli beams, two boundary conditions should be satisfied at the edges of the beam, and as there is only one unknown at each point $W_{i,j}$, therefore, the Chebyshev collocation method can be applied to satisfy one boundary condition only. To overcome this difficulty, the boundary conditions are applied by expressing the displacement at the boundary point and its adjacent point in terms of the displacement at other points in the domain. For example, the boundary conditions of a beam with clamped ends are given as:

$$W(0) = \frac{\partial W(0)}{\partial X} = W(1) = \frac{\partial W(1)}{\partial X} = 0. \quad (15)$$

Applying the Chebyshev collocation method, these conditions are expressed as:

$$W_1 = 0, \quad D_{1,1}^1 W_1 + D_{1,2}^1 W_2 + D_{1,N}^1 W_N + D_{1,N+1}^1 W_{N+1} = -\sum_{k=3}^{N-1} D_{1,k}^1 W_k, \quad W_{N+1} = 0, \quad D_{N+1,1}^1 W_1 + D_{N+1,2}^1 W_2 + D_{N+1,N}^1 W_N + D_{N+1,N+1}^1 W_{N+1} = -\sum_{k=3}^{N-1} D_{N+1,k}^1 W_k. \quad (16)$$

As the X -axis is normalized to be in the range of $[0, 1]$, the original Chebyshev points are shifted to be in this interval. Accordingly, the Chebyshev differentiation matrices will have different entries than those obtained by Trefethen [21], as they depend on the distribution of the points.

Eq. (16) is written in matrix-vector form as:

$$\begin{bmatrix} D_{1,2}^1 & D_{1,N}^1 \\ D_{N+1,2}^1 & D_{N+1,N}^1 \end{bmatrix} \begin{Bmatrix} W_2 \\ W_N \end{Bmatrix} = \begin{Bmatrix} -\sum_{k=3}^{N-1} D_{1,k}^1 W_k \\ -\sum_{k=3}^{N-1} D_{N+1,k}^1 W_k \end{Bmatrix}. \quad (17)$$

From Eq. (17), the displacements at the points adjacent to the boundaries are given as:

$$\begin{Bmatrix} W_2 \\ W_N \end{Bmatrix} = \frac{1}{\text{Det}} \begin{bmatrix} D_{N+1,N}^1 & D_{1,N}^1 \\ D_{N+1,2}^1 & D_{1,2}^1 \end{bmatrix} \begin{Bmatrix} -\sum_{k=3}^{N-1} D_{1,k}^1 W_k \\ -\sum_{k=3}^{N-1} D_{N+1,k}^1 W_k \end{Bmatrix}, \quad (18)$$

where Det is the determinant of the 2×2 matrix in the left side of Eq. (18) and is given by:

$$Det = (D_{1,2}^1 \times D_{N+1,N}^1) - (D_{1,N}^1 \times D_{N+1,2}^1). \quad (19)$$

From Eq. (18), the displacements W_2 and W_N are written in terms of the displacements at the other points as:

$$W_2 = \frac{1}{Det} \left(-D_{N+1,N}^1 \sum_{k=3}^{N-1} D_{1,k}^1 W_k + D_{1,N}^1 \sum_{k=3}^{N-1} D_{N+1,k}^1 W_k \right), \quad (20)$$

$$W_N = \frac{1}{Det} \left(D_{N+1,2}^1 \sum_{k=3}^{N-1} D_{1,k}^1 W_k - D_{1,2}^1 \sum_{k=3}^{N-1} D_{N+1,k}^1 W_k \right). \quad (21)$$

As a result, the Chebyshev collocation matrices are modified as:

$$\begin{aligned} \bar{D}_{i,k}^n &= \sum_{k=3}^{N-1} D_{i,k}^n \\ &+ D_{i,2}^n \frac{1}{Det} \left(-D_{N+1,N}^1 \sum_{k=3}^{N-1} D_{1,k}^1 + D_{1,N}^1 \sum_{k=3}^{N-1} D_{N+1,k}^1 \right) \\ &+ D_{i,N}^n \frac{1}{Det} \left(D_{N+1,2}^1 \sum_{k=3}^{N-1} D_{1,k}^1 - D_{1,2}^1 \sum_{k=3}^{N-1} D_{N+1,k}^1 \right) \end{aligned} \quad (22)$$

for $i = 3, 4, \dots, N-1$.

The boundary conditions of a beam with simply supported ends are given as:

$$W(0) = \frac{\partial^2 W(0)}{\partial X^2} = W(1) = \frac{\partial^2 W(1)}{\partial X^2} = 0. \quad (23)$$

In this case, the boundary conditions are expressed using the Chebyshev collocation method as in Eq. (16), except that each differentiation matrix D^1 is substituted with the differentiation matrix D^2 . Eq. (14) is discretized by the Chebyshev collocation method as:

$$\begin{aligned} &\left((R1 \times \bar{D}^2) + (R2 \times \bar{D}^3) + (R3 \times \bar{D}^4) \right) \{W\} = \\ &\left(+K_w I - K_G \bar{D}^2 - \mu^2 K_w \bar{D}^2 + \mu^2 K_G \bar{D}^4 \right) \{W\} = \\ &\lambda (-\bar{D}^2 + \mu^2 \bar{D}^4) \{W\}, \end{aligned} \quad (24)$$

where I is a $(M-4) \times (M-4)$ identity matrix, $R1$, $R2$, and $R3$ are diagonal $(M-4) \times (M-4)$ matrices with values of $R1_i$, $R2_i$ and $R3_i$ on the main diagonal, respectively, where:

$$\begin{aligned} R1_i &= (2c_b(c_h x_i - 1))^3 \\ &+ (6c_h(c_b + 2c_b x_i - 1)(c_h x_i - 1)^2) \\ &+ (6c_h^2(1 + x_i)(1 - c_b x_i)(1 - c_h x_i)), \end{aligned} \quad (25)$$

$$\begin{aligned} R2_i &= (2(c_b - 2c_b x_i - 1)(c_h x_i - 1)^3) \\ &+ (6c_h(1 + x_i)(1 - c_b x_i)(1 - c_h x_i - 1)), \end{aligned} \quad (26)$$

$$R3_i = (1 + x_i)(1 - c_b x_i)(1 - c_h x_i)(c_h x_i - 1)^2, \quad (27)$$

3 RESULTS AND DISCUSSION

There are no results for the critical buckling loads for micro- or nanoaxially functionally graded non-uniform Euler-Bernoulli beams resting on elastic foundations and subjected to constant axial compressive forces based on the nonlocal elasticity theory. Thus, for validation purpose, the comparison is made with local AFG non-uniform Euler-Bernoulli that are not embedded in the elastic medium, by setting the scale effect, the Winkler modulus parameter, and the shear modulus parameter to zero. To demonstrate the accuracy of the results obtained from the proposed technique, the critical buckling loads of local orthotropic non-uniform AFG Euler-Bernoulli beams with simply supported and clamped edges are compared with those obtained by Shahba and Rajasekaran [22]. The notation S-S denotes a beam that is simply supported at both edges, whereas the notation C-C denotes a beam with clamped edges. To show the stability and the accuracy of the proposed technique, a convergence study is conducted for the non-dimensional critical loads of local AFG beams with simply supported and clamped edges. From Table 1, it can be observed that the sufficient number of points to attain accurate results is $N=10$ for S-S beams, and $N=12$ for C-C beams.

Table 1. Convergence of Non-dimensional critical load for AFG S-S and C-C tapered beams, ($c_h = c_b = 0.2$, $\mu = K_w = K_G = 0$)

	S-S	C-C		S-S	C-C
N=7	9.5876	38.0371	N=11	9.5971	37.6022
N=8	9.5979	37.5838	N=12	9.5971	37.6023
N=9	9.5976	37.5967	N=13	9.5971	37.6023
N=10	9.5971	37.6020	Ref. [38]	9.5971	37.6023

As shown in Tables 2 and 3, it is clear that the results of the proposed model are in good agreement with those obtained by Shahba and Rajasekaran [22]. Additionally, the generated results for an isotropic and uniform S-S nonlocal beam (not embedded in an elastic medium) are compared to those obtained by Reddy [24], as shown in Table 4. Very good agreement is noted, and these tables reflect the validity of the proposed model and solution.

Table 2. Non-dimensional critical load ($\lambda = P_{cr}L^2 / E_0I_0$) for an AFG C-C tapered beam

c_h	c_b	0	0.2	0.8
0	Present Study	57.3940	51.7856	30.8922
	Ref. [22]	57.3940	51.7856	30.8922
0.2	Present Study	41.9169	37.6023	21.6802
	Ref. [22]	41.9169	37.6023	21.6802
0.4	Present Study	28.1794	25.0890	13.8242
	Ref. [22]	28.1794	25.0890	13.8242
0.6	Present Study	16.3412	14.3958	7.4275
	Ref. [22]	16.3412	14.3958	7.4275
0.8	Present Study	6.6801	5.7836	2.6649
	Ref. [22]	6.6801	5.7836	2.6649

Table 3. Non-dimensional critical load ($\lambda = P_{cr}L^2 / E_0I_0$) for an AFG S-S tapered beam

c_h	c_b	0	0.2	0.8
0	Present Study	14.5112	13.1398	8.3957
	Ref. [22]	14.5112	13.1398	8.3957
0.2	Present Study	10.6860	9.5971	5.8498
	Ref. [22]	10.6860	9.5971	5.8498
0.4	Present Study	7.2831	6.4715	3.7019
	Ref. [22]	7.2831	6.4715	3.7019
0.6	Present Study	4.3287	3.7892	1.9748
	Ref. [22]	4.3287	3.7892	1.9748
0.8	Present Study	1.8667	1.5950	0.7075
	Ref. [22]	1.8667	1.5950	0.7075

Table 4. Comparison of the Buckling loads with Reddy [24] for an isotropic S-S uniform beam

μ	Present Study	Ref. [24]
0	9.8696	9.8696
$0.5^{1/2} / 10$	9.4055	9.4055
$1.0^{1/2} / 10$	8.9830	8.9830
$1.5^{1/2} / 10$	8.5969	8.5969
$2.0^{1/2} / 10$	8.2426	8.2426
$2.5^{1/2} / 10$	7.9163	7.9163
$3.0^{1/2} / 10$	7.6149	7.6149
$3.5^{1/2} / 10$	7.3356	7.3356
$4.0^{1/2} / 10$	7.0761	7.0761
$4.5^{1/2} / 10$	6.8343	6.8343
$5.0^{1/2} / 10$	6.6085	6.6085

Variations of the dimensionless critical buckling loads at different values of the scale parameter of AFG nano C-C and S-S beams with $c_b = c_h = 0.2$, $K_G = 10$ and $K_W = 200$ are presented in Fig. 2. The scale parameter is taken in the range of 0 to 1. It is observed that as the scale parameter increases, the buckling loads decrease. The rate at which the buckling loads decrease is higher for the AFG nano C-C beams than

that for the AFG nano S-S beams. Additionally, as shown in the figure, the dimensionless buckling loads for the AFG C-C and S-S nanobeams have the same value for $\mu > 0.2$.

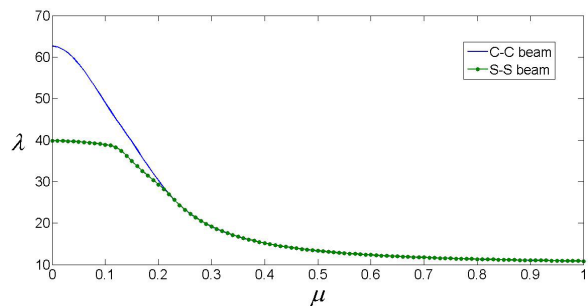


Fig. 2. Variation of the critical buckling load with the nonlocal parameter of a C-C and S-S AFG Euler Bernoulli beam ($c_b = c_h = 0.2$, $K_G = 10$, $K_W = 200$)

Fig. 3 shows the effect of the breadth taper ratio (c_b) on the critical dimensionless buckling loads of AFG C-C and S-S beams with $c_h = 0.2$, $K_G = 10$ and $K_W = 200$. The breadth taper ratio is taken in the range of 0 to 0.8. It is observed that as the value of c_b increases, the buckling load decreases, and the buckling load of the AFG C-C beam is more sensitive to the increase in c_b than the buckling load of the AFG S-S beam. For $\mu = 0$, it is noticed from Fig. 3a that as c_b increases from 0 to 0.8, the buckling load of the AFG C-C beam decreases from 66.98 to 46, whereas for the AFG S-S beam, it decreases from 40.95 to 33.65. In Fig. 3b, the effect of the breadth ratio (c_b) on the critical dimensionless buckling loads of AFG C-C and S-S nonlocal beams with $c_h = 0.2$, $K_G = 10$, $K_W = 200$, and $\mu = 0.1$ is presented. As observed from Fig. 3, the increase in c_b has a greater influence on the dimensionless buckling load of the AFG C-C nonlocal beams than that on the dimensionless buckling load of the AFG S-S nonlocal beams. Moreover, as c_b increases, the difference between the dimensionless buckling loads for the AFG C-C and S-S nanobeams becomes smaller.

The variations of the dimensionless critical buckling loads at different values of the height taper ratio (c_h) of AFG C-C and S-S beams with $c_b = 0.2$, $K_G = 10$ and $K_W = 200$ are presented in Fig. 4a. As for the breadth taper ratio, the height taper ratio is taken in the range of 0 to 0.8. The figure reveals that the critical buckling load decreases as the value of c_h increases, and the buckling load of the AFG C-C beam is more sensitive to the increase in c_h than that of the AFG S-S beam. The figure shows that as c_h increases from 0 to 0.8, the buckling load of the AFG C-C beam decreases

from 76.8 to 22.79, whereas for the AFG S-S beam, it decreases from 43.33 to 17.68. The effect of c_h on the critical dimensionless buckling loads of AFG C-C and S-S nonlocal beams with $c_b=0.2$, $K_G=10$, $K_W=200$ and $\mu=0.1$ is shown in Fig. 4b. It is noticed that as c_h increases from 0 to 0.58, the difference between the dimensionless buckling loads for the AFG C-C and S-S nanobeams becomes smaller, and for $c_h>0.58$, the critical buckling loads for the AFG C-C and S-S nanobeams are equal.

Fig. 5a shows the effect of shear modulus parameter (K_G) on the critical dimensionless buckling load of an axially functionally graded S-S and C-C beams with $c_b=c_h=0.2$, $K_W=200$ and $\mu=0$. It is observed that as the value of the shear modulus parameter increases, the critical buckling load increases, and the buckling load for the C-C beam is higher than that for the S-S beam for the same value

of K_G . However, the rate at which the buckling load increases with K_G is higher for the S-S beam. For example, as K_G increases from 0 to 10, the increasing rate of the buckling load is 33 % for the S-S beam and 19 % for the C-C beam. In Fig. 5b, the effect of K_G on the buckling load with $c_b=c_h=0.2$, $K_W=200$, and $\mu=0.1$ is presented. As in Fig. 5a, the figure reveals that the buckling load increases as K_G increases, however, the increasing rate is smaller than that when $\mu=0$. Furthermore, it is observed that the buckling load of the AFG C-C nanobeams is more affected by the increase of the scale parameter than that for the AFG S-S nanobeams. For instance, at $K_G=0$, the buckling load for the AFG C-C nanobeam decreases from 53 to 38 as the scale parameter increases from 0 to 0.1, whereas for the AFG S-S nanobeam it decreases from 30 to 28 as the scale parameter increases from 0 to 0.1.

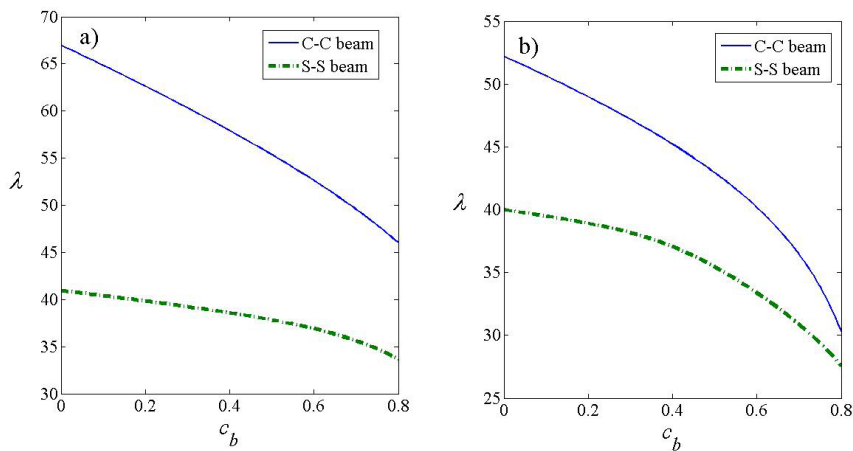


Fig. 3. Variation of the critical buckling load with the breadth ratio of a C-C and S-S AFG Euler-Bernoulli beam ($c_h = 0.2$, $K_G = 10$, $K_W = 200$; a) $\mu = 0$, and b) $\mu = 0.1$)

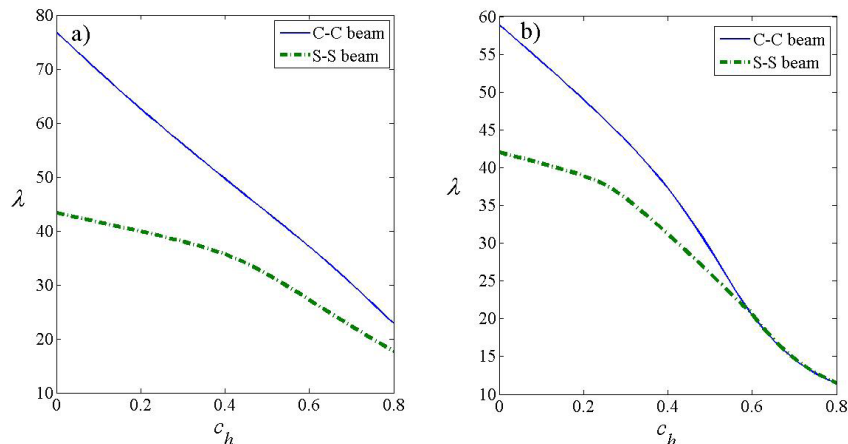


Fig. 4. Variation of the critical buckling load with the height ratio of a C-C and S-S AFG Euler-Bernoulli beam ($c_b = 0.2$, $K_G = 10$, $K_W = 200$; a) $\mu = 0$, and b) $\mu = 0.1$)

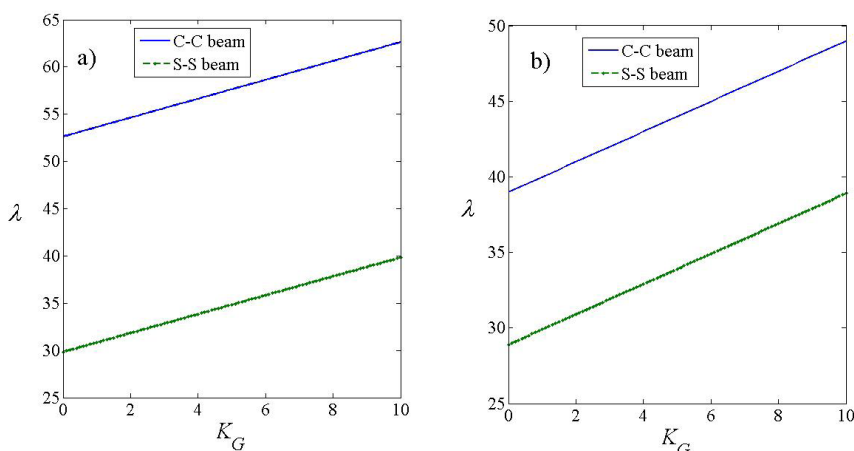


Fig. 5. Variation of the critical buckling load with shear modulus parameter of a C-C and S-S AFG Euler-Bernoulli beam ($c_b = c_h = 0.2$, $K_W = 200$; a) $\mu = 0$, and b) $\mu = 0.1$)

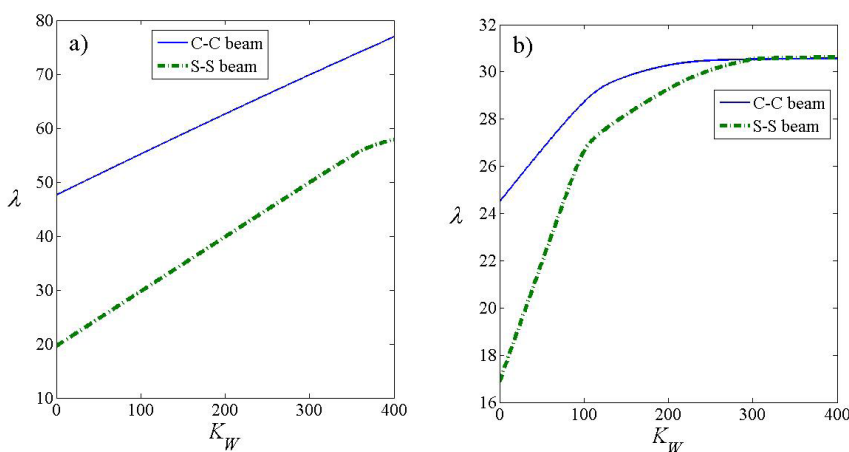


Fig. 6. Variation of the critical buckling load with Winkler modulus parameter of a C-C and S-S AFG Euler-Bernoulli beam ($c_b = c_h = 0.2$, $K_G = 10$; a) $\mu = 0$, and b) $\mu = 0.2$)

Fig. 6a shows the effect of the Winkler modulus parameter (K_W) on the critical dimensionless buckling loads of AFG C-C and S-S nonlocal beams with $c_b = c_h = 0.2$, $K_G = 10$ and $\mu = 0$. The Winkler modulus parameter is taken in the range of 0 to 400. Similar values of modulus parameter were taken by Pardhan and Murmu [14]. It is concluded that as the value of K_W increases, the buckling load linearly increases with a constant slope, and the increasing rate for the dimensionless buckling load of the AFG S-S nonlocal beams is greater than that of the AFG C-C nonlocal beams. In Fig. 6b, the effect of the Winkler modulus parameter (K_W) on the critical dimensionless buckling loads of AFG C-C and S-S nonlocal beams with $c_b = c_h = 0.2$, $K_G = 10$ and $\mu = 0.2$ is presented. The figure reveals that the increasing rate of the dimensionless buckling load depends on the range of

the Winkler modulus parameter. For example, for the AFG S-S nonlocal beam, the increasing rate of the dimensionless buckling load is approximately 59 % as K_W increases from 0 to 104, 14 % as K_W increases from 104 to 296, and only 0.4 % as K_W increases from 296 to 400. Similar observations can be made for the AFG C-C nonlocal beams. A point of interest is that the dimensionless buckling loads for the S-S and C-C beams become equal to each other for $K_W > 296$.

For a more general view, three-dimensional plots are shown in Figs. 7 and 8. In Fig. 7, the dimensionless critical buckling loads of the AFG S-S nanobeams with $c_b = c_h = 0.2$, and $K_G = 10$, are plotted versus the nonlocal scale parameter and the Winkler modulus parameter. It is shown that as the scale parameter increases, the rate at which the dimensionless critical buckling load increases with the Winkler modulus

parameter becomes smaller. For example, at $\mu=0$, the dimensionless critical buckling load of the S-S nanobeams increases from 19.6 to 57.78 as K_W increases from 0 to 400. On the other hand, at $\mu=1$, the dimensionless critical buckling load increases from 10.82 to 10.86 as K_W increases from 0 to 400. This leads us to conclude that the scale parameter is more dominant than the Winkler modulus parameter, and at relatively high values of the nonlocal scale parameter, the value of the Winkler modulus parameter has a negligible influence on the dimensionless critical buckling loads.

In Fig. 8, the dimensionless critical buckling loads of the AFG S-S nanobeam with $c_h=0.2$, $K_W=300$ and $K_G=5$, are plotted versus the nonlocal scale parameter and the breadth taper ratio (c_b). The figure reveals that the dimensionless critical buckling loads decrease with the increase in the nonlocal scale parameter and the breadth taper ratio.

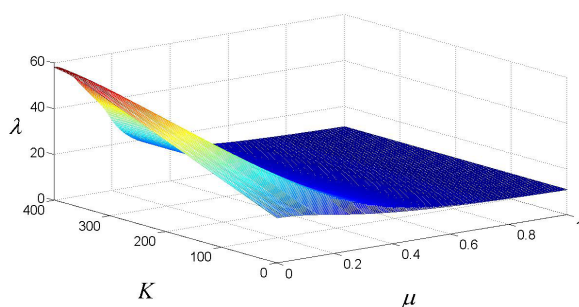


Fig. 7. Variation of the critical buckling load of a nonlocal AFG S-S Euler-Bernoulli beam with the nonlocal parameter and Winkler modulus parameter ($c_b=c_h=0.2$, $K_G=10$)

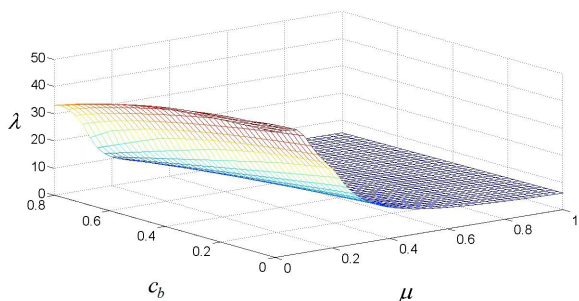


Fig. 8. Variation of the critical buckling load of a nonlocal AFG S-S Euler-Bernoulli beam with the nonlocal parameter and the breadth taper ratio ($c_h=0.2$, $K_G=5$, $K_W=300$)

4 CONCLUSIONS

The buckling behaviour of nonlocal axially functionally graded tapered Euler-Bernoulli beams embedded in the elastic medium was performed.

Eringen's nonlocal elasticity theory was used to derive the governing equation of motion. The Chebyshev spectral collocation method was utilized, and the boundary conditions were applied by expressing the displacements at the boundaries and their adjacent points in terms of the displacements at all other points in the domain, and then the resulting eigenvalue problem was solved to obtain the critical buckling loads. The effects of the nonlocal scale coefficient, the Winkler modulus parameter, the shear modulus parameter, breadth taper ratio, height taper ratio, and the boundary conditions on the critical buckling loads were studied. It was observed that the nonlocal scale parameter has a significant effect on the critical buckling loads, and the results reveal that beams with clamped ends are more affected by the scale parameter. In general, the critical buckling loads for the C-C beams are higher than those for the S-S beams; however, at relatively high values of the nonlocal scale parameter, the values of the critical buckling loads are very close to each other. It is concluded that the critical buckling load diminishes due to the rise of the nonlocal parameter, and the breadth and height taper ratios. In contrast, the critical buckling load increases as the shear modulus and Winkler modulus parameters become larger.

The authors hope that the obtained results may be useful for scientists in designing and working on the micro- or nanoaxially functionally graded thin structures.

5 NOMENCLATURE

- c_b breadth taper ratio,
- c_h height taper ratio,
- D_N Chebyshev differentiation matrix,
- $E(x)$ modulus of elasticity, [N/ m²]
- $e_0 l$ nonlocal parameter, [m]
- $I(x)$ moment of inertia of the beam, [m⁴]
- k_G shear modulus parameter, [N]
- K_G non-dimensional Shear modulus parameter,
- k_w winkler modulus parameter, [N/ m²]
- K_W non-dimensional Winkler modulus parameter,
- L length of the beam, [m]
- $N+1$ number of Chebyshev points,
- P compressive constant axial load, [N]
- t_{ij} stress tensor, [N/ m²]
- w transverse displacement, [m]
- W non-dimensional transverse displacement,
- x Cartesian coordinate, [m]
- X non-dimensional Cartesian coordinate,
- Greek Symbols**
- λ non-dimensional critical load,

μ non-dimensional nonlocal parameter,
 ζ differential operator,
 σ_{ij} local stress, [N/ m²]

6 REFERENCES

- [1] Natarajan, S., Ferreira, A.J.M., Bordas, S., Carrera, E., Cinefra, M., Zenkour, A.M. (2014). Analysis of functionally graded material plates using triangular elements with cell-based smoothed discrete shear gap method. *Mathematical Problems in Engineering*, art. ID 247932, DOI:10.1155/2014/247932.
- [2] Wang, C.M., Zhang, Y.Y., He, X.Q. (2007). Vibration of nonlocal Timoshenko beams. *Nanotechnology*, vol. 18, no. 10, p. 105401, DOI:10.1088/0957-4484/18/10/105401.
- [3] Eringen, A.C. (2002). *Nonlocal Continuum Field Theories*. Springer-Verlag, New York, DOI:10.1007/b97697.
- [4] Eringen, A.C. (1983). On differential equations of nonlocal elasticity and solutions of screw dislocation and surface waves. *Journal of Applied Physics*, vol. 54, no. 9, p. 4703-4710, DOI:10.1063/1.332803.
- [5] Thang, P.T., Nguyen, T.T., Lee, J. (2017). A new approach for nonlinear buckling analysis of imperfect functionally graded carbon nanotube-reinforced composite plates. *Composites Part B: Engineering*, vol. 127, p. 166-174, DOI:10.1016/j.compositesb.2016.12.002.
- [6] Ashoori, A.R., Salari, E., Sadough Vanini, S.A. (2016). Size-dependent thermal stability analysis of embedded functionally graded annular nanoplates based on the nonlocal elasticity theory. *International Journal of Mechanical Sciences*, vol. 119, p. 396-411, DOI:10.1016/j.ijmecsci.2016.10.035.
- [7] Challamel, N., Hache, F., Elishakoff, I., Wang, C.M. (2016). Buckling and vibrations of microstructured rectangular plates considering phenomenological and lattice-based nonlocal continuum models. *Composite Structures*, vol. 149, p. 145-156, DOI:10.1016/j.compstruct.2016.04.007.
- [8] Liu, J.C., Zhang, Y.Q., Fan, L.F. (2017). Nonlocal vibration and biaxial buckling of double-viscoelastic-FGM-nanoplate system with viscoelastic Pasternak medium in between. *Physics Letters A*, vol. 381, no. 14, p. 1228-1235, DOI:10.1016/j.physleta.2017.01.056.
- [9] Golmakani, M.E., Rezatalab, J. (2015). Nonuniform biaxial buckling of orthotropic nanoplates embedded in an elastic medium based on nonlocal Mindlin plate theory. *Composite Structures*, vol. 119, p. 238-250, DOI:10.1016/j.compstruct.2014.08.037.
- [10] Taati, E. (2018). On buckling and post-buckling behavior of functionally graded micro-beams in thermal environment. *International Journal of Engineering Science*, vol. 128, p. 63-78, DOI:10.1016/j.ijengsci.2018.03.010.
- [11] Ebrahimi, F., Barati, M.R. (2017). Buckling analysis of nonlocal strain gradient axially functionally graded nanobeams resting on variable elastic medium. *Proceedings of the Institution of Mechanical Engineers, Part C: Journal of Mechanical Engineering Science*, vol. 232, no. 11, p. 2067-2078, DOI:10.1177/0954406217713518.
- [12] Ebrahimi, F., Shaghghi, G.R., Boreiry, M. (2016). A semi-analytical evaluation of surface and nonlocal effects on buckling and vibrational characteristics of nanotubes with various boundary conditions. *International Journal of Structural Stability and Dynamics*, vol. 16, no. 6, p. 1550023, DOI:10.1142/S0219455415500236.
- [13] Latifi, M., Farhatnia, F., Kadhodaei, M. (2013). Buckling analysis of rectangular functionally graded plates under various edge conditions using Fourier series expansion. *European Journal of Mechanics - A/Solids*, vol. 41, p. 16-27, DOI:10.1016/j.euromechsol.2013.01.008.
- [14] Pradhan, S.C., Murmu, T. (2010). Small scale effect on the buckling analysis of single-layered graphene sheet embedded in an elastic medium based on nonlocal plate theory. *Physica E: Low-dimensional Systems and Nanostructures*, vol. 42, no. 5, p. 1293-1301, DOI:10.1016/j.physe.2009.10.053.
- [15] Shahidi, A.R., Anjomshoa, A., Shahidi, S.H., Kamrani, M. (2013). Fundamental size dependent natural frequencies of non-uniform orthotropic nano scaled plates using nonlocal variational principle and finite element method. *Applied Mathematical Modelling*, vol. 37, no. 10-11, p. 7047-7061, DOI:10.1016/j.apm.2013.02.015.
- [16] Asbaghian Namin, S.F., Pilafkan, R. (2017). Vibration analysis of defective graphene sheets using nonlocal elasticity theory. *Physica E: Low-dimensional Systems and Nanostructures*, vol. 93, p. 257-264, DOI:10.1016/j.physe.2017.06.014.
- [17] Zhang, L.W., Zhang, Y., Liew, K.M. (2017). Vibration analysis of quadrilateral graphene sheets subjected to an in-plane magnetic field based on nonlocal elasticity theory. *Composites Part B: Engineering*, vol. 118, p. 96-103, DOI:10.1016/j.compositesb.2017.03.017.
- [18] Li, L., Hu, Y. (2017). Torsional vibration of bi-directional functionally graded nanotubes based on nonlocal elasticity theory. *Composite Structures*, vol. 172, p. 242-250, DOI:10.1016/j.compstruct.2017.03.097.
- [19] Demir, Ç, Civalet, O. (2017). A new nonlocal FEM via Hermitian cubic shape functions for thermal vibration of nano beams surrounded by an elastic matrix. *Composite Structures*, vol. 168, p. 872-884, DOI:10.1016/j.compstruct.2017.02.091.
- [20] Murmu, T., Adhikari, S. (2011). Nonlocal vibration of bonded double-nanoplate-systems. *Composites Part B: Engineering*, vol. 42, no. 7, p. 1901-1911, DOI:10.1016/j.compositesb.2011.06.009.
- [21] Trefethen, L.N. (2000). *Spectral Methods in MATLAB, Software, Environments, and Tools*. SIAM, Philadelphia, DOI:10.1137/1.9780898719598.
- [22] Shahba, A., Rajasekaran, S. (2012). Free vibration and stability of tapered Euler-Bernoulli beams made of axially functionally graded materials. *Applied Mathematical Modelling*, vol. 36, no. 7, p. 3094-3111, DOI:10.1016/j.apm.2011.09.073.
- [23] Pradhan, S.C., Murmu, T. (2009). Thermo-mechanical vibration of FGM sandwich beam under variable elastic foundations using differential quadrature method. *Journal of Sound and Vibration*, vol. 321, no. 1-2, p. 342-362, DOI:10.1016/j.jsv.2008.09.018.
- [24] Reddy, J.N. (2007). Nonlocal theories for bending, buckling and vibration of beams. *International Journal of Engineering Sciences*, vol. 45, no. 2-8, p. 288-307, DOI:10.1016/j.ijengsci.2007.04.004.

Vsebina

Strojniški vestnik - Journal of Mechanical Engineering

letnik 64, (2018), številka 12

Ljubljana, december 2018

ISSN 0039-2480

Izhaja mesečno

Razširjeni povzetki (extended abstracts)

- Hürrem Akbıyık, Hakan Yavuz, Yahya Erkan Akansu: Študija geometrijskih konfiguracij elektrod plazemskih aktuatorjev za izboljšanje aerodinamične učinkovitosti aerodinamičnega profila SI 103
- Jinguo Chen, Minli Zheng, Yushuang Sun, Wei Zhang, Pengfei Li: Raziskava mikroskopskega mehanizma trganja nalepka pri orodjih iz karbidne trdine SI 104
- Igor Šauperl, Andreas Wimmer, Dimitar Dimitrov, Jan Zelenka, Gerhard Pirker, Eduard Schneßl, Hubert Winter: LDM COMPACT - metodolgija za razvoj plinskih motorjev na plinasta goriva z majhnim vplivom na okolje SI 105
- Jovan Trajkovski, Miha Ambrož, Robert Kunc: Vpliv koeficienta trenja med avtomobilskimi pnevmatikami in betonske varnostne ograje (BVO) na prevrnitev vozil – MKE analiza SI 106
- Jasna Prester, Borut Buchmeister, Iztok Palčič: Učinki naprednih proizvodnih tehnologij na uspešnost proizvodnih podjetij SI 107
- Ma'en S. Sari, Wael G. Al-Kouz, Anas Atieh: Analiza uklona aksialno funkcionalno gradientnih koničnih nanonosilcev na elastični podlagi s pomočjo nelokalne teorije elastičnosti SI 108

Osebne objave

- Mag. Peter Vogrič - njegov prispevek strojništvu in slovenski industriji, njegovo življenje in delo SI 109

Študija geometrijskih konfiguracij elektrod plazemskih aktuatorjev za izboljšanje aerodinamične učinkovitosti aerodinamičnega profila

Hürrem Akbıyık¹ – Hakan Yavuz^{1,*} – Yahya Erkan Akansu²

¹ Univerza Çukurova, Fakulteta za tehniko in arhitekturo, Turčija

² Univerza Niğde Ömer Halisdemir, Tehniška fakulteta, Turčija

Cilj predstavljene študije je analiza nadzora ločevanja toka in povečanja vzgonske sile pri različnih konstrukcijah elektrod plazemskih aktuatorjev. Eksperimenti so bili opravljeni na letalskem profilu NACA0015. V študijo so bili vključene geometrije elektrod, ki se najpogosteje uporabljajo pri aerodinamičnih aplikacijah.

V študiji so predstavljeni vplivi plazme na inducirani tok pri različnih geometrijskih konfiguracijah elektrod.

Kot model za študijo je bil izbran aerodinamični profil NACA0015. Eksperimenti so bili opravljeni v vetrovniku pri vrednosti Reynoldsovega števila $4,8 \times 10^4$. Plazemski aktuatorji so bili postavljeni na sprednjem robu profila na položaju tetive 0,1 (x C). Sestavljeni so iz vdelane in izpostavljene elektrode, med katerima je dielektrični material. Uporabljena je bila napetost 7 kV_{pp} in frekvenca vzbujaanja 3,5 kHz. V študiji so bile uporabljene tri različne geometrije elektrod: linearna, v obliki žagin zob in v obliki pravokotnih valov.

Rezultati analize:

- Pri plazemskem aktuatorju v oblik žagin zob se je vzgonski koeficient pri vpadnem kotu 10° povečal za približno 91 %. Vzgonski koeficient se je občutno povečal tudi pri linearnem plazemskem aktuatorju.
- Pri linearnem aktuatorju in aktuatorju v obliki žagin zob se je kot porušitve vzgona premaknil iz 8° na 10°.
- Linearni in pravokotni plazemski aktuatorji zagotavljajo večje zmanjšanje upora kot plazemski aktuatorji v obliki žagin zob oz. kot profil brez plazemskih aktuatorjev.
- Pri vpadnem kotu 10° je bilo največje oz. 31-odstotno zmanjšanje upora doseženo s pravokotnim plazemskim aktuatorjem. Koeficient upora se je pri istem plazemskem aktuatorju in vpadnem kotu 12° zmanjšal za 34 %.

Omejitve raziskave, implikacije:

- V študijo so bile vključene majhne vrednosti Re.

Prispevek, novosti, vrednost:

- Izboljšanje aerodinamične učinkovitosti.
- Vrednotenje različnih konfiguracij plazemskih aktuatorjev za zmanjšanje upora in povečanje vzgonskega koeficienta.

Ključne besede: aerodinamični profil NACA0015, koeficient vzgona in upora, pravokotni plazemski aktuator, plazemski aktuator v obliki žagin zob, linearni plazemski aktuator

Raziskava mikroskopskega mehanizma trganja nalepka pri orodjih iz karbidne trdine

Jinguo Chen^{1,2} – Minli Zheng^{1,*} – Yushuang Sun¹ – Wei Zhang¹ – Pengfei Li¹

¹ Kolidž za strojništvo in elektrotehniko, Znanstveno-tehniška univerza v Harbinu, Kitajska

² Šola za elektrotehniko in strojništvo, Univerza v Putianu, Kitajska

Trganje nalepka s cepilne ploskve orodij iz karbidne trdine močno vpliva na obstojnost orodij. V predstavljeni študiji so bili opravljeni eksperimenti in preiskava adhezije na orodjih iz karbidne trdine z vrstičnim elektronskim mikroskopom, kakor tudi meritve parametrov mikrostrukture. Za določitev mikrostrukturnega modela karbidne trdine je uporabljena teorija stereologije. Načelo stereologije je, da je površinsko razmerje komponent na dvodimenzionalnem posnetku povezano z volumskim razmerjem komponent v tridimenzionalnem prostoru. Vzpostavljen je tridimenzionalni model mikrostrukture po metodi končnih elementov za analizo trganja nalepka pri orodjih iz karbidne trdine. Za opredelitev procesa trganja nalepka s cepilne ploskve je na osnovi analize sil v območju nalepka preučena pot napredovanja razpoke na mikroskopski ravni s spreminjanjem kohezijske trdnosti karbidne trdine ter kota med razpoko in cepilno ploskvijo. Rezultati kažejo, da se razpoke pri različnih vrednostih kohezijske trdnosti odklanjajo s povečevanjem kombinirane sile lokalnih delcev. Notranja razpoka v karbidu v odsotnosti začetne razpoke napreduje vzdolž vezne ravnine WC-Co in ravnina napredovanja razpoke je v splošnem pravokotna na smer obremenitve. Trganje nalepka s cepilne ploskve orodja se pojavlja v povezavi z nastankom razpoke. Pri enojni razpoki ima začetna razpoka, ki je vzporedna s cepilno ploskvijo ali pod kotom 45° glede nanjo, velik vpliv na pot napredovanja razpoke za tri vrste začetnih razpok v delcih WC. Kadar je začetna razpoka pravokotna na cepilno ploskev, je vpliv na pot napredovanja razpoke majhen. Pri razpokah na mejnih površinah WC-Co in WC-WC začetna razpoka spremeni pot napredovanja razpoke. Kadar obstaja več začetnih razpok, poteka pot napredovanja razpoke pretežno čez predhodne razpoke ter meje WC-Co in WC-WC. Razpoke se zaradi učinka zasidranja lokalnih delcev združijo in zaobidejo področja z visoko trdnostjo vezi, kar sčasoma privede do zloma in odlusčenja prilepljenega sloja. Rezultati eksperimentov kažejo, da je površina zrn po poškodbi cementiranega karbida razmeroma nedotaknjena, kar je znamenje za interkristalni zlom. Ugotovitve se tako ujemajo z rezultati simulacij. Večja ko je kohezijska trdnost karbida, večja je v odsotnosti razpok natezna trdnost materiala. Kjer obstaja razpoka v karbidni trdini, napredovanje in zasidranje razpoke poveča natezno trdnost do določene mere. Povečanje števila interkristalnih razpok pa zmanjša skupno natezno trdnost materiala, ki je zato bolj nagnjen k zlomu.

Glavni prispevek tega članka je v uporabi programske opreme za tridimenzionalne numerične simulacije za preučitev luščenja prilepljenega sloja s karbidne trdine na mikroskopski ravni v povezavi s spremembami notranjih sil v orodju in nastankom razpok med dejanskim procesom odrezavanja.

Nov je tudi pristop k analizi: delaminacija prilepljenega sloja je analizirana z vidika napredovanja razpoke, v modelu pa so upoštevani kohezijska sila, kot in položaj razpoke ter proces rasti razpoke v različnih pogojih za opredelitev procesa trganja nalepka s cepilne ploskve orodja med realnim procesom odrezavanja. Cilj študije je bila osvetlitev procesa trganja nalepka s cepilne ploskve orodja iz karbidne trdine, ki bo osnova za nadaljnje raziskave mehanizmov trganja nalepka in izboljševanje obstojnosti orodja.

Ključne besede: trganje nalepka, napredovanje razpoke, orodje iz karbidne trdine, natezna trdnost, model kohezijske cone, analiza po metodi končnih elementov

LDM COMPACT – metodologija za razvoj plinskih motorjev na plinasta goriva z majhnim vplivom na okolje

Igor Šauperl¹ – Andreas Wimmer² – Dimitar Dimitrov¹ – Jan Zelenka¹ –
Gerhard Pirker¹ – Eduard Schneßl¹ – Hubert Winter¹

¹ LEC GmbH, Avstrija

² Tehnična univerza v Gradcu, Inštitut za motorje z notranjim zgorevanjem in termodinamiko, Avstrija

LDM COMPACT je metodologija, ki omogoča razvoj konceptov zgorevanja in prilagoditev motorjev na plinasta goriva s specifičnimi lastnostmi brez obsežnega preskušanja na večvaljnem motorju. LDM je kratica za LEC Development Methodology, pri čemer je LEC (Large Engines Competence Center) ime raziskovalne inštitucije, ki je metodologijo razvila.

Izraba plinastih goriv z majhnim vplivom na okolje (t.i. non-natural gases - NNG), za proizvodnjo električne energije in toplote, je ključnega pomena za izkoriščanje razpoložljivih energijskih virov na okolju prijazen način. Med tovrstna goriva štejemo deponijski plin, bakelni plin, premogovniški plin, plin iz čistilnih naprav, bioplina ter druge posebne pline iz industrijskih procesov (npr. plavžni plin). Uporaba teh plinov za proizvodnjo energije je pogosto neučinkovita ali pa jih v ta namen sploh ne izkoriščamo. Problem predstavljajo njihove specifične lastnosti in močna nihanja kakovosti (npr. spodnje energijske vrednosti in metanskega števila).

Veliki plinski motorji, prirejeni za uporabo plinov z neugodnimi lastnostmi a z majhnim vplivom na okolje, so se izkazali kot zelo primerni za proizvodnjo energije. Ti motorji so v primerjavi s konvencionalnimi motorji na zemeljski plin, ki se proizvajajo v relativno velikih količinah, pretežno unikatne izvedbe, kar ima za posledico visoke stroške razvoja in izdelave. Glede na dejstvo, da je izraba posebnih plinov smotrna le, če so stroški ekonomsko vzdržni, je prestop, ki ne zahteva dragega tovarniškega testiranja na večvaljnem motorju, ključnega pomena za snovanje in optimiranje ustreznih motorskih konceptov.

Metodologija LDM COMPACT temelji na intenzivni interakciji med simulacijo in eksperimentalnimi raziskavami na preskuševališču. Pri tem z uporabo 3-dimenzionalne simulacije (CFD) določamo osnovne parametre procesa (npr. geometrijo bata, izmenjavo delovne snovi, itd.), 0- in 1-dimenzionalno simulacijo motorja pa uporabljamo za določanje ključnih parametrov delovanja motorja (npr. kompresijsko razmerje, čas krmiljenja ventilov, itd.). S pomočjo eksperimentiranja na enovaljnem motorju (drugi korak) nato optimiramo izkoristek motorjev in največje možne obremenitve glede na predpisane mejne vrednosti izpustov za uporabljeno plinasto gorivo.

V prispevku sta predstavljena dva primera uspešne uporabe LDM COMPACT metodologije. V prvem primeru gre za izrabo plavžnega, v drugem pa bakelnega plina za proizvodnjo energije. V obeh primerih je rezultat razvoja visoko zmogljiv motor, ki ne presega mejnih vrednosti emisij in deluje stabilno, kljub nihanju kakovosti uporabljenega plinastega goriva.

LDM COMPACT metodologija omogoča neposredno implementacijo koncepta zgorevanja na samem kraju uporabe motorja, brez predhodnega stroškovno intenzivnega testiranja na preskuševališču. Prihranki pri stroških razvoja motorja se prenesejo v korist uporabnika, kar neposredno zniža stroške investicije in s tem poveča njeno atraktivnost. Predstavljena metodologija je tako pomemben dejavnik pri uveljavljanju tehnologije za proizvodno energije z majhnim vplivom na okolje in z nizko emisijo CO₂.

Ključne besede: metodologija, plinski motorji, koncept zgorevanja, plin z majhnim vplivom na okolje (non-natural gas), plavžni plin, bakelni plin

Vpliv koeficienta trenja med avtomobilskimi pnevmatikami in betonske varnostne ograje (BVO) na prevrnitev vozil – MKE analiza

Jovan Trajkovski* – Miha Ambrož – Robert Kunc

Univerza v Ljubljani, Fakulteta za strojništvo, Slovenija

Med najbolj pomembne mehanske dejavnike pri izidu trka vozila v betonsko varnostno ograjo (BVO) spadajo hitrost vozila, kot naleta, faktor statične stabilnosti vozila kot tudi geometrija in stanje betonskih varnostnih ograj. Betonske varnostne ograje so v osnovi zasnovane z namenom zmanjševanja škode na vozilu pri trku, tako da omogočijo dvig vozila pri začetnem kontaktu z delom manjšega naklona in nato preusmeritev vozila nazaj na cestišče. V nekaterih primerih naleta vozil so prav BVO lahko povzročitelj prevrnitev vozila, posledice katerega so pogosto usodne. Za zmanjšanje tveganja prevrnitev vozil je bilo v preteklosti zasnovanih več različnih oblik varnostnih betonskih ograj, pri čemer pa je bil zanemaren pomen koeficienta trenja med pnevmatikami vozila in ograjo.

Namen prispevka je raziskati in poudariti pomen koeficienta trenja med pnevmatikami vozila in BVO v primeru prevrnitve vozila. Izvedeli smo vrsto numeričnih MKE-analiz naleta različnih vozil v BVO ob upoštevanju različnih vrednosti koeficienta trenja med pnevmatikami vozila in BVO. Eksperimentalne meritve koeficienta trenja med pnevmatiko in BVO z različnimi površinami so bile dodatno opravljene v suhih in mokrih vremenskih razmerah za pridobitev podatkov o realnih karakteristikah trenja. Pridobljeni rezultati kažejo, da ima koeficient trenja pri naletu vozila v BVO zelo pomemben vpliv na odziv vozila in lahko povzroči prevrnitev vozila. Zaradi tega je priporočljivo, da proizvajalci in vzdrževalci BVO poskrbijo za to, da je vrednost koeficienta trenja čim nižja.

Rezultati numeričnih MKE analiz so pokazali, da lahko visoke vrednosti koeficienta trenja povzročijo prevrnitev vozila. To zlasti velja za večja vozila z višjim masnim središčem, kot so na primer poltovornjaki, terenska vozila in enoprostorski avtomobili, število katerih se na evropskih cestah neprestano povečuje. Poleg optimizacije geometrije profila BVO je pomembno tudi zmanjšati tveganje za prevrnitev vozila v primeru kontakta med vozilom in BVO. Skladno s tem namenom je treba vpeljati različne strategije, kot so na primer zmanjševanje koeficienta trenja s pomočjo določanja hrapavosti površine BVO ali uporaba prevlek z nizkim trenjem, s pomočjo katerih je mogoče zmanjšati tveganje za prevrnitev vozil iz te skupine.

Ključne besede: betonske varnostne ograje, prevrnitev, trenje, simulacija, LS-DYNA

Učinki naprednih proizvodnih tehnologij na uspešnost proizvodnih podjetij

Jasna Prester¹ – Borut Buchmeister² – Iztok Palčič^{2,*}

¹ Univerza v Zagrebu, Ekonomsko-poslovna fakulteta, Hrvaška

² Univerza v Mariboru, Fakulteta za strojništvo, Slovenija

Namen prispevka je raziskati razširjenost naprednih proizvodnih tehnologij v proizvodnih podjetjih in preučiti njihov vpliv na uspešnost podjetja. Naša raziskava temelji na principih kontingenčne teorije, kjer smo kot kontingenčne dejavnike uporabili velikost podjetja, velikost serij, tip proizvodnje, prilagodljivost kupcu in kompleksnost izdelka. Dodatno je bil namen prispevka preučiti rabo in vpliv naprednih proizvodnih tehnologij v industrijsko nekoliko manj razvitih državah (primerjalno z visoko industrijsko razvitimi državami), kot sta Slovenija in Hrvaška. Z uporabo različnih statističnih metod (deskriptivna statistika in regresijska analiza) smo analizirali rezultate anketne raziskave, ki smo jo izvedli v letih 2015 in 2016.

Raziskava temelji na podatkih iz največje evropske ankete o proizvodni dejavnosti in vključuje podatke iz slovenskih in hrvaških proizvodnih podjetij. V anketi sprašujemo podjetja o proizvodnih strategijah, rabi tehniških in organizacijskih inovacij, selitvi proizvodnje, tipih proizvodnje in izdelkov, konkurenčnih kriterijih, kvalifikacijah in izobrazbi zaposlenih, energijski učinkovitosti podjetij ter o na izdelek vezanih storitvah. Zbiramo tudi podatke o produktivnosti, fleksibilnosti, kakovosti, donosih, itd.

Uspešnost podjetja smo opazovali skozi pet kriterijev: porabo materiala, stroške delovne sile, kakovost izdelkov (merjeno skozi stopnjo odpada izdelkov), inovativnost (ali je podjetje v zadnjih treh letih lansiralo na tržišče nov izdelek) ter dobiček podjetja. Opazovali smo rabo 20-ih naprednih proizvodnih tehnologij, ki smo jih razvrstili v pet skupin: avtomatizacija in robotika, tehnologije za zagotavljanje energijske učinkovitosti, tehnologije za procesiranje novih materialov, dodajalne tehnologije in tehnologije digitalne tovarne. Ugotovili smo, da kontingenčni dejavniki ne vplivajo stroške podjetja, kakovost ali profitabilnost. Napredne proizvodne tehnologije imajo vpliv na porabo materiala, kakovost in profitabilnost, vendar pogosto v negativnem smislu.

Raziskava ima določene omejitve, vezane predvsem na geografsko lokacijo (Slovenija in Hrvaška) in velikost analiziranega vzorca. Posledično bomo v prihodnosti v raziskavo vključili izsledke partnerskih držav v projektu in analizirati raziskovalna vprašanja znotraj specifičnih industrij.

Prispevek je izviren, saj podobnih raziskav s področja rabe naprednih proizvodnih tehnologij in njihovega vpliva na uspešnost proizvodnih podjetij v znanstveni literaturi nismo našli. Dejstvo je, da so klasifikacije naprednih proizvodnih tehnologij pogosto starejšega datuma, zato tudi ni raziskav vpliva novejših naprednih proizvodnih tehnologij na uspešnost podjetja, še posebej redko na osnovi kontingenčnih dejavnikov.

Prispevek ima tudi doprinos za prakso, saj menedžerjem proizvodnih podjetij jasno nakazuje, kako in katere napredne proizvodne tehnologije vplivajo na uspešnost podjetja, merjeno skozi pet zelo pomembnih kriterijev. Odločitve o investicijah v napredno proizvodno opremo so tvegane in finančno zahtevne, zato je pomembno poznati posledice odločitev o implementaciji določene tehnologije v proizvodno okolje.

Ključne besede: napredne proizvodne tehnologije, proizvodno podjetje, uspešnost podjetja, kontingenčna teorija, European Manufacturing Survey

Analiza uklona aksialno funkcionalno gradientnih koničnih nanonosilcev na elastični podlagi s pomočjo nelokalne teorije elastičnosti

Ma'en S. Sari¹ – Wael G. Al-Kouz^{2,*} – Anas Atieh³

¹Nemško-jordanska univerza, Oddelek za strojništvo, Jordanija

²Nemško-jordanska univerza, Oddelek za mehatroniko, Jordanija

³Nemško-jordanska univerza, Oddelek za industrijski inženiring, Jordanija

Predmet študije je analiza stabilnosti aksialno funkcionalno gradientnih koničnih nosilcev. Euler-Bernoullijevi nosilci na mikro-/nanoravni so modelirani s pomočjo Eringenove nelokalne teorije elastičnosti. Vodilne enačbe so izpeljane z diferencialnimi konstitutivnimi relacijami, za pretvorbo diferencialnih enačb gibanja v množico algebrskih enačb pa je uporabljena kolokacijska metoda Čebišova. Nato so določeni robni pogoji in nastali problem lastne vrednosti je razrešen za določitev kritičnih uklonskih obremenitev. Preučeni so vplivi Winklerjevega modula, strižnega modula, koničnosti po širini, koničnosti po višini, koeficienta nelokalne skale in robnih pogojev na kritične uklonske obremenitve. Variabilni koeficienti v vodilni diferencialni enačbi so spremenljiva višina, širina, drugi moment ploskve in modul elastičnosti. Rezultati predlaganega modela so bili verificirani s primerjavo z znanimi podatki iz literature, pri čemer je bilo ugotovljeno dobro ujemanje ter potrjena veljavnost predlaganega numeričnega pristopa in rešitve.

Za diskretizacijo vodilne enačbe in robnih pogojev je bila uporabljena spektralna kolokacijska metoda Čebišova. Znano je, da morata biti pri tankih konstrukcijah, ki so modelirane kot Euler-Bernoullijevi nosilci, izpolnjena dva robna pogoja na koncih nosilca. Ker je v vsaki točki samo ena neznanka, je torej kolokacijsko metodo Čebišova mogoče uporabiti samo za izpolnitev enega od robnih pogojev. Za razrešitev te težave sta bila uporabljena dva robna pogoja tako, da je bil odmik v mejni in sosednji točki izražen z odmiki ostalih točk iz domene.

Rezultati so pokazali, da se s povečevanjem parametra skale zmanjšujejo uklonske obremenitve in stopnja zmanjševanja uklonskih obremenitev je večja pri AFG-nanonosilcih C-C kot pri AFG-nanonosilcih S-S. Iz ugotovitev sledi sklep, da se s povečevanjem koničnosti po širini in višini zmanjšuje uklonska obremenitev, uklonska obremenitev AFG-nosilca C-C pa je občutljivejša na povečanje koničnosti po širini in višini kot pri AFG-nosilcu S-S. S povečevanjem vrednosti strižnega in Winklerjevega modula se povečuje kritična uklonska obremenitev. Ta je ob enakih vrednostih omenjenih parametrov večja pri nosilcu C-C kot pri nosilcu S-S. Iz diagramov je razvidno, da je stopnja povečevanja brezdimenzijske uklonske obremenitve odvisna od razpona Winklerjevega modula. Parameter skale je dominantnejši od Winklerjevega modula in pri razmeroma velikih vrednostih parametra nelokalne skale ima vrednost Winklerjevega modula zanemarljiv vpliv na brezdimenzijske kritične uklonske obremenitve. Kritična uklonska obremenitev je za nosilce C-C v splošnem večja kot za nosilce S-S, pri razmeroma visokih vrednostih parametra nelokalne skale pa so si te vrednosti kritične uklonske obremenitve zelo podobne.

Rezultati pričujoče študije bodo lahko uporabni pri konstruiranju in optimizaciji dvojno koničnih nanonaprav, izdelanih iz aksialno funkcionalno gradientnih materialov, vdelanih v elastični medij, v pomoč pa bodo tudi pri preučevanju uklonskega odziva dvojno koničnih nanonaprav (ki jih je mogoče modelirati kot tanke nosilce) za uporabo v vlogi mehanskih resonatorjev, zaznaval in izvršnih členov. Avtorji upajo, da bodo rezultati uporabni tudi znanstvenikom, ki se ukvarjajo z razvojem aksialno funkcionalno gradientnih tankih mikro- in nanokonstrukcij.

Ključne besede: uklon, proste vibracije, aksialno funkcionalno gradientni nosilci, Eringenova nelokalna teorija elastičnosti, kolokacijska metoda Čebišova, problem lastnih vrednosti

Mag. Peter VOGRİČ

Njegov prispevek strojništvu in slovenski industriji, njegovo življenje in delo

Rodil se je leta 1931 zelo revnim staršem v Labinjah blizu Cerkna na Primorskem, takrat še na ozemlju Italije. Mati je bila brez dohodkov, zato ju je z dve leti mlajšim bratom predala v rejništvo v tujo družino, k starejši vdovi s tremi odraslimi hčera v Gorenjih Novakih. Zanju je skrbela najstarejša od hčera, ki je bila šivilja in brez otrok.

Ko so se Italijani konec tridesetih let prejšnjega stoletja začeli pripravljati na vojno z Jugoslavijo, so obmejno območje začasno izselili v notranjost Italije. Med to akcijo sta devetletni Peter Vogrič in njegov brat prišla v Chiusi blizu Rima. Ob začetku vojne, aprila 1941, so se razmere med prebivalci tega področja zaostrele in rejniška družina se je s svojimi otroki lahko vrnila nazaj. Peter je takrat dopolnil 10 let in je postal dovolj samostojen in močan, da so ga poslali služiti na bogatejšo kmetijo »na Poludi« v bližini rejniške družine, kjer je na planini, ob nekdanji državni meji pasel ovce. Italijani so ozemlje ob meji med njihovo odsotnostjo na gosto minirali z minami tipa ročnih bomb, ki so se sprožile, v primeru naključnega potega zanke. Pastirji so po zankah odkrili sistem polaganja bomb, jih veliko razminirali in občasno posredovali partizanom. Temeljiteje so mejno območje razminirali šele partizani ob kapitulaciji Italije septembra 1943. Zelo hitro zatem so celotno nekdanje italijansko ozemlje zasedli Nemci in nekdanje Rapalske meje ni bilo več. V tem obdobju vojne je trinajstletni Peter doživel grožnjo nemških vojakov, ko je skupina okupatorjevih vojakov preiskovala kmetijo, in zatem doživel še požig stanovanjskega poslopja kmetije. Po tem požigu je kot pastir odšel na oddaljeno kmetijo »na Puču« nad Selško dolino, kjer se je prvič srečal s partizanskimi vezisti. In prav ti, tehnično izobraženi mladi fantje, so mu odprli pogled v prihodnost izven okvirov kmetovanja. Ko je služil na domačiji "na Puču", so v bližini odprli novo šolo. V tej šoli se je Peter pri dvanajstih letih prvič začel učiti slovenski jezik in druge predmete v slovenščini. Pred tem je obiskoval štiri leta italijansko šolo v vasi Laze pri Leskovici. V tej šoli se je govorilo in poučevalo samo italijansko, govoriti slovensko pa je bilo prepovedano in kaznivo.

Vojna se je tudi na tem območju stopnjevala, zaključila pa se je srečno spomladi leta 1945. Na tem ozemlju je med štiriletnim vojskovanjem padlo veliko borcev, na domačijah je nastalo pomanjkanje moške

delovne sile, zato so Petra vabili na delo na kmetije. Ponekod so mu ponudili celo domačijo v upravljanje. Peter je še enkrat zamenjal gospodarja, tokrat je prišel za hlapca v vas Dražgoše, kjer je bila prve mesece po vojni vihri v polnem zagonu obnova požganih domačij. Raznovrstnega kmečkega dela na kmetiji brez moških rok je bilo čez vso mero.

Jeseni leta 1945 je od svojega znanca, nekdanjega vezista, izvedel za novo poklicno šolo v Kropi. Štirinajstletnemu Petru se je posrečilo, da je bil sprejet v prvo generacijo na triletno Industrijsko kovinarsko šolo Kropa, ki je delovala v sklopu tovarne vijakov »Plamen Kropa«. Po treh letih je postal strojni ključavničar. Ta šola je bila prirejena in organizirana za oblikovanje potrebnih znanj delavcev za proizvodnjo konkretnih izdelkov v nastajajočem povojnem gospodarstvu. Industrijska kovinarska šola Kropa je bila ustanovljena po vzoru kvalitetne jeseniške vajeniške šole, ustanovljene pred drugo svetovno vojno, ki je obsegala pouk iz teoretičnih znanj v razredu in v delavnicah privzgjajala ročne spretnosti, pomembne za izdelavo industrijskih izdelkov. Peter Vogrič se je v tej šoli prvič srečal s prepoznavanjem potrebnih tehniških umskih sposobnosti, kakor tudi ročnih spretnosti, ki so osnova vseh izdelovalnih tehnologij. Tu so bile praktično uporabljene vse tehnike, od enostavnih do najbolj zahtevnih načinov obdelave različnih materialov, od kovin do lesa in drugih snovi. Peter Vogrič je do vstopa v to šolo doživel in preživel hud boj za preživetje, ki ga je obvladoval s pridnostjo in iznajdljivostjo. Ti dve lastnosti je uporabil tudi pri osvajanju znanj za oblikovanje proizvodnih procesov, kar mu je koristilo skozi njegovo ustvarjalno aktivnost. V prvih dveh letih triletnega obdobja je med počitnicami opravil še izpite iz predmetov zadnjih razredov osnovne šole, da bi se lahko vpisal na srednjo tehnično šolo. Petra Vogriča je očitno s stroji podprta tehnologija izdelave izjemno zanimala, zaradi česar je med leti strokovnega šolanja dosegal in dokazoval odlične rezultate, dobil dobro spričevalo, ter bil na podlagi tega sprejet na Tehniško srednjo šolo v Ljubljani.

V letih med 1948 in 1951 je Peter Vogrič obiskoval Tehnično srednjo šolo v Ljubljani ter pridobil nova znanja predvsem s področja pravičisanja, geometrije in z ožjega strokovnega področja strojništva. V zadnjem letniku srednje tehniške šole

ga je dipl. ing. Jože Bandelj, profesor na Tehniški srednji šoli v Ljubljani in hkrati ravnatelj Industrijske kovinarske šole Litostroj, pritegnil k honorarnemu delu v konstrukcijski risalnici le-te. Po končani srednji šoli je pridobljeno znanje uporabil tudi pri služenju vojaške obveznosti v letih 1952 in 1953 v Aviotehnični oficirski šoli v Rajlovcu pri Sarajevu, kjer je opravljal vzdrževanje in sodeloval pri razstavljanju in sestavljanju sklopov raznih tipov vojnih letal. V okviru oficirske šole je absolviral tudi obširen učni predmet o konstrukciji vojnih letal od obremenitev do njihovih konstrukcijskih sklopov in detajlov.

Predvsem za potrebe Litostroja je bila za vzgojo in izobraževanje novih industrijskih delavcev ustanovljena Industrijska kovinarska šola Litostroj v letu 1947. Oblikovana je bila po vzoru predhodno opisane Industrijsko kovinarske šole Kropa s poudarkom na seznanitvi in učenju različnih tehnoloških procesov. Poudarek je bil na sosledju pretežno razrednega pouka v prvem letniku do pretežno praktičnega obvladovanja širokega nabora spretnosti, ki so ga učenci pridobivali v zaključnem delu učnega programa v delavnicah. Glede na raznolikost tehničnih izdelkov in pripadajočih tehnologij so bili tudi učni programi prilagojeni tej različnosti, npr. programi za izrazito kovinsko tehnologijo, programi za lesarsko tehnologijo, tehnologijo gradbenih materialov in seveda tudi programi s področja elektrotehnike.

Peter Vogrič je po končani Tehniški srednji šoli v Ljubljani in še pred odsluženjem vojaške obveznosti na predlog takratnega ravnatelja Industrijske kovinarske šole Litostroj Jožeta Bandlja nadaljeval svojo honorarno zaposlitev na tej šoli, najprej kot tehniški risar, v enem letu napredoval v konstruktorja ter po dveh letih postal že vodja šolske konstrukcije (1951), kar je ostal z enoletno prekinitvijo do konca leta 1960, ko je prevzel vodstvo vseh konstruktorskih aktivnosti Litostrojskih proizvodnih skupin. V času vodenja šolske konstrukcije je po vzoru Industrijske kovinarske šole Kropa organiziral praktičen pouk v šoli, predvsem reševanje konkretnih nalog od teoretične zasnove do izročitve izdelka končnemu kupcu. S prizadevanji za poglobitev izobraževalnega dela je Industrijska kovinarska šola Litostroj postala vse bolj uspešna ter znana po dobrih mojstrih, ki so končali to šolo. Obiskovali so jo tudi učitelji in vodstveni delavci iz drugih sorodnih šol Slovenije in Jugoslavije. Tudi združeno podjetje Iskra je v sedemdesetih letih svojo šolo v Ljubljani priključilo Industrijski kovinarski šoli Litostroj. Na pobudo sindikatov dveh držav je prišlo do stika Industrijske kovinarske šole Litostroj in Nemške šole istega ranga v Stuttgartu. Omenjeni šoli sta izmenjavali strokovne obiske in izkušnje ter organizirali letna tekmovanja svojih učencev. S širitvijo proizvodnje v Litostroju

in večanjem števila zaposlenih so se večale tudi potrebe po izobraževanju odraslih, zato je šola postala izobraževalni center tudi za odrasle. Šola je razvijala nove metodične in didaktične modele teoretičnega in praktičnega pouka in skrbela tudi za sodobno opremljanje učilnic s sodobnimi učnimi pripomočki.

Njegov izreden smisel za sintezo strojev so opazili tudi izven Litostroja. Kot izkušenega razvijalca so ga povabili kot svetovalca v skupino, ki je razvijala stavbna dvigala.

Peter Vogrič je ob vsem odgovornem delu v Industrijski kovinarski šoli Litostroj z izjemnimi naporii študiral naprej. V letih 1954 do 1961 je študiral ob delu na Fakulteti za strojništvo, Univerze v Ljubljani, pred tem pa je moral opraviti še gimnazijsko maturo, kar je bil pogoj za vpis na univerzo. (V tem obdobju se je današnja Fakulteta za strojništvo imenovala Univerza v Ljubljani, Tehniška fakulteta, Oddelek za strojništvo (1954-1957) in Univerza v Ljubljani, Fakulteta za elektrotehniko in strojništvo (1957-1960), ter od leta 1960 naprej Univerza v Ljubljani, Fakulteta za strojništvo).

Peter Vogrič je med leti 1950 in 1960 pisno dokumentiral vse stroje ali objekte, ki so bili zasnovani v šolski konstruktorski učilnici, v njihovi delavnici izdelani in aktivirani pri naročniku. Ocenjujem, da omenjena dokumentacija obsega skoraj 100 takih strojev, naročil brez morebitnih ponovitev. V vsakem letu v omenjenem obdobju je bila v delavnicah šole izdelana vsaj ena stiskalnica. Do leta 1957 so bili izdelani klasični tipi stiskalnic za razne namene. Kasneje pa so začeli izdelovati tudi hidravlične stiskalnice. Izpostavil bom leto 1960, kjer so bile dokumentirane hidravlične stiskalnice različnih velikosti in opremljenosti, ki so bile izdelane in prodane raznim zunanjim naročnikom po zamislih g. Vogriča. Številne našete naprave in stroji, ki so bili zasnovani in izdelani v Industrijski kovinarski šoli Litostroj ter dostavljeni kupcem v obdobju med leti 1950 in 1960, predstavljajo tudi velik doprinos Petra Vogriča k razvoju in oblikovanju industrijskega šolstva v Sloveniji za slovenske delavce.

Industrijsko kovinarsko šolo Litostroj je po letu 1973 vsako leto obiskovalo med 500 in 600 učenci, v obdobju med 1987 in 1991 so se začele gospodarske razmere, v katerih je delovala šola, močno spreminjati. Na to so najbolj vplivali odnosi Litostroja do šole zaradi slabšanja gospodarskih razmer v samostojni Republiki Sloveniji. Ta razvoj razmer v gospodarstvu je pripeljal do ukinitve usmerjenega izobraževanja, ukinjen je bil štiri letni program izobraževanja in marca 1992 sta Litostroj in Republika Slovenija podpisala sporazum o prenosu lastništva, pravic in dolžnosti ustanovitelja šole z Litostroja na Republiko

Slovenijo. Leta 1993 je šolanje na Industrijski kovinarski šoli Litostroj zamrlo.

V sedemdesetih letih je Peter Vogrič pri akademiku prof. dr. Janezu Pekleniku opravil magistririj z naslovom »Razvoj in optimizacija oblikovalnih sistemov z uporabo računalnika«, poglavje o tipizaciji ponavljajočih delov je postalo zanimivo pri razvoju novih strojev.

Peter Vogrič je leta 1960 zapustil Industrijsko kovinarsko šolo Litostroj in prevzel vodenje vseh konstrukcijskih oddelkov v Litostroju z utečenim poslovanjem naslednjih proizvodnih skupin: vodnih turbin, centrifugalnih črpalk, ladijskih motorjev ter talnih transportnih sredstev (viličarjev) in žerjavov, prav tako pa je prisostvoval v razvojni skupini za industrijsko opremo, cementarne in opekarne. Ob različnih razvojnih programih je gospoda Vogriča najbolj zanimalo stanje strojev preoblikovalne tehnike (hidravličnih stiskalnic), saj so različna svetovna gospodarstva (avtomobilska, letalska, strojna industrija, industrija široke potrošnje, ...) veliko povpraševala po le-teh. Stroji in naprave preoblikovalne tehnike so namreč omogočali in še omogočajo masovno produkcijo, ki znatno znižuje ceno na enoto izdelka. Osrednji del preoblikovalnega stroja je stiskalnica, to je naprava za ustvarjanje velike in tudi zelo velike pritiskne sile v kratkem in zelo kratkem času z možnostjo hitrega ponavljanja ciklov. S pomočjo različnih dodanih orodij je možno s preoblikovalnim strojem: rezati, izsekavati, obsekavati, kriviti, zapogibati, ploščiti, iztiskati, globoko vleči, hladno volumnsko preoblikovati, ulivati pod tlakom in podobno. In to širino je zaslužil mladi Vogrič že v Industrijski kovinarski šoli Litostroj. Intelktualni izvor Vogričeve preoblikovalne tehnike sega v zadnja leta študija strojništva oziroma v vodenje Industrijske kovinarske šole Litostroj, kjer je do potankosti osvojil zasnovo in izdelavo posameznih hidravličnih stiskalnic, razcvet pa je dosegel v koncernu Litostroj v treh desetletjih, med leti 1961 in 1991 s sistematičnim pristopom k izvirnemu razvoju posameznega preoblikovalnega stroja ter celotnih preoblikovalnih linij. Pri tem razvoju je uporabil modularni sistem, ki omogoča hitrejšo reševanje zahtev pri novih naročilih ter tudi hitrejšo in cenejšo izdelavo. Poleg modularnega sistema, je zelo zgodaj uporabil tipizacijo, kot zelo močno razvojno orodje. Ko je imel za določen tip preoblikovalnega stroja rešitev za eno zmogljivostno stopnjo, je takoj pristopil k postavitvi geometrijske vrste zmogljivosti od najmanjše še uporabne do največje, ki jo je zaznal pri konkurenci. Zatem je izbral vse ključne sklope in dimenzioniral glavne nosilne elemente za vse člene vrste. Oznake izbranih sklopov in glavne dimenzije nosilnih elementov je nato vstavil v ustrezno tabelo

za posamezen tip naprave. Ker je bil Peter Vogrič odličen prostoročni risar s čutom za estetiko, je oba opisana pristopa nadgradil še z modernim oblikovanjem zunanjih površin strojev. Novo estetsko oblikovanje, modularna gradnja in vzpostavljena vrsta pri vsakem tipu je pomenilo veliko konkurenčno prednost pri hitrem odzivanju na povpraševanje in pri razpoznavnosti proizvajalca preoblikovalnih strojev.

Zelo poučno je slediti Vogričevim strokovnim uspehom. Takoj po prihodu iz Industrijske kovinarske šole Litostroj se je moral spopasti s problemom stiskalnic, izdelane po načrtih zunanjega biroja, ki jih je kupec zavrnil kot neustrezne. Na osnovi delujočih stiskalnic, ki so bile izdelane po njegovi zamisli v Industrijski kovinarski šoli Litostroj, je uspel prepričati osrednje vodstvo Litostroja, da se izdelajo nove ustrezne stiskalnice po njegovih načrtih. Kupec je bil z na novo izdelanimi stiskalnicami zadovoljen. Po tem uspehu so prišla nova naročila in letna proizvodnja se je začela vztrajno dvigati. Leta 1966 je znašala 300 ton, leta 1971 720 ton, leta 1976 1100 ton, leta 1981 2600 ton. Vidimo, da se je v petnajstih letih (1966-1981) proizvodnja povečala skoraj za devetkrat. V letih intenzivne rasti proizvodnje je potekal tudi intenziven razvoj sestavnih sklopov preoblikovalnih strojev (funkcionalni elementi, krmilje, varnostni sistemi, nosilno ogrodje, ...), ter priključnih orodij, ki naredijo preoblikovalni stroj namenski, ter sistem strege, ki naredi preoblikovalni stroj vrhunsko učinkovit.

Razvoj ni potekal samo od naročila do naročila, ampak tudi vnaprej v okviru vrste raziskovalnih nalog, ki jih je sofinancirala Raziskovalna skupnost Slovenije. Vsebinsko omenjenih raziskovalnih nalog je načrtoval sam ter v povezavi s posameznimi profesorji na Fakulteti za strojništvo, Univerze v Ljubljani. Tematika teh nalog sega od trdnostnih problemov, preko preučevanja hidravličnih komponent do varnostnih in krmilnih sistemov, vključno z numeričnim programiranjem tehnoloških procesov in njihovo optimizacijo. O svojih načrtih in rezultatih raziskovalnih nalog je poročal v več deset člankih v Litostrojski prilogi Strojniškega vestnika.

V Litostroju je potekala večletna strokovna in poslovna razprava o dveh alternativnih poteh (nakup licence ali samostojen razvoj) za hitrejši in dolgoročnejši poslovni uspeh. Mag. Peter Vogrič je bil odločen zagovornik samostojnega razvoja s svojimi prepričljivimi rezultati. To se je pokazalo tudi ob nakupu licence za stroje za tlačni liv. Ko je imetnik licence že po nekaj letih šel v stečaj, je prav Vogričeva majhna a učinkovita razvojna skupina, v kratkem času obvladala zahtevne stroje za tlačno litje in jih razvila na višji nivo ter z njimi uspela na svetovnem tržišču.

Že nekaj let pred letom 1981 je Peter Vogrič spoznal, da bo potrebno za ta hitro se razvijajoč segment proizvodnega programa Litostroja postaviti nove izdelovalne prostore in novo zgradbo za razvojno delo, samostojno komercialno in druge službe, ki so nujno potrebne za povsem samostojno pot. Sredi sedemdesetih let prejšnjega stoletja, ko je prišlo med Vogričevo skupino vodilnih sodelavcev in vodstvom Litostrojskega koncerna do motečih nesoglasjih, kar Vogrič pripisuje nepoznavanju dejanskega stanja na trgu, se je Vogrič odločil ustanoviti TOZD Proizvodnja preoblikovalne opreme Litostroj. Sam je izdelal celoten koncept nove tovarne, pridobil je vsa potrebna dovoljenja in iz ostanka prihodkov, združevanjem sredstev in bančnimi posojili zagotovil tudi finančno konstrukcijo v znesku 5.000.000.000 dinarjev oziroma v protivrednosti 20 milijonov US \$. Investicija je bila realizirana v letu 1981.

Po realizirani investiciji se je do leta 1986 produkcija povečala na 4300 ton letno in leta 1988 dosegla količinski vrh s 4570 tonami. Nova tovarna ni le prodajala posamične preoblikovalne stroje, ampak je z njimi opremljala celovite produkcijske linije v različnih vejah industrije (avtomobilska, letalska, industrija za široko potrošnjo, ...). Tak kakovostni skok je temeljil na odličnem poznavanju tehnologij v industrijskih sistemih in na sposobnosti obvladovanja celovite logistike v njih. Temu uspehu je sledil še prehod na dobavljanje opreme za fleksibilne avtomatizirane proizvodne celice leta 1986 predvsem s področja tlačnega liva. Tu govorimo o računalniško vodeni in hitro prilagodljivi produkciji. Večinski delež proizvodnje tovarne Proizvodne preoblikovalne opreme Litostroj je šel v izvoz, predvsem v Italijo, Nemčijo, Sovjetsko zvezo, Združene države Amerike, Poljsko, Venezuelo, Egipt, in podobno.

Glavne značilnosti Vogričeve osebnosti in njegovega delovanja so:

- široko lastno znanje + delavnost + močna volja + dosledno izvrševanje sprejetega programa dela in dogovora,
- pogum za pomembne odločitve na osnovi visokega strokovnega znanja, vseživljenjsko zanimanje za širok nabor izdelovalnih tehnik ter za delovanje posameznih strojev,
- sprotno sledenje razvoju istih strojev pri tujih proizvajalcih,
- sodelovanje z zunanjimi nosilci znanja (univerza),
- spopadanje s konkurenco na svetovnem tržišču,
- skrb za kakovost izdelave komponent in končnih izdelkov,
- prenos odgovornosti na prave ljudi, ki posedujejo znanje, kar pogojuje tržno gospodarstvo,

- poslovna samostojnost za ceno brezplačnega dela (imeti neprekinjeno v mislih skrb za rešitev naloge),
- premestiti motnje dogovornega upravljanja centralističnega sistema z neznanjem (uporabiti svoje znanje), centralistični sistemi upravljanja so namreč obstajali na ravni podjetja, pa tudi na vladni (državni) ravni.

V večletnem obdobju vodenja učencev pri reševanju tehničnih problemov z razvojem novih »H« strojev, doseganje vrhunskih rezultatov in na koncu tudi doseženi komercialni uspehi so temeljili na pridobljenem znanju pridobljenega v Industrijski kovinarski šoli Litostroj ter oplemenitenega in teoretično poglobljenega na Fakulteti za strojništvo. Gospod Vogrič je že pred otvoritvijo novega proizvodnega področja preoblikovalne tehnike sledil razvoju potreb na tržišču in nivoju doseženega razvoja tovrstne tehnologije v svetu in sprejel izziv konkurence na svetovnem trgu. Glede na stanje razvoja preoblikovalnih strojev v svetu je, s ciljem premagati konkurenco na tržišču, stalno dopolnjeval svoje znanje o teh strojih in posvečal posebno skrb kakovosti izdelave svojih izdelkov. Gospod Vogrič se je neprekinjeno zavzemal za samostojnost pri odločitvah in poslovno korektnost. Eno od pomembnih načel tržnega gospodarstva je znanje, ki ga mora imeti vsak delavec v ekipi za tržno uspešen izdelek. Litostroj je s preoblikovalnimi stroji brez ovir sodeloval na pomembnih jugoslovanskih in mednarodnih razstavah (Zagreb, Beograd, Hannover, Pariz, Moskva, ...) že pred investicijo in po njej.

Načrtni razvoj skupine Proizvodne preoblikovalne opreme Litostroj in opreme po lastni zamisli Vogriča sodi v leto 1961. Za celovit nastop na trgu je oblikoval poseben proizvodni program, zasnovan na modularnem sistemu gradnje, ki je zajemal stroje za preoblikovanje s pripadajočimi orodji in mehanizmi strege. Na osnovi uspešnega začetka proizvodnje prvega stroja iz družine preoblikovalnih strojev se je to področje pod Vogričevim vodstvom nadaljevalo in razširilo na raziskovalno aktivnost o celovitih strojih. Zelo razvito je bilo raziskovanje tržnih možnosti in spremljanje, kaj na razvoju preoblikovalne tehnike počne konkurenca. Gre za tridesetletne izkušnje razvoja preoblikovalne opreme v obdobju med 1961 in 1991 brez pomoči tujih licenc, saj je bilo v tem obdobju izdelanih okoli 10.000 samostojnih enot, ki so delovale posamično ali kot členi proizvodnih linij s področja preoblikovalne tehnike. Skupaj je bilo izdelanih 300 zelo zahtevnih strojev za tlačno litje. Dosežena je bila tudi velika produktivnost, izražena s prihodkom na zaposlenega, ki je bila 93.000 \$ letno (konec osemdesetih let) oz. vsaj 63 000 \$, če odštejemo delež, ki so ga prispevale podporne službe

drugih delov koncerna Litostroj. Dosežek je bil vsaj dvakrat večji od povprečja v koncernu. Konec osemdesetih let je tovarna Proizvodne preoblikovalne opreme Litostroj prispevala skoraj četrtno celotnega prihodka Koncerna Litostroj ob 11 % zaposlenih od vseh v Litostroju.

V povzetku lahko zapišemo, da se je mag. Peter Vogrič kljub izjemno težkemu otroštvu in z nepopolno osnovno šolo redno izobraževal, najprej v Industrijski kovinarski šoli Kropa, nato v Tehniški srednji šoli ter na Univerzi v Ljubljani, Fakulteti za strojništvo do stopnje magistra znanosti. In skoraj pri vsakem napredovanju v višji nivo izobraževanja je moral nadoknaditi manjkajoče pogoje za vpis (zaključni razredi osnovne šole za vpis na Tehniško srednjo šolo, gimnazijska matura za vpis na univerzo). Univerzitetni del šolanja je opravil ob delu. Ker pa je imel močno voljo, nadarjenost in pristno zanimanje za učno snov, je med šolanjem osvojil ogromno strokovnega znanja. Za razvoj poklicnega izobraževanja in tudi za njegov razvoj je zelo pomembno obdobje dela v risalnici Industrijske kovinarske šole Litostroj. To znanje je potem usmeril v razvoj izjemno pomembnih preoblikovalnih strojev. Pri tem razvoju je z uporabo modernih metod konstruiranja prehitel svetovno konkurenco in s postavitvijo samostojne tovarne znotraj koncerna Litostroj, ustvaril izvozno usmerjeno konkurenčno proizvodnjo, ki je prinašala nadpovprečne prihodke na zaposlenega. Mnogi njegovi preoblikovalni stroji in celotne preoblikovalne linije delujejo še danes.

Obetajoče nastavljena proizvodnja in dosežen obseg prodaje v tovarni Proizvodnja preoblikovalne opreme Litostroj je žal ob osamosvojitvi Slovenije skoraj povsem usahnila. Lahko bi se stvari zasukale tudi drugače, če bi na državni ravni izbrali drugačen način privatizacije družbene lastnine. Gospod Peter Vogrič je namreč že v pogojih planskega gospodarstva deloval povsem kompetitivno in tržno.

Dobrobit narodu ali človeškim skupnostim v veliki meri ustvarjajo izjemni posamezniki s svojim znanjem in inovativnostjo.

Med take inovatorje na področju strojništva je spadal profesor Feliks Lobe, ki je diplomiral leta 1922 na Dunaju. Deloval je kot konstruktor v dunajskih tovarnah za lokomotive in vozila, v Ljubljani je takrat skonstruiral pogonski mehanizem za vlečno tramvajsko vozilo, zaposlen je bil tudi v Slavonskem Brodu, v tovarni za težke konstrukcije. Na osnovi

izkušenj pridobljenih v praksi ga je Milan Vidmar povabil, da v okviru Univerze v Ljubljani oblikuje oddelek za strojništvo. Tej nalogi se je posvetil z navdušenjem. Še pred drugo svetovno vojno je uspel, da je bila ob Aškerčevi cesti zgrajena stavba ter po osvoboditvi nastala sodobno opremljena in za raziskovalno delo primerna Fakulteta za strojništvo z močnim poudarkom na proizvodni tehnologiji. Tu se je kasneje izobrazilo veliko inženirjev, ki so odločujoče oblikovali slovensko gospodarstvo.

Pomembni sodelavci prof. Lobeta na Fakulteti za strojništvo Univerze v Ljubljani so bili še prof. Albert Struna na področju vodnih pogonskih strojev, prof. Bojan Kraut na področju proizvodne tehnologije in standardov, prof. Zoran Rant na področju termodinamike in procesne tehnologije, prof. Franček Kovačec na področju transportnih strojev in konstruiranja ter mnogi drugi.

Slovenskemu gospodarstvu so prav tako v preteklosti bistveno pripomogli številni izkušeni podjetni posamezniki z vizijo in inovatorji kot npr. Gregor Klančnik z izgradnjo Železarne Ravne; Ivan Zupan z izgradnjo Ravenske strojegradnje; Boris Andrijanič z izgradnjo in izjemnim razvojem tovarne Krka; Gustav Tönnis kot graditelj Peltonovih turbin v Mostah pri Žirovnici leta 1915; Jurij Levičnik z razvojem močne Industrije motornih vozil v Novem Mestu; Tine Sever z razvojem inovativnih prikolic Adria Novo mesto; Ivan Munda kot vrhunski razvojni inženir na področju luških in ladjedelniških žerjavov v Metalni Maribor; Tone Kropušek kot dolgoletni direktor Hidromontaže Maribor; Ivan Atelšek kot prvi direktor tovarne Gorenje in podobni.

Poleg naštetih bi lahko omenili še veliko drugih uspešnih inženirjev, gospodarstvenikov in inovatorjev z različnih področij. Le-ti so s svojo strokovnostjo in delavnostjo odločilno prispevali oz. še prispevajo h gospodarskemu napredku Slovenije.

Med zaslužne posameznike spada tudi mag. Peter Vogrič, kot močan steber Litostroja kot celote, kot oblikovalec uspešne Industrijske kovinarske šole Litostroj ter še posebej kot graditelj tovarne Proizvodnja preoblikovalne opreme Litostroj z dolgoletnim lastnim razvojem proizvodnega programa.

Avtor: zasl. prof. dr. Jože Hlebanja

Information for Authors

All manuscripts must be in English. Pages should be numbered sequentially. The manuscript should be composed in accordance with the Article Template given above. The maximum length of contributions is 10 pages. Longer contributions will only be accepted if authors provide justification in a cover letter. For full instructions see the Information for Authors section on the journal's website: <http://en.sv-jme.eu>.

SUBMISSION:

Submission to SV-JME is made with the implicit understanding that neither the manuscript nor the essence of its content has been published previously either in whole or in part and that it is not being considered for publication elsewhere. All the listed authors should have agreed on the content and the corresponding (submitting) author is responsible for having ensured that this agreement has been reached. The acceptance of an article is based entirely on its scientific merit, as judged by peer review. Scientific articles comprising simulations only will not be accepted for publication; simulations must be accompanied by experimental results carried out to confirm or deny the accuracy of the simulation. Every manuscript submitted to the SV-JME undergoes a peer-review process.

The authors are kindly invited to submit the paper through our web site: <http://ojs.sv-jme.eu>. The Author is able to track the submission through the editorial process - as well as participate in the copyediting and proofreading of submissions accepted for publication - by logging in, and using the username and password provided.

SUBMISSION CONTENT:

The typical submission material consists of:

- A **manuscript** (A PDF file, with title, all authors with affiliations, abstract, keywords, highlights, inserted figures and tables and references),
 - Supplementary files:
 - a **manuscript** in a WORD file format
 - a **cover letter** (please see instructions for composing the cover letter)
 - a ZIP file containing **figures** in high resolution in one of the graphical formats (please see instructions for preparing the figure files)
 - possible **appendices** (optional), cover materials, video materials, etc.
- Incomplete or improperly prepared submissions will be rejected with explanatory comments provided. In this case we will kindly ask the authors to carefully read the Information for Authors and to resubmit their manuscripts taking into consideration our comments.

COVER LETTER INSTRUCTIONS:

Please add a **cover letter** stating the following information about the submitted paper:

1. Paper **title**, list of **authors** and their **affiliations**.
2. **Type of paper**: original scientific paper (1.01), review scientific paper (1.02) or short scientific paper (1.03).
3. A **declaration** that neither the manuscript nor the essence of its content has been published in whole or in part previously and that it is not being considered for publication elsewhere.
4. State the **value of the paper** or its practical, theoretical and scientific implications. What is new in the paper with respect to the state-of-the-art in the published papers? Do not repeat the content of your abstract for this purpose.
5. We kindly ask you to suggest at least two **reviewers** for your paper and give us their names, their full affiliation and contact information, and their scientific research interest. The suggested reviewers should have at least two relevant references (with an impact factor) to the scientific field concerned; they should not be from the same country as the authors and should have no close connection with the authors.

FORMAT OF THE MANUSCRIPT:

The Manuscript should be composed in accordance with the Article Template. The manuscript should be written in the following format:

- A **Title** that adequately describes the content of the manuscript.
- A list of **Authors** and their **affiliations**.
- An **Abstract** that should not exceed 250 words. The Abstract should state the principal objectives and the scope of the investigation, as well as the methodology employed. It should summarize the results and state the principal conclusions.
- 4 to 6 significant **key words** should follow the abstract to aid indexing.
- 4 to 6 **highlights**; a short collection of bullet points that convey the core findings and provide readers with a quick textual overview of the article. These four to six bullet points should describe the essence of the research (e.g. results or conclusions) and highlight what is distinctive about it.
- An **Introduction** that should provide a review of recent literature and sufficient background information to allow the results of the article to be understood and evaluated.
- A **Methods** section detailing the theoretical or experimental methods used.
- An **Experimental section** that should provide details of the experimental set-up and the methods used to obtain the results.
- A **Results** section that should clearly and concisely present the data, using figures and tables where appropriate.
- A **Discussion** section that should describe the relationships and generalizations shown by the results and discuss the significance of the results, making comparisons with previously published work. (It may be appropriate to combine the Results and Discussion sections into a single section to improve clarity.)
- A **Conclusions** section that should present one or more conclusions drawn from the results and subsequent discussion and should not duplicate the Abstract.
- **Acknowledgement** (optional) of collaboration or preparation assistance may be included. Please note the source of funding for the research.
- **Nomenclature** (optional). Papers with many symbols should have a nomenclature that defines all symbols with units, inserted above the references. If one is used, it must contain all the symbols used in the manuscript and the definitions should not be repeated in the text. In all cases, identify the symbols used if they are not widely recognized in the profession. Define acronyms in the text, not in the nomenclature.
- **References** must be cited consecutively in the text using square brackets [1] and collected together in a reference list at the end of the manuscript.
- **Appendix(-ices)** if any.

SPECIAL NOTES

Units: The SI system of units for nomenclature, symbols and abbreviations should be followed closely. Symbols for physical quantities in the text should be written in italics (e.g. v , T , n , etc.). Symbols for units that consist of letters should be in plain text (e.g. ms^{-1} , K, min, mm, etc.). Please also see: <http://physics.nist.gov/cuu/pdf/sp811.pdf>.

Abbreviations should be spelt out in full on first appearance followed by the abbreviation in parentheses, e.g. variable time geometry (VTG). The meaning of symbols and units belonging to symbols should be explained in each case or cited in a **nomenclature** section at the end of the manuscript before the References.

Figures (figures, graphs, illustrations digital images, photographs) must be cited in consecutive numerical order in the text and referred to in both the text and the captions as Fig. 1, Fig. 2, etc. Figures should be prepared without borders and on white grounding and should be sent separately in their original formats. If a figure is composed of several parts, please mark each part with a), b), c), etc. and provide an explanation for each part in Figure caption. The caption should be self-explanatory. Letters and numbers should be readable (Arial or Times New Roman, min 6 pt with equal sizes and fonts in all figures). Graphics (submitted as supplementary files) may be exported in resolution good enough for printing (min. 300 dpi) in any common format, e.g. TIFF, BMP or JPG, PDF and should be named Fig1.jpg, Fig2.tif, etc. However, graphs and line drawings should be prepared as vector images, e.g. CDR, AI. Multi-curve graphs should have individual curves marked with a symbol or otherwise provide distinguishing differences using, for example, different thicknesses or dashing.

Tables should carry separate titles and must be numbered in consecutive numerical order in the text and referred to in both the text and the captions as Table 1, Table 2, etc. In addition to the physical quantities, such as t (in italics), the units [s] (normal text) should be added in square brackets. Tables should not duplicate data found elsewhere in the manuscript. Tables should be prepared using a table editor and not inserted as a graphic.

REFERENCES:

A reference list must be included using the following information as a guide. Only cited text references are to be included. Each reference is to be referred to in the text by a number enclosed in a square bracket (i.e. [3] or [2] to [4] for more references; do not combine more than 3 references, explain each). No reference to the author is necessary.

References must be numbered and ordered according to where they are first mentioned in the paper, not alphabetically. All references must be complete and accurate. Please add DOI code when available. Examples follow.

Journal Papers:

Surname 1, Initials, Surname 2, Initials (year). Title. Journal, volume, number, pages, DOI code.

- [1] Hackenschmidt, R., Alber-Laukant, B., Rieg, F. (2010). Simulating nonlinear materials under centrifugal forces by using intelligent cross-linked simulations. *Strojniški vestnik - Journal of Mechanical Engineering*, vol. 57, no. 7-8, p. 531-538, DOI:10.5545/sv-jme.2011.013.

Journal titles should not be abbreviated. Note that journal title is set in italics.

Books:

Surname 1, Initials, Surname 2, Initials (year). Title. Publisher, place of publication.

- [2] Groover, M.P. (2007). *Fundamentals of Modern Manufacturing*. John Wiley & Sons, Hoboken.

Note that the title of the book is italicized.

Chapters in Books:

Surname 1, Initials, Surname 2, Initials (year). Chapter title. Editor(s) of book, book title. Publisher, place of publication, pages.

- [3] Carbone, G., Ceccarelli, M. (2005). Legged robotic systems. Kordić, V., Lazinica, A., Merdan, M. (Eds.), *Cutting Edge Robotics*. Pro literatur Verlag, Mammendorf, p. 553-576.

Proceedings Papers:

Surname 1, Initials, Surname 2, Initials (year). Paper title. Proceedings title, pages.

- [4] Stefančić, N., Martinčević-Mikić, S., Tošanović, N. (2009). Applied lean system in process industry. *MOTSP Conference Proceedings*, p. 422-427.

Standards:

Standard-Code (year). Title. Organisation. Place.

- [5] ISO/DIS 16000-6:2002. *Indoor Air – Part 6: Determination of Volatile Organic Compounds in Indoor and Chamber Air by Active Sampling on TENAX TA Sorbent, Thermal Desorption and Gas Chromatography using MSD/FID*. International Organization for Standardization. Geneva.

WWW pages:

Surname, Initials or Company name. Title, from <http://address>, date of access.

- [6] Rockwell Automation. Arena, from <http://www.arenasimulation.com>, accessed on 2009-09-07.

EXTENDED ABSTRACT:

When the paper is accepted for publishing, the authors will be requested to send an **extended abstract** (approx. one A4 page or 3500 to 4000 characters). The instruction for composing the extended abstract are published on-line: <http://www.sv-jme.eu/information-for-authors/>.

COPYRIGHT:

Authors submitting a manuscript do so on the understanding that the work has not been published before, is not being considered for publication elsewhere and has been read and approved by all authors. The submission of the manuscript by the authors means that the authors automatically agree to transfer copyright to SV-JME when the manuscript is accepted for publication. All accepted manuscripts must be accompanied by a Copyright Transfer Agreement, which should be sent to the editor. The work should be original work by the authors and not be published elsewhere in any language without the written consent of the publisher. The proof will be sent to the author showing the final layout of the article. Proof correction must be minimal and executed quickly. Thus it is essential that manuscripts are accurate when submitted. Authors can track the status of their accepted articles on <http://en.sv-jme.eu/>.

PUBLICATION FEE:

Authors will be asked to pay a publication fee for each article prior to the article appearing in the journal. However, this fee only needs to be paid after the article has been accepted for publishing. The fee is 320 EUR (for articles with maximum of 6 pages), 400 EUR (for articles with maximum of 10 pages), plus 40 EUR for each additional page. The additional cost for a color page is 90.00 EUR. These fees do not include tax.

Strojniški vestnik -Journal of Mechanical Engineering

Aškerčeva 6, 1000 Ljubljana, Slovenia,

e-mail: info@sv-jme.eu



<http://www.sv-jme.eu>

Contents

Papers

- 719** Hürrem Akbiyik – Hakan Yavuz – Yahya Erkan Akansu:
A Study on the Plasma Actuator Electrode Geometry Configurations for Improvement of the Aerodynamic Performance of an Airfoil
- 726** Jinguo Chen, Minli Zheng, Yushuang Sun, Wei Zhang, Pengfei Li:
Research on the Microscopic Mechanism of the Bond Breakage of Cemented Carbide Tools
- 743** Igor Šaupertl, Andreas Wimmer, Dimitar Dimitrov, Jan Zelenka, Gerhard Pirker, Eduard Schneßl, Hubert Winter:
LDM COMPACT – A Methodology for Development of Gas Engines for Use with Low Environmental Impact Non-Natural Gas
- 753** Jovan Trajkovski, Miha Ambrož, Robert Kunc:
The Importance of Friction Coefficient between Vehicle Tyres and Concrete Safety Barrier to Vehicle Rollover - FE Analysis Study
- 763** Jasna Prester, Borut Buchmeister, Iztok Palčič:
Effects of Advanced Manufacturing Technologies on Manufacturing Company Performance
- 772** Ma'en S. Sari, Wael G. Al-Kouz, Anas Atieh:
Buckling Analysis of Axially Functionally Graded Tapered Nanobeams Resting on Elastic Foundations, Based on Nonlocal Elasticity Theory